Thermal Transport in Metal Halide Perovskites and Other Third-Generation Photovoltaic Materials: A Review

Du Chen^{1,2}, Shunran Li^{1,2}, Bowen Li^{1,2}, Peijun Guo^{1,2,*}

¹Department of Chemical and Environmental Engineering, Yale University, New Haven, CT 06520, USA

²Energy Sciences Institute, Yale University, West Haven, CT 06516, USA

^{*}E-mail: peijun.guo@yale.edu

Abstract

Third-generation photovoltaic materials, including metal halide perovskites, quantum dots (QDs), copper zinc tin sulfide (CZTS), and organic semiconductors, among others, have become attractive in the past two decades. Unlike their first- and second-generation counterparts, these advanced materials boast properties beyond mere photovoltaic performance, such as mechanical flexibility, light weight, and cost effectiveness. Meanwhile, these materials possess more intricate crystalline structures for understanding and predicting their transport properties. In particular, the distinctive phonon dispersions in metal halide perovskites, the layered architecture in quasi-two-dimensional (2D) perovskites, the strong quantum confinements in QDs, and the complex crystal structures interspersed with abundant disorders in quaternary CZTS, result in unique and sometimes anomalous thermal transport properties. Concurrently, the criticality of thermal management in applications such as photovoltaics, thermoelectrics, light emitting diodes (LEDs), and photodetections has received increased recognition, considering that many of these thirdgeneration photovoltaic materials are not good thermal conductors. Effective thermal management necessitates precise measurement, advanced modeling, and a profound understanding and interpretation of thermal transport in these novel materials. In this review, we provide a comprehensive summary of various techniques for measuring thermal transport properties of these materials, and discuss the ultralow thermal conductivities of 3D perovskites, superlattice-like thermal transport in 2D perovskites, and novel thermal transport characteristics inherent in quantum dots and CZTS. By collecting and comparing the literature-reported results, we offer a thorough discussion on the thermal transport phenomenon in these materials. The collective understanding from literature in this area, as reviewed in this article, can provide guidance for improving thermal management across a wide spectrum of applications extending beyond photovoltaics.

Keywords

thermal transport, metal halide perovskites, heat transfer, thermal conductivity, nanocrystals, quantum dots, copper zinc tin sulfide, photovoltaics

TABLE OF CONTENTS

- I. Introduction
- II. Measurement techniques
 - 2.1 Laser flash analysis (LFA)
 - 2.2 Photoacoustic (PA)
 - 2.3 Time/frequency-domain thermoreflectance (TDTR/FDTR)
 - 2.4 Transient thermal grating (TTG)

- 2.5 Other photothermal methods
 - 2.5.1 Optothermal Raman spectroscopy
 - 2.5.2 Photothermal deflection spectroscopy & thermal lens spectroscopy
- 2.6 Electrothermal methods
 - 2.6.1 3 ω method
 - 2.6.2 Scanning thermal microscopy (SThM)
 - 2.6.3 Suspended pad
- 2.7 Differential scanning calorimetry (DSC)
- III. 3D perovskites
 - 3.1 Introduction to 3D metal halide perovskite (MHP) photovoltaics
 - 3.2 Thermal conductivity of MAPbI₃
 - 3.2.1 Four-point probe
 - 3.2.2 SThM
 - 3.2.3 TDTR and FDTR
 - 3.2.4 VPVP
 - 3.2.5 Other experimental methods
 - 3.2.6 Numerical simulations
 - 3.3 Constituent-dependent thermal conductivity of MAPbI₃
 - 3.4 Temperature-dependent thermal conductivity of MAPbI₃
- IV. Quasi-2D perovskites
 - 4.1 Introduction to 2D metal halide perovskites
 - 4.2 Ultralow thermal conductivities exceeding bulk limits
 - 4.3 Partially coherent cross-plane thermal transport
 - 4.4 Measuring anisotropic thermal transport

- 4.5 Temperature-dependent thermal transport
- 4.6 Role of halide and organic spacers
- 4.7 Lower dimensionality
- V. Compositional origins of the ultralow thermal conductivities of MHPs
 - 5.1 Role of A-site cation and $[BX_6]^{4-}$ octahedra
 - 5.2 Role of A'-site organic spacers in 2D MHPs
- VI. Quantum dots & CZTS
 - 6.1 Quantum dots (QDs)
 - 6.1.1 Metal chalcogenide QDs
 - 6.1.2 Graphene QDs
 - 6.2 Copper Zinc Tin Sulfide/Selenide (CZTS/Se)
- VII. Summary and outlook

I. Introduction

The escalating global energy demand along with the need for sustainable and environmentally friendly energy sources has propelled the development of advanced photovoltaic (PV) materials. Photovoltaics, which directly convert sunlight into electricity, will play a pivotal role in the future energy landscape. First-generation PV materials, primarily crystalline silicon-based, have dominated the market for decades, achieving improved efficiency and cost reduction. Second-generation thin-film solar cells, including amorphous silicon, cadmium telluride (CdTe), and copper indium gallium selenide (CIGS), are much more lightweight, flexible, and have lower production costs. However, these PV materials face inherent limitations in efficiency due to high non-radiative recombination and low material availability. This has driven significant interest in third-generation PV materials, which promise higher efficiencies, novel functionalities, and potentially lower manufacturing costs. In particular, metal halide perovskites (MHPs), quantum dots (QDs), and copper zinc tin sulfide (CZTS) stand out as promising candidates due to their unique optoelectronic properties.

MHPs have garnered substantial attention due to their remarkable power conversion efficiency improvements, which have rapidly increased from below 4% to over 26% within a decade.³⁻¹¹ Their facile solution-based processing,^{3,12} tunable bandgaps,^{13,14} and defect tolerance^{15,16} make them highly attractive for various optoelectronic applications. In the case of lead halide perovskites, the 6s orbital lone pair electrons in Pb enable highly symmetrical structure and thus direct bandgap, leading to high absorption of light in the visible and near-infrared spectrum suitable for PV applications.¹⁷ In addition, the coupling between the s and p orbitals of Pb and I allow the formation of defect states near or within the valance band and conduction band, making MHPs defect-tolerant with high carrier diffusion lengths.¹⁸ The structure of perovskites can also be substantially modified by changing the organic cation, allowing them to be tailored into two-dimensional (2D) layered MHPs. In 3D MHPs, the A site cation is contained within cages formed between the octahedral structures. In contrast, in 2D MHPs, the octahedra are confined in layers, separated by bulk organic spacers, which exert strong quantum and dielectric confinement on charge carriers.¹⁹ The wide range of available spacers and choice of layer number enable a larger structural tunability and chemical diversity of 2D MHPs.

Quantum dots (QDs), sometimes referred as nanocrystals, are nanoscale semiconducting particles utilized for third-generation photovoltaics. QDs exhibit strong quantum confinement effects, leading to discrete energy levels and size-tunable optical properties. ^{20,21} QDs have larger multiple exciton generation efficiency due to enhanced impact ionization, making it possible to bypass the efficiency bottleneck of single bandgap semiconductor solar cells. ^{22,23} Another third-generation PV material is copper zinc tin sulfide (CZTS), which has a direct bandgap and high absorption coefficient, making it suitable for thin-film solar cells. ²⁴ Unlike traditional PV materials, CZTS is made of earth-abundant and nonpoisonous elements, addressing some of the critical material availability and environmental concerns. ²⁵

While the remarkable electrical and optical properties of third-generation PV materials have been extensively explored, fewer efforts are spent on understanding the thermal transport behaviors of such systems, which significantly influences device performance, stability, and robustness under operation conditions. Effective thermal management is critical for the efficiency and longevity of PV devices due to the existence of many thermal-activated processes. Excessive

heat can lead to increased carrier recombination rates, reduced carrier mobility, phase transition, and material degradation. As an example, 3D MHPs such as MAPbI3 undergo phase transition from tetragonal to cubic above room temperature, which impedes efficiencies after thermal cycling. Elevated temperature is also shown to accelerate material degradation significantly and chemical decomposition can happen at temperatures as low as 80 °C, which is possible in practical solar cell operations.

To effectively lower the operation temperature and optimize the design of PV devices, precise measurement and control of thermal transport properties of PV materials are necessary. As shown in Fig. 1(a), during the past 30 years, the amount of research effort on thermal transport measurements of PV materials surged. This trend is synchronous with the development of thirdgeneration PV materials, which generally possess much smaller thermal conductivity than crystalline silicon (Fig. 1(b)), further attracting attention to thermal management. MHPs are known for their ultralow thermal conductivities. Specifically, low thermal conductivities in MHPs can be attributed to the flattening of low-frequency phonon bands and thus low group velocities, as well as strong anharmonicity arising from the soft inorganic octahedral lattice, which are present regardless of organic cation composition.³⁴⁻³⁶ However, the presence of organic cations may still modify the thermal properties of the perovskite system, by either introducing new vibrational modes or altering material structure. In 3D organic-inorganic hybrid MHPs, the phonon mode associated with slow rotation of the organic cation might also contribute to low thermal conduction at low temperatures.³⁷ In 2D hybrid MHPs, weak van der Waals forces binding neighboring perovskite layers further impede cross-plane heat transport, which is affected by organic spacer orientations.³⁸ The anisotropy of 2D perovskites poses a challenge in measuring both in-plane and cross-plane thermal conductivities accurately. Additionally, the intrinsic instability of hybrid MHPs requires careful consideration of measurement conditions. Vacuum conditions and noncontact methods are preferred to avoid degradation during testing. Therefore, versatile and flexible measurement techniques are essential to accurately characterize the thermal transport properties of these materials under varying conditions.

This review aims to provide a comprehensive coverage of the thermal transport properties of MHPs, while touching on QDs and CZTS, highlighting the experimental techniques used for their measurement. Note that our discussion does not cover organic semiconductors, which has been reviewed elsewhere.³⁹ The first section of the review will introduce a range of commonly used photothermal and electrothermal-based measurement techniques, focusing on their operation principle and capabilities. The second part discusses the thermal properties of 3D MHPs and the effect of chemical composition, temperature, and phonons on thermal transport and summarizes experimental and simulation efforts on measuring thermal properties. The third section considers the scenario of 2D or lower-dimensional MHPs, and in addition to topics discussed for the 3D case, emphasizes mechanisms and measurements of in-plane and cross-plane anisotropic transport. Lastly, the application of QDs and CZTS in photovoltaics and efforts to maximize thermal conduction in these systems are discussed. By combining and comparing the reported results, this review seeks to clarify the range of applicability and limitations of methods used in thermal properties measurement of PV materials and shed light on the underlying physical mechanisms governing thermal transport. Accurate determination and understanding of thermal transport properties will inform the development of strategies for effective thermal management, thereby enhancing the performance and durability of PV devices and broadening their applicability in various optoelectronic applications.

II. Measurement techniques

Broadly, thermal transport measurement techniques can be categorized into transient heatflow methods and periodic heat-flow methods. The latter method was first pioneered by Angström as early as 1863, wherein one end of a metal rod is subjected to periodic heating and the temperature oscillation at another point on the rod was measured. The phase lag between the temperature oscillations at two points offers an accurate evaluation of thermal diffusivity, and consequently, thermal conductivity (κ). Various heat sources, such as light illumination or electrical Joule heating, can induce heat flow in the sample during the measurement. Here, we primarily focus on the photothermal methods, where temperature variations are induced by light absorption and the resulting effects are detected through various signal modalities. A transient decay in the time domain or a modulation dependence in the frequency domain of the detected signals, in either transient heating or periodic heating scenarios, respectively, provides a direct measurement of the thermal transport properties of materials. Below, we give a brief account of the techniques utilized for characterizing third-generation PV materials. Readers interested in a specific technique are encouraged to read the references in each section.

2.1 Laser Flash Analysis

The laser flash method (LFM), also known as the laser flash analysis (LFA), was invented by W.J. Parker in 1961.⁴¹ Since its inception, LFA has been extensively adopted for measuring the thermal diffusivity of materials, including PV semiconductors, $^{42-44}$ owing to its simplicity and ease of implementation. A typical LFA setup is depicted in **Fig. 2(a)**, where a disk or square-shaped specimen is secured in an adiabatic chamber, and its front surface is irradiated by a short laser pulse. The temporal rise in temperature of the rear surface, which manifests as infrared (IR) radiation, is then detected by an IR sensor. This scenario can be accurately described by a one-dimensional heat transfer equation that is analytically solvable. For an optically opaque and geometrically uniform specimen with a thickness of d, the thermal diffusivity can be determined from the temperature rise time as

$$\alpha = 0.1388 \frac{d^2}{t_{1/2}} \tag{1}$$

, where α is the thermal diffusivity in cm²·s⁻¹, and $t_{1/2}$ is the time for the rear-surface temperature rise to reach half of the maximum value. Since LFA measures thermal diffusivity, separate measurements of sample density (ρ) and specific heat (C_p) are required to calculate the effective thermal conductivity $\kappa_{\rm eff}$ using the following relationship:.

$$\kappa_{\text{eff}} = \alpha \cdot C_n \cdot \rho \tag{2}$$

While uncertancy of the thermal conductivity determination by classical LFA was estimated to be from $\pm 3\%$ to $\pm 5\%$, ⁴⁵ more nuanced analysis that takes into account thermal radiation loss and other uncertainties in LFA to improve the accuracy has also been reported. ^{46,47} Instead of the conventional half-rise-time method, the entire time-dependent temperature curve can be fitted with calculations, providing a more accurate determination of thermal diffusivity ⁴⁸ or enabling the simultaneous evaluation of both thermal diffusivity and heat capacity. ⁴⁹ A crucial requirement for LFA is that the flash duration is much shorter compared to the characteristic time of heat diffusion, defined as $\tau_c = d^2/\alpha$, where d is the sample thickness. ⁴¹ This imposes stringent constraints on the

sample thickness, typically required to be of millimeter-scale. Furthermore, commercial equipment often necessitates a minimal lateral size of several millimeters (e.g. 8 mm×8 mm in Netzch LFA 457).⁵⁰ Consequently, commercial LFA instrument is generally employed for measuring the "effective" and isotropic thermal diffusivity of large single crystals or powder-compressed specimens. That being said, some careful treatment to the specimen dimension could potentially enable the measurement of anisotropic thermal transport on the powder-compressed pellets.⁵¹

A method analogous to LFA is pulsed photothermal radiometry (PPTR), which adopts a nearly identical measurement configuration. The primary distinction is that PPTR collects IR emission from the front surface, *i.e.* the same side as for illumination. Unlike LFA where the temperature rise is contributed by the entire volume of the sample, PPTR measures the temperature decay of a skin layer of the surface, making it more sensitive to the surface and sub-surface properties.⁵² With more complex modeling and data analysis, PPTR could provide depth-resolved information of complex structures and layered materials.^{53,54}

2.2 Photoacoustic

Photoacoustic (PA) effect involves the generation of acoustic waves by the absorption of light or other forms of radiation incident on the sample. Such effect was first discovered by Alexander Graham Bell in as early as 1880,⁵⁵ but it faded into obscurity until the late 20th century with the advent of sensitive detectors and intense light sources. PA subsequently emerged as a viable tool for spectral absorption and thermal transport characterization.⁵⁶⁻⁶⁰ An important advantage of photoacoustic spectroscopy (PAS) over reflection-based method, which will be discussed later, is that ultrasmooth and highly reflective surfaces are not necessary.⁶¹

In a typical PAS measurement on solids, a chopped beam of continuous-wave (CW) light or pulsed laser light is incident onto either the front or rear surface of an absorbing sample. The absorbed radiation energy is dissipated into the lattice, primarily as heat. The subsequent periodic temperature excursion leads to intermittent thermal expansion via thermo-elastic effects, generating acoustic waves that propagate through the interior of samples, subsequently detected by a sensor. This detection scheme is sometimes referred to as the transmission mode.⁶² Alternatively, the PA signals can be collected from the fluid (usually gas) in contact with the surface of the sample enclosed in a gas cell. A periodic modulation of surface temperature of the sample gives rise to pressure oscillations in the gas, the amplitude of which is proportional to the surface temperature.⁶³ The collected signal is then amplified and analyzed with a lock-in amplifier.⁶¹

Despite some literatures distinguishing between PA effect (direct generation of acoustic waves inside the sample) and opto-acoustic effects (acoustic waves induced in adjacent fluid), 64,65 in this review, we will use "PA" as a common reference. Generally, PA signals indirectly measured from the adjacent gas under front-surface illumination are more sensitive to the surface temperature changes, while the direct acoustic waves are more influenced by the overall thermal and elastic properties of the sample. In the case of highly absorbing materials where only a skin layer of the sample surface is heated, PA signals from the gas can provide higher sensitivity.

Conventionally, either a microphone or a piezoceramic transducer can be used as the detector for PA signals. Despite the fact that microphone is an inexpensive and most commonly used detectors in PAS, piezoelectric sensors have the advantages of eliminating acoustic mismatch between the gas, the solid sample surface and the microphone membrane. Additionally,

piezoelectric transducers enable the use of much higher modulation frequency,⁶⁶ which is beneficial for avoiding PA saturation^{57,67} and achieving high-resolution photoacoustic imaging.⁶⁸ A typical PAS setup is illustrated in **Fig. 2(b)** adopting a microphone detector.

While both front- and rear-surface illumination configurations are available, it has been verified that accurate thermal transport measurement by PAS requires rear-surface illumination and a modulation frequency appropriately higher than the characteristic frequency, $f_c = \frac{\alpha}{d}$, to eliminate the influence of backing substrate on the results. In this configuration, the sample is usually directly backed by water and then a solid substrate to minimize the parasitic coherent effects accompanying rear illumination. Otherwise, careful system calibration is needed to determine the ratio of effusivities between the backing substrate and sample, $g = \frac{e_b}{e_s}$, where e_b and e_s are the effusivities of the substrate and sample, respectively. Note that, front-surface illumination requires knowledge of g and a modulation frequency lower than f_c .

To determine the thermal diffusivity of the sample, PA measurements can be performed with either a varying or a single modulation frequency. Both the modulation frequency dependence of signal magnitude⁵⁷ and phase⁶⁴ provide information to extract the thermal diffusivity. Using a single modulation frequency, thermal diffusivity can also be evaluated with a similar scheme to the Angström method⁴⁰ where the phase and magnitude of PA signals are measured at varying distance away from the heat source.⁶⁹ Alternatively, magnitude ratio and phase difference of the signals between front- and rear-surface illuminations under single modulation can also be used to precisely determine the thermal diffusivity.⁵⁸

Instead of using uniform illumination, photoacoustic microscope focuses the excitation light to a small spot on the sample with a lens or objective to achieve photoacoustic imaging on a microscopic lengthscale. Combined with the capability of PA signals to provide depth-profile information, subsurface features that are hard to be observed with an optical microscope can be visualized. It is also worth noting that one of the unique characteristics of PAS over other spectroscopic methods is that signals can originate from diverse excited-state decay pathways generating acoustic waves, such as thermal expansion, lettrostriction, lettrostriction, lettrostriction, and plasma formation, molecule decompositions, and charge carrier recombination.

2.3 Time/Frequency-Domain Thermoreflectance (TDTR/FDTR)

Thermoreflectance (TR) is a modulation technique predicated on a periodic perturbation of temperature, which alters the optical properties of the samples that leads to a reflectivity change. For metals, the change in the complex refractive index with temperature $(\frac{d\hat{\pi}}{dT})$, arises from several temperature effects including changes in energy bands, shifts and broadening of the Fermi level, and variations in electron-phonon scattering rates.⁷⁷ Additional effects such as shifts of energy bandgaps in semiconductors also play a role.⁷⁸ The resulting rate of change in reflectivity $(\frac{dR}{dT})$, also termed as the thermoreflectance coefficient, is found to be constant $(10^{-5} \sim 10^{-4} \, \text{K}^{-1})^{79}$ within a small temperature perturbation (< 10 K) at a given wavelength.⁸⁰ Thus, the AC component of reflectivity change (ΔR) in TR is directly proportional to the amplitude of the temperature modulation (ΔT) , allowing the monitoring of temperature changes during heat flow. The first thermal transport measurement applying thermoreflectance dated back to 1986,^{81,82} where ultrafast lasers with a modulation frequency as high as 10 MHz were used to induce periodic heating and the transient temperature change was investigated in the time domain with a picosecond time

resolution. This measurement scheme was later recognized as time-domain thermoreflectance (TDTR).

A key advantage of TDTR over conventional photothermal methods such as LFA is the use of ultrafast lasers with nanosecond (ns) to picosecond (ps) pulse durations, ⁸³ which facilitates the measurement of thin films with nanometer-scale thickness. The heat diffusion length is defined as $L = \sqrt{\alpha \cdot \delta t}$, where α is the thermal diffusivity and δt is the heating time (approximated as the pulse duration). As discussed for LFA, a valid evaluation of κ of thin-film materials requires sample thickness to exceed the thermal diffusion length. The latest model of LFA 457 HyperFlash provides a pulse width down to 10 μ s, with the lower limit for measuring a highly conductive sample such as a copper plate being around 200 μ m. In comparison, with an ultrashort pulse duration, TDTR allows measurement of samples ranging from bulk sizes⁸⁴ down to several tens of nanometers, ⁸⁵ and with κ ranging from $\sim 2000 \text{ W} \cdot \text{m}^{-1} \cdot \text{K}^{-1}$ to as low as 0.03 W·m⁻¹·K⁻¹. ^{86,87}

In a TDTR measurement, a metallic transducer with a high thermoreflectance coefficient is deposited onto the sample surface. The pump and probe beams are focused onto the transducer to comparable spot sizes (5~20 µm). The pump beam induces periodic heat flow from the transducer to the sample and substrate while the probe captures the thermoreflectance response. Fig. 2(c) illustrates a typical experimental configuration of TDTR. A mode-locked Ti:sapphire laser oscillator with a center wavelength at 800 nm generates a train of sub-ps optical pulses at a repetition rate of 80 MHz. A Faraday optical isolator follows immediately after the laser output to prevent back reflection into the oscillator. The laser is then split into two cross-polarized pump and probe beams by a polarizing beam splitter (PBS). The pump beam is typically modulated to a square wave at a frequency of 0.2~20 MHz by an electro-optic modulator (EOM), or an acoustooptic modulator (AOM) with a modulation frequency usually smaller than 1 MHz.88,89 The probe beam is delayed with respect to the pump beam by up to several thousands of ps via a mechanical delay stage. Both the pump and probe beams are then directed and focused by an objective lens onto the sample surface, with the reflected probe beam collected by a photodiode detector converting the varying photon counts to oscillating electrical signals. A radio-frequency lock-in amplifier with a clean sine-wave modulation at the same frequency as the pump beam analyzes the signals, rejecting the DC component and higher harmonics, and isolating only the fundamental harmonic component of EOM.

Several precautions are necessary for TDTR. First is the appropriate choice of transducer according to the laser source used. For a Ti:sapphire laser, an aluminum thin film with a thickness of ~ 100 nm is preferred due to its strong absorption⁷⁷ and remarkably high thermoreflectance coefficient $\sim 10^{-4}\,\mathrm{K}^{-1}$ at 800 nm.⁹⁰ When using other types of ultrafast lasers such as a Nd:YAG laser centered at 1064 nm, a Yb:doped fiber laser centered at 1030 nm, or dye laser centered at 632 nm, different materials may be preferred as the transducers. Another concern is preventing the pump from leaking into the detector, as even a minor amount can disrupt the signals due to the small absolute value of $\frac{dR}{dT}$ from the probe. Two approaches are commonly applied to address this issue. One is to spatially separate the parallel pump and probe beams by several millimeters before entering the objective, allowing the specular reflection of the pump to be blocked by a carefully placed aperture.⁸⁸ This approach is illustrated in the upper boxed panel in **Fig. 2(c)**. While effective for smooth samples with minimal diffuse scattering of pump from the sample surface,⁹¹ a "two-color" approach to spectrally separate the pump and probe is also widely adopted.⁹² As shown in the lower boxed panel in **Fig. 2(c)**, the pump beam coming out of the EOM is incident on a second-

harmonic generation (SHG) crystal. The frequency-doubled pump beam and probe beam are then coaxially aligned and focused by the objective lens. In this case the BS can be replaced by a dichroic mirror (cold mirror) and the reflected pump beam can be further eliminated by a long-pass filter in front of the detector.

During a TDTR measurement, the lock-in amplifier outputs voltage signals comprising of both in-phase and out-of-phase components as $V(t) = V_{\rm in}(t) + iV_{\rm out}(t)$, which contain the necessary thermal information. While the in-phase signal $V_{\rm in}$ is directly related to the transient temperature decay⁹³ and $V_{\rm out}$ is related to the modulated continuous heating,⁹⁴ it is usually the phase, $\varphi = \tan^{-1}(V_{\rm out}/V_{\rm in})$, or equivalently the ratio $R = -V_{\rm in}/V_{\rm out}$ of the signal that is used to determine the κ .^{89,95} Calibration to subtract the additional instrument phases introduced by the optics and electronics is crucial. The instrument phase can be directly measured by splitting a small fraction of the modulated pump beam to a reference detector with the same optical path length as the pump incident on the sample,⁹⁶ or calculated using the ratio between the change in $V_{\rm out}$ and $V_{\rm in}$ across zero delay time.⁸⁹

Similar to some of the thermal transport measurements we discussed in previous sections, TDTR determines the thermal transport properties by iteratively fitting unknown objective parameters, such as κ or diffusivity, and heat capacity, into a carefully constructed heat transfer model to obtain optimal agreement with the measured signals. A widely used diffusive thermal transport model based on Fourier's law of heat transfer in cylindrical coordinates is written as follows^{89,97}

$$C\frac{\partial T}{\partial t} = \frac{\kappa_r}{r} \frac{\partial}{\partial r} \left(r \frac{\partial T}{\partial r} \right) + \kappa_z \frac{\partial^2 T}{\partial z^2} \tag{3}$$

, where κ_r and κ_z are the thermal conductivities of the sample in the radial (in-plane) and crossplane directions, respectively. C is the volumetric heat capacity. The interfacial thermal conductance G between the transducer and sample, or between the interlayers of a multi-layer sample is also taken into consideration, manifesting as a temperature drop that scales linearly with the heat flux across the interfaces, i.e. $\Delta T = q/G$. The uncertainty of fitting single, or multi parameters with a single measurement can differ depending on factors such as materials and substrate properties, transducer thickness, spot size, and modulation frequency. For instance, TDTR with high modulation frequency is more sensitive to the thermal effusivity, $\sqrt{C\kappa}$, rather than to individual properties. As a result, the uncertainty in separately extracting C and K is relatively high. At lower modulation frequencies C, K and K can be uniquely determined with high precision. A more detailed discussion on uncertainty analysis in TR techniques can be found elsewhere.

Note that deviation from the above model will occur as the thermal transport approaches the Casimer regime, where heat transfer is dominated by the ballistic transport of phonons with long mean free paths (MFPs). Practically, this could be the case when the sample is "thermally thin", *i.e.* the thickness is smaller than the thermal penetration depth, $d = \sqrt{\kappa_z/\pi f C}$, where f is the modulation frequency of the pump.⁹⁹

In the majority of TDTR measurements where κ_z and G are of the most interest, the above heat diffusion equation can be simplified to a 1D or quasi-1D cross-plane transport equation. In such cases, the pump spot size must be much larger than the thermal penetration depth, which corresponds to a high modulation frequency. Note that the relationship between the TR signals of

TDTR and the actual temperature decay is not straightforward due to the pulse accumulation effect.⁸⁹ At high modulation frequencies, the system does not have sufficient time to reach thermal equilibrium between pulses, causing continuous temperature excursions. Detailed calculation processes of TDTR signals addressing the after-pulse heating by solving the heat diffusion model in either time⁸⁹ or frequency domain⁹⁷ can be found elsewhere.

Alternative to TDTR, the modulation frequency-dependent TR response under a variation of modulation frequency of the pump can be used to measure thermal transport properties, which is known as frequency-domain thermoreflectance (FDTR). In FDTR, both the pump and probe can use CW lasers which greatly simplifies the configuration and reduces instrument cost. The TR signals are measured with respect to frequency rather than time, and the model is solved in the frequency domain to fit the $\tan^{-1}\left(\frac{V_{out}}{V_{in}}\right)$ vs. f curve. Any thermal property described in eq. (3), i.e. cross-plane and in-plane κ , and heat capacity can be extracted from the TDTR or FDTR signals by implementing different experimental conditions, provided that the rest of the parameters are known, such as the spot size, heat capacity and κ of the transducer, etc. 44

Despite the numerous advantages of TDTR and FDTR, these techniques also have certain limitations. First of all, although TR-based methods require minimal sample preparation, a smooth surface (roughness < 15 nm) is often preferred. Additionally, TDTR/FDTR have relatively low sensitivity to radial heat transfer, presenting challenges in measuring in-plane κ or resolving spatial inhomogeneity. Fortunately, special configurations and approaches have been reported to overcome these limitations and achieve determination of in-plane κ with low uncertainty. Moreover, the performance of TDTR/FDTR at low temperatures is limited due to the low heat capacity of the transducer. In spite of these constraints, TR-based methods are regarded as powerful and versatile methods for measuring the thermal transport properties of materials, particularly thin films and for investigating phonon MFPs. 106-108

It is also worth noting that recent research has focused on removing or replacing the metallic transducers, which induce parasitic contact effects and compromises the sensitivity of conventional TR experiments to deeply buried interfacial thermal conductance, in-plane thermal conduction, and spatial inhomogeneity. For example, one of the transducer-less TR methods, vibrational-pump-visible-probe (VPVP), directly heats up thin-film MHPs with infrared light and monitors their transient TR response without any sample preparation. Alternatively, h-BN, which is commonly applied as an encapsulation layer in nanoscale PV devices, can be heated with pulsed mid-infrared light. The optical transparency of h-BN to visible probe light allows direct spectroscopic observation of the heat flow within and across each of the deeply buried layers of the device. These two variations of TR provide novel tools for achieving in-situ thermal transport measurements on either macroscopic or nanoscale PV materials and devices.

2.4 Transient thermal grating

Transient thermal grating (TTG) is a spatially periodic temperature distribution generated by the absorption of two interfering pump beams. The thermal grating produces a spatial modulation of the refractive index through the thermo-optic effect, along with a spatially varying surface displacement due to ununiform thermal expansion. A time-delayed probe laser incident on the sample is diffracted by the thermal grating and used to monitor the temporal evolution (decay) of the thermal grating. The relaxation time of the grating is then used to extract the thermal diffusivity of the samples. Because the TTG method involves direct excitation of the semiconductors, a population grating or a spatially periodic distribution of excited and ground

states coexists with the temperature grating and simultaneously contributes to the diffraction of the probe beam. However, the relaxation time of the population grating can differ by several orders of magnitude from that of thermal grating, allowing it to be separated from thermal transport modeling.^{117,118} Materials with substantially long carrier lifetime (e.g. MAPbI₃¹¹⁹) are not suitable for this method because it becomes difficult to distinguish between the contributions of heat and charge carriers to the TTG signals.

TTG can adopt versatile configurations,¹¹⁶ among which a frequently used four-wave setup working in reflection mode is illustrated in **Fig. 2(d)**. Two pump beams with a wavelength of λ (usually above-bandgap) overlapped on the sample surface with an angle of θ , generating a spatial intensity pattern through interference with a period of Λ :

$$\Lambda = \frac{\lambda}{2\sin\left(\frac{\theta}{2}\right)} \tag{4}$$

The non-uniform absorption on the surface produces a temperature grating, periodic thermo-elastic deformation, and surface acoustic waves, relaxation of which all have different time dependences. 120-122 Transient decay of the temperature grating can be monitored by the intensity change of the reflected probe, which follows an exponential decay. The thermal diffusivity can be readily determined from the decay time constant without any complex modeling as: 117

$$\alpha = \frac{\Lambda^2}{4\pi^2\tau} \tag{5}$$

, where τ is the time constant of the exponential decay, and Λ is the grating period.

One of the most appealing features of TTG method is its high sensitivity to the lateral heat transfer (parallel to the grating period), thus its capability to measure the in-plane transport of anisotropic semiconductors, such as quasi-2D perovskites¹²³ and TMDs.¹²⁴ Meanwhile, film-morphology induced macroscopic anisotropy can also be studied by TTG.¹²⁵ While the transient relaxation of the temperature at the interference maxima follows a $t^{1/2}$ decay, the temperature response at the grating minima is directly governed by the lateral thermal diffusivity α_{\parallel} as:¹²⁶

$$T \propto \frac{1}{\sqrt{t}} \left(1 - e^{-4\pi^2 \alpha_{\parallel} t / \Lambda^2} \right) \tag{6}$$

Furthermore, as the TTG is primarily influenced by the sample from the surface up to a depth of Λ/π , depth-dependent thermal diffusivity can be semi-quantitively determined by varying the grating period, either through changing wavelength or incident angle of the pump.

2.5 Other photothermal methods

Beyond the photothermal-based methods discussed above – LFA, PPTR, TDTR, FDTR and TTG – other temperature-induced effects, such as light deflection, ^{127,128} thermal lens, ^{129,130} and Raman peak shifts ^{131,132} can also be exploited to produce discernible signals. Although these methods are not as prevalently employed for PV materials and thus fall out of the scoop of this review, we will briefly elucidate them here.

2.5.1 Optothermal Raman spectroscopy (OTRS)

Optothermal Raman spectroscopy (OTRS) is a steady-state measurement wherein a tightly focused laser beam heats up and probes the Raman spectrum of the sample as illustrated in **Fig. 2(e)**. Temperature elevation induces modifications of the Raman spectrum: an increase in the

Raman peaks intensity due to enhanced phonon-phonon scattering, and a redshift of the Raman peak owing to the softening of vibration modes at increased temperature. Under slight perturbations, the redshift of the peak frequency scales linearly with the temperature rise, which itself is linearly dependent on the absorbed laser power. Consequently, employing a micro-Raman spectrometer as a thermometer, a power-dependent Raman measurement can be performed to directly distill the κ of the material. Despite the widespread and successful applications of OTRS, 131,133,134 particularly in 2D inorganic materials, 135-138 one inherent limitation of OTRS is the need to precisely determine the practically absorbed laser power, which is a challenging task typically aided by theoretical estimations. Moreover, OTRS requires high polarizability of the bonds within the materials, thus more suitable for inorganic crystalline materials with well-defined vibrational modes. Materials with strong fluorescence are not preferred for OTRS because the fluorescence can mask the Raman signal, increasing uncertainty.

2.5.2 Photothermal deflection spectroscopy (PDS) & thermal lens spectroscopy (TLS)

Photothermal deflection spectroscopy (PDS) and thermal lens spectroscopy (TLS) are two methods initially conceived for measuring absorption properties but later adapted for thermal characterizations. 129,130,140-142 PDS is predicated on photothermal deflection, a phenomenon where a light beam passing through or near the surface of a heated sample gets deflected. Transient or periodic heating of the sample induces varying temperature gradients within the sample and in the thin gas layer adjacent to the sample surface, the latter case often regarded as the "mirage effect". The temperature gradient results in a refractive index gradient in the medium that deflects the light passing through. As depicted in Fig. 2(f), the temperature changes can be detected by the deflected angle of a probe beam traveling through (i.e. collinear mode) or across the surface of (i.e. transverse mode) the sample using a position sensor. Similarly, thermal lens (TL) effect is the deflection of light due to photothermally induced refractive index gradients. Although fundamentally akin to PDS, TL specifically refers to a lens-like refractive index gradient induced by a Gaussian-shaped light beam that converges or diverges the incident light. ¹⁴⁰ A diverging TLS is shown in Fig. 2(g). Such lensing effect can also occur in the medium adjacent to the sample surface, allowing for either transmission mode which measures bulk materials properties, or reflection mode which is more sensitive to surface characteristics.

2.6 Electrothermal methods

Instead of the photothermal and photoacoustic methods discussed above, where light is the source of heat, electrothermal methods also see a broad application in semiconductors.

2.6.1 3 ω method

The 3ω method leverages the relationship between Joule heating and resistivity changes, allowing for the measurement of κ without a temperature sensor. An AC current of frequency ω is supplied to the sample and heats up the sample with a frequency of 2ω . The voltage across the sample is then detected using a lock-in amplifier, which varies at 3ω as a result of temperature-induced resistivity change. If the sample is an insulator, a metal film can be deposited on the surface to serve as a thermal inducer. Information of the thermal properties of the sample is then implicitly contained between Joule heating and temperature fluctuations, and can be extracted from the lock-in signal. Compared with room temperature steady-state thermal measurements, this method is insensitive to black body radiation due to a much smaller effective thickness of the sample. It is most commonly applied to bulk materials, wires and thin films, but can also extend to liquids. Accurate determination of thermal properties relies on solving the heat conduction

equation for the specific system. Initially, only relatively simple scenarios such as high-frequency limit or low-frequency limit are solved. Later development presents a more general solution in the 1D case which allows simultaneous determination of specific heat and κ . ¹⁴⁶ Recently, the finite element method (FEM) has been introduced to achieve more precise results, accommodating more complex experimental scenarios. ¹⁴⁷ The 3ω method is most commonly used in four-point-probe configuration as shown in **Fig. 3(a)**, but it can be applied in other scenarios as well, such as scanning thermal microscopy (SThM)^{148,149}. Despite that the 3ω method is commonly used to measure the thermal conductivity of bulk materials, by integrating the lead and electrode onto a chip, the 3ω method can be used to measure the thermal conductivity of thin film materials with thickness in the order of nanometers. ¹⁵⁰

2.6.2 Scanning thermal microscopy (SThM)

Scanning thermal microscopy (SThM) is a technique that combines either scanning tunneling microscopy (STM) or atomic force microscopy (AFM) with a thermo-sensitive probe tip, which gives nanometer spatial resolution and microsecond-to-millisecond temporal resolution of the thermal time constant (**Fig. 3(b)**). ^{151,152} It is suitable for measurement of nanoscale structures or microelectronic devices. The most commonly used probe tips are of thermovoltage types, which generate a voltage at a small thermocouple junction, and thermoresistive types, whose resistivity varies with temperature. ¹⁵³⁻¹⁵⁵ SThM can be used to either map out the temperature profiles without an external heat supply (*i.e.*, passive mode) or characterize κ by varying probe tip temperature through electrical or laser heating (*i.e.*, active mode). ^{156,157} Local heat conduction can take several pathways including radiation, diffusive or ballistic conduction, and solid-solid conduction, which heavily depends on the probe parameters and surrounding environment. ¹⁵⁸ Thus, one of the most crucial steps of SThM is calibration, which quantitively relates the amount of heat flow or electrical signals to the local κ of the measured material. Calibration can be performed experimentally by measuring standard samples or by fitting parameters in established models. ^{148,159,160}

2.6.3 Suspended-pad method

The suspended pad is a method that specializes in measuring the thermal transport properties of low-dimensional systems, such as nanotubes, nanowires, and 2D materials. ¹⁶¹⁻¹⁶⁵ As illustrated in **Fig. 3(c)**, a nanowire is suspended between two micro-membranes embedded with metal resistance coils, which serve as both the heaters and temperature sensors by adopting the four-point-probe configuration. The heat conduction process in such a system is thus greatly simplified and the conductivity of a single nanowire can be isolated. ^{166,167}

2.7 Differential scanning calorimetry (DSC)

Apart from all the above discussed photothermal and electrothermal methods to measure the thermal transport properties, another method that is usually used alongside, differential scanning calorimetry (DSC), is also important. More details on this technique are well covered in other literatures. Although DSC typically measures the heat capacity and enthalpy changes, and does not provide a direct measurement of how well heat is transferring through the material, some special configurations and treatments can be applied to measure the heat capacity and κ simultaneously. In the special configurations are treatments can be applied to measure the heat capacity and κ simultaneously.

III. Three-dimensional perovskites

3.1 Introduction to 3D metal halide perovskite photovoltaics

3D MHPs, characterized by the chemical formula ABX₃ (A = Cs⁺, MA⁺, FA⁺; B = Pb²⁺, Sn²⁺; X = Cl⁻, Br⁻, I⁻; MA⁺ = methylammonium, FA⁺ = formamidinium), have catalyzed a revolution in photovoltaics. A typical structure of corner-sharing [BX₆]⁴⁻ octahedra of 3D MHPs is shown in **Fig. 4(a)**. The power conversion efficiencies of perovskite solar cells (PSCs), with a single planar structure as illustrated in **Fig. 4(b)**, has increased rapidly from an initial value of 3.8%³ to more than 26%. ¹⁷¹, ¹⁷² The rapid advancement is attributed to favorable properties including low trap densities, ¹⁷³ high carrier mobilities, ¹⁷⁴ and long carrier diffusion lengths, ¹⁷⁵⁻¹⁷⁸ which collectively facilitate efficient light absorption and charge collection. The structural versatility of MHPs allows for the adjustment of their electronic and optical properties by varying their ionic compositions. This tunability extends their utility across various applications beyond photovoltaics, such as light-emitting diodes (LEDs), ¹⁷⁹ lasers, ¹⁸⁰ and photodetectors. ¹⁸¹ Unlike silicon, which necessitates high-temperature processing, MHPs are appealing due to their potential for lower manufacturing costs ¹⁸²⁻¹⁸⁵ and their compatibility with flexible substrates (**Fig. 4(c)**). ^{186,187}

Despite their advantages, the path toward widespread commercialization of PSCs is still challenged by their environmental instability.¹⁸⁸⁻¹⁹⁰ Specifically, these materials are prone to rapid degradation when exposed to environmental stressors such as moisture, oxygen, and temperature fluctuations (**Fig. 4(d)**),^{190,191} which can lead to decreased efficiency and lifespan of PSCs. To address the stability challenge, considerable research efforts have been directed toward enhancing the robustness of MHPs through chemical modifications and improving device architectures.¹⁹²⁻¹⁹⁴ This includes the development of more stable MHP compositions that are less susceptible to degradation and the application of advanced encapsulation techniques for protecting MHPs from environmental exposures.^{195,196} Additionally, innovations in the interfacial engineering and the optimization of charge transport materials have shown promise in increasing the operational stability and efficiency of PSCs.¹⁹⁷⁻²⁰⁰

Thermal stability, in particular, is a key factor that influences the operational reliability of these devices.²⁰¹ It was shown that an increase in temperature leads to an exponential decay in the lifetime of PSCs (**Fig. 4(e)**). κ is an important property that affects how heat generated within the solar cell is managed, particularly given that the MHP layer serves as the primary heat source in PSCs. Effective thermal management helps prevent thermal degradation of MHPs and maintains PSC efficiency over time.²⁰²⁻²⁰⁵ Recent advancements in the field have shown that managing the thermal properties of MHPs can significantly improve the fabrication and operational stability of solar cells (**Fig. 4(f)**).^{204,205}

3.2 Thermal conductivity of MAPbI₃.

MAPbI₃ holds a pivotal role among the diverse family of 3D MHPs for photovoltaics.³ Since the structure of MAPbI₃ consists of corner-sharing [PbI₆]⁴⁻ octahedra extending in all three directions, in most thermal transport studies this material was treated as isotropic, for which it is amenable to most techniques mentioned in Section II. However, it is important to note that each technique comes with its own degree of uncertainty and specific sample requirements. Consequently, the thermal conductivities of MAPbI₃ can vary significantly depending on its form – whether as a single crystal, film, powder, or nanowire – and the measurement method employed. To provide a clear understanding, the discussion on the κ of MAPbI₃ below will be organized based on the different techniques used by various research groups, specifically four-point probe (**Fig. 5(a)**), SThM (**Fig. 5(b)**), TDTR/FDTR (**Fig. 5(c)**), and suspended pad (**Fig. 5(d)**).

3.2.1 Four-point probe

The steady-state four-point probe method was first applied to investigate thermal transport in MAPbI₃ (Fig. 5(a)).³⁷ In contrast to the 3 ω -based four-point probe method mentioned in Section 2.6.1, here the temperature-dependent electrical resistivity measurement were performed to extract the thermal conductivities. Measurements on single crystals of MAPbI₃ revealed an intrinsic, ultralow κ of 0.5 W·m⁻¹·K⁻¹.³⁷ This value is significantly lower than the κ of other PV materials: single crystalline Si has a κ of 126 W·m⁻¹·K⁻¹ and bulk GaAs owns a κ of 54 W·m⁻¹·K⁻¹ at room temperature. 206,207 This significant disparity highlights the importance of thermal management of PSCs. In addition to single crystal measurements, it is also of great significance to determine the κ of polycrystalline MAPbI₃ thin films. A. Pisoni et al. pressed MAPbI₃ powder and obtained a polycrystalline sample to mimic the effects of the rich grain boundaries in thin films.³⁷ κ of the pressed polycrystal was determined to be 0.3 W·m⁻¹·K⁻¹, smaller than that of single crystals but still lies in the same realm. In contrast, the κ of bulk silicon, single crystal thin film silicon and amorphous silicon are 148, 22 and 1.4 W·m⁻¹·K⁻¹, respectively. ^{206,208} This intrinsically low κ and the small disparity between single-crystalline and polycrystalline forms point to significant, intrinsic phonon scattering in MAPbI₃, which dominates heat transfer over effects from grain boundaries and defects.

As a classical κ measurement method, the four-point probe is straightforward to deploy and produces reliable results, but mounting thermocouples and heat sources onto MHPs may cause sample degradation. Additionally, the configuration lacks the compactness for low-temperature measurements within a vacuum chamber, and is usually conducted in ambient environment with the risk of sample degradation due to presence of water and air, which is especially prominent for thin films. In addition, thermal radiation of the material itself can seriously affect the results. In one work by A. Kovalsky *et al.*, the uncorrected κ is twice as high as the one corrected for thermal radiation loss at room temperature.²⁰⁹ To this end, non-contact methods under a controlled environment have been employed for κ measurement of MAPbI₃.

3.2.2 SThM

R. Heiderhoff *et al.* used SThM method (**Fig. 5(b)**) and obtained a κ of 0.34 W·m⁻¹·K⁻¹ for single crystals and 0.33 W·m⁻¹·K⁻¹ for thin films fabricated by a planar hot-pressing procedure. The small difference within the error margin is consistent with the results obtained by the four-point probe. It should be noted that the thin film consists of a large grain size up to 10 μ m, which is even larger than the phonon MFPs of Si membranes at ambient temperature (~ 400 nm). Taking advantage of the high spatial resolution, SThM can be further used in thermal imaging. J. Zhao *et al.* successfully imaged the local thermal strain, revealing the ferroelastic nature of MAPbI₃. ²¹²

3.2.3 TDTR and FDTR

TDTR and FDTR have been adopted in the investigation of κ of MAPbI₃ (**Fig. 5(c)(e)(f)**). ^{34,213-215} The fitting results across various samples demonstrate strong agreement with the experimental data, regardless of the delay time or the repetition rate (**Fig. 5(e)**). The κ of thin film MAPbI₃ spin-coated on Si substrate was determined to be 0.3 W·m⁻¹·K⁻¹ while the MAPbI₃ film intercalated into an Al₂O₃ mesoporous scaffold produced a lower κ of 0.2 W·m⁻¹·K⁻¹. ²¹⁴ In two other independent works, FDTR performed on MAPbI₃ single crystals produced a κ of 0.34 and 0.35 W·m⁻¹·K⁻¹, respectively. ^{34,215} Regardless of thin films or single crystals, the results given

by TDTR/FDTR are highly consistent with those given by SThM and slightly lower than those given by the four-point probe. The low κ for the MAPbI₃ embedded in Al₂O₃ scaffolds arises due to the grain boundary as small as tens of nanometers.

A TDTR-based study attempted to use a simplified model to extract κ from time-dependent reflection intensity. However, despite a minimal fitting error, a κ value of 11.2 W·m⁻¹·K⁻¹ was obtained on MAPbI₃ thin films, which is more than one order of magnitude higher than all currently reported room-temperature κ of MAPbI₃. Although the low repetition rate (1000 Hz) of the laser ensured that the material had sufficient time to fully return to its initial state, the data used in fitting only covered the first 6 ns, several orders of magnitude shorter than the time of heat dissipation. Missing data points during the subsequent cooling process may compromise the accuracy of the fitting results to a certain extent.

3.2.4 **VPVP**

S. Li *et al.* developed a method dubbed VPVP spectroscopy, a variant of TDTR, where the κ can be obtained by directly fitting transient changes in reflectance or transmittance without the use of a lock-in amplifier for phase detection. 112 Utilizing an electronically triggered probe laser, the maximum delay window in VPVP is up to 1 ms. Note that the nanosecond time resolution is sufficient for resolving the slow thermal dissipation process in MAPbI₃ and other MHPs.

One innovation is that VPVP does not involve a metal transducer. Instead, the MHP thin film itself serves as both the heat source and temperature monitor. By pumping the vibrational mode of the MA⁺ cations with mid-infrared (MIR) laser pulses, the lattice temperature increases impulsively in sub-ns timescale, much shorter than the timescale of thermal dissipation. Meanwhile, the transmittance of MHPs near the band gap is used to monitor the temperature change ΔT as a function of time. A 1D thermal transport model can be established with only two independent parameters: the κ of MAPbI₃ and the interfacial conductance G of the MAPbI₃/substrate interface. Further analysis reveals that when G exceeds 10^6 W·m⁻²·K⁻¹, the transmittance over time becomes solely a function of κ , and the error function reaches a minimum when κ most closely approximates the true value (**Fig. 5(g)**). Within the framework of this simplified model, the fitted ΔT -vs.-time curve exhibits substantial agreement with experimental measurements covering the whole cooling process with a high sensitivity to κ (**Fig. 5(h)**). Depending on the type of substrate, the VPVP-inferred κ of MAPbI₃ ranges from 0.30 to 0.51 W·m⁻¹·K⁻¹, which agrees with values extracted from TDTR/FDTR experiments.

3.2.5 Other experimental methods

Other techniques have also been utilized for measuring the κ of MAPbI₃, when the sample morphology is adjusted to suit experimental requirements, *i.e.* single crystal samples for the LFA, thin film samples for chip-based 3ω method, and nanowire samples for the suspended pad method. Both LFA and chip-based 3ω method yield κ ranging from 0.30 to 0.39 W·m⁻¹·K⁻¹, ²¹⁶⁻²¹⁹ whereas the suspended pad method produced a κ of 0.22 W·m⁻¹·K⁻¹ for MAPbI₃ nanowires, similar with the reduction from single crystals to thin films (**Fig. 5(d)**). ²²⁰ Unlike other methods, where κ shows a weak correlation with sample size, the measurement results from the 3ω method indicate that the κ of the MHP film varies significantly with thicknesses. Specifically, when the film thicknesses are 65 nm, 80 nm, and 100 nm, the κ are 0.31, 0.44, and 0.59 W·m⁻¹·K⁻¹, respectively. ¹⁵⁰ Such a variation in the thermal conductivity was attributed to the difference in carefully tuned crystallite size, thus the density of grain boundaries.

Different from the methods discussed above, C. Shen et al. used photoluminescence spectroscopy to obtain the κ of MAPbI₃.²²¹ Their measurement was predicated on the fact that an increase in the band gap of MAPbI₃ with rising temperature not only causes changes in transmittance but also induces a blue shift in the photoluminescence (PL) spectra, which is linearly proportional to the amplitude of temperature rise. As a st eady-state, transducer-free measurement, a presumption behind their experiments is that energy released through radiation constitutes only a small part of the energy from the incident pump light, so the primary energy dissipation is through non-radiative heat transfer process. The measurements involved specially prepared MAPbI₃ single crystal flakes suspended on a SiO₂/Si substrate prepatterned with an array of holes. By parking the excitation beam at the center of the floating region, heat transfer only occurs along the radial direction. It was further assumed that the temperature of the MHP outside the suspended region is always identical to that of the substrate acting as a heat sink. Under these conditions, the κ can be written as $\kappa = \gamma (Q/\Delta T)^{22}$, where γ is a structure factor, Q is the heating power and ΔT is the temperature difference between the excitation center and the heat sink. Since ΔT is linear to the excitation power, the equation can be further written as $\kappa = \gamma (Q_1 - Q_2)/(T_1 - T_2)$, where T_1 and T_2 are the temperatures under the heating power Q_1 and Q_2 , respectively. Using these equations, C. Shen *et al.* obtained a κ of 0.14 W·m⁻¹·K⁻¹ for MAPbI₃ single crystals. This value is lower than those obtained by other techniques. We note that this method is similar to OTRS, which has been primarily employed to measure the κ of 2D materials with good accuracy. ²²²⁻²²⁵ One potential source of experimental error can be the heat flow in the vertical direction compounded by the PL photon recycling in the film, which can alter the observed spectral location of PL.

3.2.6 Numerical simulations

Aside from experimental efforts, numerical techniques such as molecular dynamics (MD) simulations are widely used to predict the κ of materials. Using the Green-Kubo relation, the κ can be calculated from equilibrium MD simulations as: 231,232

$$\kappa = \frac{1}{3Vk_BT^2} \int_0^\infty \langle \dot{\boldsymbol{w}}(0) \cdot \dot{\boldsymbol{w}}(t) \rangle dt \tag{7}$$

Here k_B is the Boltzmann constant, T is the temperature, V is the volume of the simulation cell, $\dot{\boldsymbol{w}}$ is the heat current, and $\langle \dot{\boldsymbol{w}}(0) \cdot \dot{\boldsymbol{w}}(t) \rangle$ denotes the averaged heat current autocorrelation function. $\dot{\boldsymbol{w}}$ is defined as the time derivative of the first-order energy moment with respect to the atomic position \boldsymbol{r}_i ,

$$\dot{\mathbf{w}} = \frac{d}{dt} \sum_{i} E_i \mathbf{r}_i \tag{8}$$

, where E_i is the total energy of atom i.

MD simulations effectively reproduced the experimental results of MAPbI₃, with κ determined to range from 0.3 to 0.6 W·m⁻¹·K⁻¹.2⁰²,2³¹,2³³ Another benefit of using theoretical calculations is that the anisotropic κ along different crystal orientations can be calculated straightforwardly,²⁰² a task often more challenging for experimentalists.

Density-functional theory (DFT) is a theoretical method widely employed to predict the electronic and vibrational properties of semiconductors. Using DFT-based anharmonic lattice dynamics calculations, the average group velocity and lifetimes of phonons can be deduced from the slope and width of the phonon dispersion relations. With the calculated heat capacity and phonon-phonon scattering rates, the κ can be obtained from the solution of Boltzmann transport

equation (BTE) using these physical quantities. However, one report that is based on DFT calculation yielded a κ of 0.05 W·m⁻¹·K⁻¹,²³⁴ which is significantly lower than values obtained from other experimental or numerical methods. The deviation observed in DFT compared to MD simulations warrants further investigation.

In **Fig. 6** and **Table 1**, we summarize the κ values of MAPbI₃ and the associated methods reported in the literature. Most experimental methods and theoretical calculations show that the κ of MAPbI₃ is orders of magnitude lower than that of other PV materials. It is also discovered that the thermal expansion coefficient of MAPbI₃ is an order of magnitude higher than that of inorganic PV materials, ²¹⁷ which may cause delamination of PSCs under variation of the operating temperatures, thus weakening their long-term stability.

3.3 Constituent-dependent thermal conductivity of MAPbI₃

One of the major advantages of MHPs over other semiconductor materials is their high degree of chemical composition tunability. In this context, tuning the chemical composition of MHPs can inform on the origins behind the ultralow κ of MAPbI₃. One of the most straightforward approaches to isolate and quantify the effect of MA⁺ on thermal transport is to compare the κ of MAPbI₃ with that of CsPbI₃.²⁰⁹ Although the κ of CsPbI₃ (0.43 W·m⁻¹·K⁻¹) is higher than that of MAPbI₃, it remains an order of magnitude lower than that of other inorganic semiconductors. This result suggests that while vibrations of the organic MA⁺ do partly contribute to the low κ , the low κ is common to all MHPs and is not unique to organic-inorganic hybrid ones.

When MHPs are subject to A-site cation mixing of Cs⁺, FA⁺, and MA⁺, the replacement of B-site Pb²⁺ with Sn²⁺, and the interchange of halide anion X⁻ (Cl⁻, Br⁻, and I⁻), their κ are consistently lower than 1 W·m⁻¹·K⁻¹. Fig. 7 and Table 2 summarize the κ values for MHPs published in the literature found by the authors. 34,210,215,235-242 Their similarity implies that the inorganic octahedral framework and the phonons corresponding to the motions of B and X atoms should be responsible for the low κ of MAPbI₃ and other MHPs in general. From the data points in Fig. 7, three key trends emerge: (1) the κ of all-inorganic MHPs are generally higher than those of organic-inorganic hybrid MHPs; (2) for MHPs containing different inorganic cages ([BX₆]⁴⁻), the trend in κ is as follows: $\kappa_{Cl} > \kappa_{Br} > \kappa_{I}$, $\kappa_{Sn} > \kappa_{Pb}$; (3) the κ of MHPs with mixed A⁺ cations or mixed halides are lower than those of their un-mixed counterparts. The first trend has been attributed to the resonant scattering by the organic cations, ^{37,209,220} a phenomenon also reported in other organic-inorganic hybrid materials, and thermoelectric materials with similar cage network, 243 where thermal conductance is greatly suppressed due to the presence of organic constituents. 227,244,245 As for the second trend, one potential origin is the different bond strengths resulted by the differences in oxidation potential and atomic radii. At room temperature, the bond dissociation energies of the B-X bonds are as follows: 350 kJ·mol⁻¹ for Sn-Cl, 337 kJ·mol⁻¹ for Sn-Br, 235 kJ·mol⁻¹ for Sn-I, 301 kJ·mol⁻¹ for Pb-Cl, 248 kJ·mol⁻¹ for Pb-Br, and 194 kJ·mol⁻¹ for Pb-I.²⁴⁶ The strength of these chemical bonds influences the mechanical properties of the MHPs, such as the elastic modulus, consequently affecting the κ . ²⁴⁷ Regarding the third trend, The diversity of chemical components in a system increases its entropy, and one characteristic of high entropy compounds is their low κ . This property is widely exploited in the field of thermoelectrics.²⁴⁸⁻²⁵⁰

3.4 Temperature-dependent thermal conductivity of MAPbI₃

The Debye model is widely used to bridge the macroscopic κ and microscopic phonon behaviors, where κ can be approximated as:³⁷

$$\kappa = CT^3 \int_0^{\theta_D/T} \tau(x) \left[\frac{x^4 e^x}{(e^x - 1)^2} \right] dx \tag{9}$$

Here, θ_D is the Debye temperature, $C = (k_B/2\pi^2 v_s)(k_B/\hbar)^3$, and $x = \hbar\omega/k_BT$, where k_B is the Boltzmann constant, \hbar is the reduced Planck's constant, τ is the average phonon lifetime, and v_s is the average speed of sound. τ can be approximated using the Callaway's approach, with different phonon scattering mechanisms summed up as:²⁵¹

$$\tau^{-1} = \sum_{i} \tau_i^{-1} \tag{10}$$

There are several common scattering mechanisms: grain boundaries, point defects, and Umklapp scattering. The corresponding phonon lifetime can be written as $\tau_B^{-1} = \frac{v_s}{d}$, $\tau_{PD}^{-1} = \frac{V}{4\pi v_s^3} B_{PD}^2 \omega^4$, and $\tau_U^{-1} = \frac{\hbar \gamma^2}{M v^2 \theta_D} \omega^2 T \exp(-\frac{\theta_D}{3T})$, where d is the average crystallite size, V is the unit-cell volume, M is the average atomic mass, and γ is the Grünreisen parameter. For MAPbI3, since MA⁺ has vibrational modes such as rotation, another resonant scattering term in the form of $\tau_R^{-1} = \frac{\omega^2 \omega_0^2}{(\omega^2 - \omega_0^2)^2}$ was added in some studies, where ω_0 is the vibrational frequency of the guest responsible for the resonant scattering. 37,209,253

For solids, especially single crystals, κ initially increases and then decreases with rising temperature. This occurs because in the low-temperature region, as temperature rises, more phonons are activated to conduct thermal energy. As phonon density continues to increase, phonon-phonon interactions intensify rapidly, leading to predominant Umklapp scattering, which ultimately causes κ to decrease with increased temperature. In most studies, the temperaturedependent κ of MHPs, including both single crystals and thin films, follows this trend (see Fig. **8(a)** for an example). However, the scattering mechanisms contributing to the low κ can differ. Given the large grain size and low impurity densities in single crystals, A. Pisoni et al. utilized only the resonant term and the Umklapp scattering term to fit the temperature-dependent κ , obtaining a curve that closely aligns with the experimental data.³⁷ In contrast, Z. Guo et al. chose three terms to incorporate effects from grain boundaries, point defects, and Umklapp scattering, the results of which matches their experimental data.²¹⁴ A. Kovalsky et al. found that unless the temperature falls below 10 K, the inclusion of grain boundaries, point defect, and resonant scattering terms does not significantly alter the temperature-dependent κ curve (Fig. 8(b)).²⁰⁹ It implies that Umklapp scattering starts to dominate heat transfer even at very low temperatures, suggesting strong phonon-phonon coupling in MAPbI₃ across a broad range of temperatures.

While there is consensus on the general tendency for the κ of MAPbI₃ to decrease with increasing temperature (above 100 K), variation in κ near the phase transition temperature differs across studies. There is a sudden increase in κ after the tetragonal-to-cubic phase transition around 330 K measured by SThM,²¹⁰ which was also predicted by MD simulations.²³¹ In all studies involving the LFA, no change near the tetragonal-to-cubic phase transition has been observed.²¹⁶ As for the orthorhombic-to-tetragonal phase transition around 160 K, a decrease in κ was found by TDTR while it was not captured by the four-point probe method.^{37,209,214} It is not clear why different methods give different trends and further research is warranted. It should be noted that in some specific cases, such as MHPs in Al₂O₃ mesostructured films, the κ shows a monotonic

increase with temperature in low-temperature regions (up to room temperature).²¹⁴ This glass-like thermal transport behavior mainly results from the nanostructure and is not an intrinsic property of MHPs.²⁵⁴

IV. Quasi-2D metal halide perovskites

4.1 Introduction to 2D metal halide perovskites

In this section, we will discuss the thermal transport properties of low-dimensional MHPs, primarily focusing on 2D MHPs due to their technological importance. Systematic investigations on the dependence of temperature, ^{43,255} organic spacers, ²⁵⁶⁻²⁵⁹ and inorganic layer thickness ^{258,260-262} reveal that thermal transport in layered 2D MHPs share some characteristics with superlattices ²⁶³⁻²⁶⁵ and self-assembled monolayers, ²⁶⁶⁻²⁶⁸ although these two systems exhibit behaviors unique to themselves as a result of their chemical and structural diversities.

MHPs with reduced dimensionalities (i.e., 2D, 1D and 0D) play an important role in the MHP family due to their favorable optoelectronic properties and diverse applications, including photovoltaics.²⁶⁹⁻²⁷¹ Although the record conversion efficiency of 2D MHP-based PSCs (20%)²⁷² is lower than the state-of-art 3D MHP-based PSCs (~ 26%), 8,273 the advantages of the 2D form have been extensively reported, ^{270,274,275} especially their improved moisture stability owing to the inclusion of hydrophobic organic cations.^{271,274,276} Moreover, instead of serving as the lightabsorbing layer in PSCs, 2D MHPs have also been exploited as interfacial layers to improve the charge collection characteristics and stability of 3D MHP-based PSCs. 277-279 In recent years, there has been a surge in publications on 2D MHPs ^{13,280-283} not only focusing on their potential as photovoltaics but also exploring other applications such as photodetection, ²⁸⁴ LEDs, ^{13,285-287} and thermoelectrics.²⁸⁸ Concurrently, thermal management of 2D MHPs becomes increasingly important. For instance, efficient heat dissipation prompts longer-lifetime LEDs, and effective suppression of heat flow can maintain sizeable temperature gradients for improving thermoelectric performances (Fig. 9(a)). The plethora of available choices of organic spacers provides a playground for tuning the material properties and device performance by adjusting the crystal structures, interlayer distances, and octahedral connectivity modalities.²⁸⁹

The general formulas of (100)-oriented and (110)-oriented 2D MHPs are $A_2'A_{n-1}B_nX_{3n+1}$ or $A'A_{n-1}B_nX_{3n+1}$, respectively where A' is a 1+ or 2+ cation, A is a 1+ cation, B is a divalent metallic cation (e.g. Pb^{2+} , Sn^{2+} , Ge^{2+} , Cu^{2+} , or Cd^{2+}), and X is a halide anion (Cl^{-} , Br^{-} , or I^{-}). The less common (111)-oriented 2D MHPs have a general formula of $A'_{n+1}B_nX_{3n+3}$. The structures of (100)-, (110)- and (111)-oriented 2D MHPs are displayed in Fig. 9(b). The (100)-oriented type, with inorganic layers comprising of corner-sharing $[BX_6]^{4-}$ octahedra separated by interdigitating organic chain cations, are mostly investigated due to their easier processability and higher charge mobility. Based on the selected organic spacers, (100)-oriented 2D MHPs may adopt two different phases: the Ruddlesden-Popper (RP) phase, featuring monovalent interlayer organic spacers (A' = 1 + cation), and the Dion-Jacobson (DJ) phase, characterized by divalent organic spacers. The variation in organic spacers leads to distinct stacking configurations of each layer as shown in Fig. 9(b). Some commonly adopted spacers are presented in Fig. 9(b), although a substantially larger range of cations has been utilized for making 2D MHPs, which has been summarized in an excellent review article. The summarized in an excellent review article.

In addition to the facile fabrication, 270,274 tunable bandgaps $^{291-293}$ and efficient light absorption properties 13 of 2D MHPs, their ultralow κ (even lower than the already-low κ of their 3D counterparts) are garnering increasing attentions. 38,258,260 As discussed in the 3D-MHP section (Section 3.3.3), PSCs may benefit from the low κ of MHPs through longer-lived hot carriers arising from the hot-phonon bottleneck effect. 294 However, slow heat dissipation raises concerns on thermal degradation under high operating temperature (up to 85 °C) of PSCs. 33 This delicate trade-off necessitates better thermal management and hence a deeper understanding of thermal transport in 2D MHPs. Additionally, due to the strong excitonic effect in 2D MHPs, they are also extensively incorporated into LEDs, where heat generation can be more prominent. As we discuss below, while there have been systematic studies delving into certain aspects of the thermal transport properties in low-dimensional MHPs, a comprehensive understanding of all influencing factors and a thorough comparative discussion of existing research are still lacking. $^{38,255-258,260,261,295}$

4.2 Ultralow thermal conductivities exceeding bulk limits

Ultralow κ of a series of 2D MHP films, ranging from $0.1 \sim 0.2~\rm W\cdot m^{-1}\cdot K^{-1}$, were measured by A. Giri *et al.* using TDTR.³⁸ Notably, unlike in highly-doped semiconductors and metals where charge carriers carry a significant amount of heat, ²⁹⁶⁻²⁹⁸ phonons are the dominant heat carriers in 2D MHPs. The exclusive contribution of phonons is even more pronounced in the cross-plane thermal transport in 2D MHPs due to the strong confinement effect on charge carriers imposed by the quantum-well-like structures. ^{19,299} The low κ in 2D MHPs partially comes from similar phonon dispersions to their 3D counterparts, characterized by low phonon group velocities and short phonon lifetimes, which originate from enhanced phonon scattering rates as a result of the significant overlap between acoustic and optical phonon branches. ^{123,260,300,301} Moreover, the ultralow κ of 2D MHPs exceeds the minimum limit of disordered crystals predicted by the Cahill-Watson-Pohl (CWP) model: ³⁸

$$\kappa_{\min} = \frac{1}{6} n_{\text{atom}}^{1/3} \sum_{i} \int_{0}^{\Theta_{j}} \frac{\hbar^{2} \omega^{2}}{k_{B} T^{2}} \frac{e^{\hbar \omega / k_{B} T}}{(e^{\hbar \omega / k_{B} T} - 1)^{2}} d\omega$$
 (11)

, where the κ is calculated by summing over all j^{th} phonon modes (one longitudinal and two transverse), $n_{\rm atom}$ is the atomic density, ω is the phonon angular frequency, $\Theta_j = v_j (6\pi^2 n)^{1/3}$ is the cutoff frequency for mode j with a phonon group velocity v_j . 302

The κ of 2D MHPs are found to be almost an order of magnitude lower than the predicted minimum values, the discrepancy of which is much more pronounced compared with their 3D analogue. Such unexpectedly low κ have been attributed to diffuse phonon scattering occurring at the organic-inorganic interfaces caused by a large mismatch in acoustic impedances²⁶¹ (reaching about 25.1 in a literature report³⁰³). A possible explanation for the experimental observation by A. Giri *et al.* is that thermal transport falls into the classical Casimir regime wherein phonons travel ballistically or quasi-ballistically through the interiors of each perovskite layer and scatter diffusely at the interfaces and boundaries. This implies an incoherent thermal transport scheme at the organic-inorganic interfaces, where phonons behave more like particles that scatter randomly off the interfaces and lose their phase information as schematically illustrated in Fig. 10(a). This picture of thermal transport can be quantitively described by a stacked interfacial thermal conductance model (SITCM) that has been validly applied to self-assembled monolayers^{267,304} and nanocrystal arrays²⁶⁶ with similar organic-inorganic layered structures. One intuitive prediction

one can make with this model is that increasing the interlayer distance will lead to a decreased density of interfaces, consequently resulting in a higher effective κ in the cross-plane direction. That is to say, increased κ should be observed in 2D MHPs with larger periodicity, *i.e.* thicker inorganic layer (larger n number in the formula) or organic layer (longer-chain spacers). This trend coming from the incoherent interface scattering was observed for structurally similar organic/inorganic hybrid superlattices, 266,305,306 and also all-inorganic layered composites where the acoustic impedance mismatch is smaller. 264,307

The as-predicted trend was experimentally verified by N. S. Dahod *et al.* through systematic research on $(C_xH_{2x+1}NH_3)_2(MA)_{n-1}Pb_nBr_{3n+1}$ using DSC and FDTR.²⁵⁸ For stoichiometry with n larger than one, it represents a quasi-2D MHP comprising of n layers of $[PbBr_6]^{4-}$ octahedra stacked in the (100) direction, confined by the organic layers. By varying the n number and the value of x, the thickness of the inorganic layer and the organic layer can be systematically altered, respectively. In this meticulous work, the 2D MHPs were treated as superlattice-like hybrid materials that fit in the incoherent thermal transport model presented in **Fig. 10(a)**, with phonons treated as particles described by the Boltzmann transport equation with boundary conditions involving diffuse interface scattering.²⁶⁵ Two key assumptions underpin this model: (1) the phonon MFP of the bulk material making up the superlattice is comparable or slightly larger than the period thickness so that phonons within individual layers travel ballistically or quasi-ballistically without coherent correlation and scatter diffusely at the interfaces; (2) each layer is governed by its bulk dispersion relations.³⁰⁸

N. S. Dahod *et al.* posited similar phonon MFPs in 2D MHPs as in their 3D form, 258 which is comparable to or slightly larger than the periodicity of the alternating layers $(1 \sim 2 \text{ nm})^{309,310}$ ensuring ballistic behavior of phonons inside the inorganic layers. Although counter-intuitive, phonons were also assumed by N.S. Dahod *et al.* to be traveling ballistically through the organic layer, despite the intrinsically ultralow κ of alkanes. According to the second assumption, the heat capacity and sound speed within the perovskite octahedra and alkylammonium chain layers are taken to be analogous to those in 3D MAPbBr₃ and liquid alkanes, respectively. The decoupling of phonon branches between different layers here is a reasonable assumption, given that the vibrational density of states of 2D MHPs resemble the sum of those of the organic and inorganic sub-lattices as implied by low-frequency Raman spectroscopy. The monotonic trend of increasing κ with the thickness of either the organic or the inorganic layer (**Fig. 10(b)**) is well described by the following equation, originally derived for superlattices 264 :

$$\kappa = \frac{1}{2} \left(\frac{1}{C_1 \nu_1} + \frac{1}{C_2 \nu_2} \right)^{-1} \frac{(d_1 + d_2)}{2}$$
 (12)

, where the subscripts represent different layer components, organic or inorganic, C_i is the bulk volumetric heat capacity, v_i is the sound velocity, and d_i is the layer thickness. Moreover, the measured heat capacities show fair alignment with this model assuming the overall heat capacity to be the mass average between the organic and inorganic subphases (Fig. 10(b)).

More researchers, however, have observed consistent or even decreasing κ of 2D MHPs with an increasing layer thickness, which brought about the existence of a distinct thermal transport mechanism in the cross-plane direction that is dominated by coherent acoustic phonons. ^{256,257,260} In this picture, as shown in **Fig. 11(a)**, phonons move in a wave-like manner and propagate through layers via collective vibrations of the whole materials, akin to an inorganic superlattice in the κ recovering regime. ²⁶³ Phonons of this kind feature MFPs much larger than the periodicity and

preserve coherence for up to several layers. Further supporting works for this model are discussed below.

4.3 Partially coherent cross-plane thermal transport

The existence of coherent longitudinal acoustic phonons (CLAPs) in 2D RP-phase MHPs, $(BA)_2(MA)_{n-1}Pb_nI_{3n+1}$ (n=1-6), was first experimentally verified and investigated by P. Guo et al. using a pump-probe-based transient reflection technique.²⁶¹ An above-bandgap pump was used to excite hot charge carriers, which quickly thermalize through electron-phonon coupling, accompanied by emission of longitudinal optical (LO) phonons.³¹¹ These emitted LO phonons rapidly decay to lower-energy longitudinal acoustic (LA) phonons³¹² that propagate coherently in the cross-plane direction. The local strain induced along the propagation of such CLAPs causes depth-dependent modifications on the local material refractive index. A below-bandgap (nearinfrared) probe light is reflected by the sample and collected by a spectrometer. The interference coming from the spatial-temporal variation in refractive index results in oscillations in the probe intensity over time as shown in Fig. 11(b). Information about the CLAPs such as coherence time and group velocities can then be extracted from these oscillations. Evidently from Fig. 11(b), compounds with smaller n number show stronger coherence and longer lifetimes of CLAPs. Applying a similar technique to another 2D RP-phase MHPs, $(PEA)_2(MA)_{n-1}Pb_nI_{3n+1}$, P. Maity et al. further verified the existence of the long-lived (extending up to nanoseconds) CLAPs, similar to those present in 3D MHPs, while the lifetime of optical phonons in the system is only on the sub-ps scale.³¹³

Despite featuring reduced group velocities and significant attenuation compared to the 3D counterparts due to the large acoustic impedance mismatch between organic and inorganic layers, the relatively long-lived CLAPs could serve as important heat carriers in cross-plane thermal transport and potentially lead to increased κ . Numerous studies provide compelling evidence of another more complex thermal transport scheme involving coherent phonon transport across the layer interfaces, contrary to the purely diffusive scattering model discussed in Section 4.2. In this partially coherent thermal-transport picture, both incoherent interface scattering and coherent wave-like transport of phonons across the interfaces contribute to the overall heat transfer through the layered structures. 265

While modeling the phonon propagation with a coherent wave equation, the diffuse interface scattering is accounted for by an imaginary part in the propagation wave vector of coherent phonons. This model is well-established to explain the period thickness dependence of κ in superlattices. Two anomalous trends in κ , contrary to the prediction made by SITCM, are generally observed experimentally in a wide range of research, supporting the notion that a substantial amount of heat is carried by coherent phonons.

One observation is the cross-plane κ being nearly independent on the thickness of the organic layer (chain length of the organic spacers). ^{38,256,257} A. Giri *et al.* revealed an insignificant influence of spacing distance between the inorganic layers on the κ with TDTR. ³⁸ Furthermore, by increasing the organic chain length in $(C_nH_{2n+1}NH_3)_2PbI_4$ from n=4 to n=7, an almost constant, and even decreasing κ was found with the same TDTR technique at 330 K (**Fig. 11(c)**). ²⁵⁶ This trend is inconsistent with the prediction of the incoherent thermal transport model, *i.e.* SITCM, and is attributed to phonons propagating coherently across interfaces. The coherence of phonons is expected to be disrupted by larger periodicity, coming from the lengthened organic spacers according to the partially coherent model. A recent work, up to the point of this review, reported

an almost 2-fold decrease in κ (at room temperature) as the organic chain length increases from n = 4 to n = 6 in $(C_n H_{2n+1} NH_3)_2 PbI_4$, also measured with TDTR.²⁵⁹

Another unexpected trend is the decreasing cross-plane κ with thicker inorganic layers (larger n number in the general formula). An D. Christodoulides et al used FDTR to investigate the κ dependence on the inorganic layer thickness by measuring $(BA)_2(MA)_{n-1}Pb_nI_{3n+1}$ with n increasing from 1 to 4 for thin films and n=3-6 for single crystals. A monotonically decreasing trend of κ with n was observed (Fig. 11(d)), which contrasts with the results from N. S. Dahod et al that assumed totally incoherent thermal transport across interfaces. Both P. Guo et al and A. D. Christodoulides et al applied a simple harmonic bead-spring model (Fig. 11(e)) to capture the coherent nature of these systems and revealed a stronger band-flattening effect in the phonon dispersions for systems with higher n values. Relationship between the phonon dispersion and material κ is given by an equation similar to eq. (11): 265,315

$$\kappa_i = \sum_{\lambda} C_{ph}(\omega_{\lambda}) \cdot \left| \frac{\partial \omega}{\partial k_i} \right| \cdot MFP_{SL}$$
(13)

, where i specifies the direction of thermal transport, λ denotes the phonon mode, $C_{ph}(\omega_{\lambda})$ stands for the mode specific heat, ω is the angular frequency, and k is the wave vector. MFP_{SL} represents the total phonon mean-free path in the superlattice-like structure as defined elsewhere. ²⁶⁵

The simulated band flattening is considered to reduce the group velocities, $\left|\frac{\partial \omega}{\partial k_i}\right|$, of CLAPs, accounting for the κ diminishment in high-n samples. More intriguingly, a universal coherent phonon lifetime across n=1 - 6 is extracted to be ~ 100 ps, which corresponds to phonon MFPs of 7 nm for n=6 and 12 nm for n=1 in the cross-plane direction. The much larger MFPs than the interlayer spacing³⁰⁹ further highlight the wave-like properties of phonons in RP-phase 2D MHPs. The decreasing trend of MFPs, along with slowed group velocities as the thickness of the inorganic layer increases, demonstrates the reduction in κ dictated by eq. (13).

In addition to the direct measurements of κ , Raman spectroscopy serves as another powerful technique to provide insights into the partially coherent thermal transport nature in the 2D MHPs. Similar to their 3D counterparts, 2D MHPs exhibit low-frequency (between 30 cm⁻¹ and 100 cm⁻¹) LO and TO modes, corresponding to octahedral twists and distortions coupling to the organic cations, shown in the sharp Raman mode at 47.5 \pm 0.1 cm⁻¹ for an n=2 (BA)2(MA)Pb2I7 in **Fig. 11(f)**. Additionally, ultra-low-frequency modes have been identified by Raman spectroscopy below this region (< 30 cm⁻¹) and are attributed to the zone-folded longitudinal acoustic (zf-LA) phonons resulting from the superlattice-like layered structure of 2D MHPs. Signature 303,316 The periodically varying elastic properties in the cross-plane direction lead to periodic environment resembling the periodic potential wells experienced by electrons in crystals. Consequently, a phonon "Brillouin zone" is formed in the dispersion of phonons propagating along the direction of this discrete periodicity as illustrated in the calculated phonon dispersion diagram in **Fig. 11(f)**. The LA phonon branches extending out of the first Brillouin zone can then be zone-folded back to the first zone. These zone-fold behavior is widely observed and well-studied in superlattices. Si4,315,317,318

Evident in the calculated dispersions in **Fig. 11(f)**, two anomalous phonon properties arise from this phonon Brillouin zone picture. One is the presence of Raman-active LA modes with non-zero frequency at the zone center. The second is the emergence of phonon bandgaps (only for the longitudinal modes) in the dispersion for phonon wavelengths satisfying the Bragg condition.

These properties of LA phonons are widely observed in inorganic superlattices sharing a similar, layered structure. $^{317-319}$ Note that only the low-lying LA phonon branches experience the zone-folding effect, because LA phonons with high frequencies corresponding to wavelengths shorter than the period thickness will behave more particle-like and scatter off the interfaces instead of transmitting coherently and forming the phonon "Brillouin zone". Furthermore, higher n-value 2D MHPs with thicker inorganic layers (larger periodicity) were verified to also support the zf-LA mode, featuring a qualitatively same Raman spectrum with the n=2 MHP. 303 Notably from the n-number-dependent phonon dispersion relation in **Fig. 11(f)**, the optical phonon modes originating from the inorganic cage distortion redshift towards the bulk value in 3D MHPs, and the zf-LA phonon branches shift upward. It can thus be well anticipated that at higher n values, the softened optical modes and hardened acoustic modes begin to overlap, leading to more prominent phonon scattering, thereby lower κ . Also, at a high enough n value, i. i. large enough periodicity, the LA modes will no longer be observable in Raman as the periodicity becomes larger than the wavelength of the LA phonons. These arguments from Raman spectroscopic measurement align well with the thermal transport measurements discussed above.

4.4 Measuring anisotropic thermal transport

All the above-discussed thermal transport and Raman characterizations revealed a partially coherent nature of thermal transport in the cross-plane direction of 2D MHPs. Along the in-plane direction, where phonons propagate within each constituent layer, 2D MHPs are expected to exhibit higher κ , akin to other layered structures. However, the in-plane thermal transport has been less investigated than cross-plane transport due to the inherent low sensitivity of TDTR and FDTR to in-plane thermal transport (*i.e.*, caused by heat spreading in the metallic transducers), as well as a stringent requirement on the surface smoothness. Respectively with the surface smoothness, Respectively single crystals, remains a challenging topic.

Alternatively, measurements can be conducted on polycrystalline film of 2D MHPs, where the orientation of the layers relative to the substrate can be meticulously controlled through various deposition techniques. While spin-coated films generally favor a horizontal orientation – where the layers are parallel to the substrate, a vertical orientation with layers perpendicular to the substrate is sometimes more desirable because of the significantly better electrical conductivity and carrier mobility along the planes. TDTR and FDTR have been successfully applied to measure the in-plane κ of 2D MHPs on vertically oriented films. Nonetheless, the high density of grain boundaries and defects in films considerably impedes thermal transport, leading to challenges in accurately extracting the intrinsic anisotropic thermal properties of these materials.

Despite these challenges, methods other than TDTR or FDTR, such as LFA, TTG, and SThM as introduced in Section II have been utilized to measure the anisotropic thermal transport properties of 2D MHPs. 123,125,255,325 The exceptional directional sensitivity of TTGs allows for the detection of anisotropies in the lateral thermal transport near the surface. 126 An in-plane thermal conductivity (κ_{\parallel}) of (BA)₂PbI₄ single crystals was measured with TTG to be $0.28 \pm 0.01 \, \text{W} \cdot \text{m}^{-1} \cdot \text{K}^{-1}$ at 300 K, aligning well with MD simulation predictions. 123 Given that the cross-plane thermal conductivity (κ_{\perp}) predicted by the same MD simulation is $0.18 \pm 0.01 \, \text{W} \cdot \text{m}^{-1} \cdot \text{K}^{-1}$, it was concluded that (BA)₂PbI₄ exhibits a relatively low anisotropy ($\kappa_{\parallel}/\kappa_{\perp} \sim 1.5$) compared to van der Waals layered materials that exhibit tens or hundreds of anisotropic ratio. 320,321,323,326 In another work, simultaneous measurement of κ_{\parallel} and κ_{\perp} was achieved with cross-section SThM on a film of (PEA)₂PbI₄, and lower-than-expected anisotropy ($\kappa_{\parallel}/\kappa_{\perp} \sim 3.4$) was also found. 325 This minimal

anisotropy in 2D MHPs may be contributed by the CLAPs that are carrying substantial heat across the layer interfaces. Using DynaCool physical property measurement system (PPMS), which is based on steady-state methods, A. Mandal *et al.* measured the anisotropic thermal conductivity of a lead-free RP-phase 2D double perovskite, (PA)₄CuInCl₈ (PA = C₃H₇NH₃⁺), to be 0.15 W·m⁻¹·K⁻¹ and 0.28 W·m⁻¹·K⁻¹ in the cross-plane and in-plane direction, respectively.⁵¹ The measurement was conducted on highly oriented powder-compressed pellets, enabling the use of commercial instrument.

Beyond the organic-inorganic hybrid 2D MHPs, the thermal transport properties of all-inorganic 2D MHPs are also of great research interest. P. Acharyya *et al.* employed a commercial LFA instrument to measure both κ_{\perp} and κ_{\parallel} of high-quality, Bridgman-grown all inorganic 2D Cs₂Pb₂Cl₂ and Cs₃Bi₂I₆Cl₃ single crystals.^{255,327} As anticipated, all inorganic 2D MHPs show higher κ in both in-plane and cross-plane directions compared to organic-inorganic hybrid 2D MHPs. In addition, the absence of organic-inorganic interfaces, which introduce strong diffuse scattering of phonons particularly in the cross-plane direction, together with the weak interlayer interaction, result in a remarkably low thermal transport anisotropy of $\kappa_{\parallel}/\kappa_{\perp} \sim 1.1$. The κ of single crystalline and polycrystalline 2D MHPs measured with different techniques in either in-plane or cross-plane directions are summarized in **Table 3** and **Fig. 12**.

It is noteworthy that while LFA methods based on well-established commercial instruments offer a straightforward and fast-handed approach to measuring the thermal transport properties, the stringent requirement on the quality and size of the sample largely limits the applicability. Typical LFA instruments require the samples to be millimeters in both size and thickness, 48,50 which is nontrivial to meet for hybrid 2D MHPs. 292,328 Therefore, LFA is predominantly applied on powder-compressed pellets, which only reflect an effective isotropic $\kappa_{\rm eff}$. The circular markers in **Fig. 12** represent the effective $\kappa_{\rm eff}$ without any consideration of anisotropy.

4.5 Temperature-dependent thermal transport

At high temperatures (*i.e.*, temperatures above the Debye temperature), κ of semiconducting or insulating solids generally goes as an inverse relationship with temperature, *i.e.* $\kappa(T) \propto T^{-\alpha}$, due to strong phonon-phonon scattering.³²⁹ In a crystal where the thermal transport is primarily limited by the lowest-order three-phonon process (both Umklapp and normal scattering), a linearly inverse dependence is followed, *i.e.*, $\alpha = 1$. Practically however, thermal transport in typical inorganic bulk PV materials involves higher-order phonon-phonon scatterings involving more than three phonons, leading to a steeper temperature dependence, *i.e.* $1 < \alpha \le 2$. $2^{96,330,331}$

A higher value of α , which stands for a stronger temperature dependence, implies more prominent temperature-dependent phonon scattering. As discussed in the previous sections, anisotropic thermal transport arises in 2D MHPs due to the difference in dominating phonon scattering mechanisms in cross-plane and in-plane directions. In the cross-plane direction, the temperature-insensitive interface scattering plays a significant role in affecting the cross-plane κ , whereas in-plane thermal transport is dominated by the more temperature-dependent phonon-phonon scattering. The κ in either in-plane or cross-plane direction are thus expected to exhibit different extents of temperature dependence, with κ_{\parallel} showing stronger temperature dependence and changing more rapidly with temperature than κ_{\perp} . Although this behavior has not been reported experimentally for 2D MHPs to the best of our knowledge, it has been well studied by the same partially coherent model discussed in **Section 4.2** for superlattice. A representative

temperature-dependent κ in both in-plane and cross-plane directions of GaAs/AlAs superlattice calculated from this model is shown in Fig. 13(a).

Temperature dependence of κ could shed light onto the underlying complex phonon scattering process of thermal transport in 2D MHPs. However, it is challenging to conduct temperature-varying thermal transport measurements on 2D MHPs, especially on hybrid ones due to phase or structural transitions. For instance, (BA)₂PbI₄ goes through a structural phase transition featured by the shifting of BA⁺ cations relative to the inorganic layers at 274 K.⁴³ Such phase transitions lead to abrupt changes in thermal transport properties, such as jumps in κ and divergence in specific heat, thereby obscuring the intrinsic temperature dependence. Therefore, temperature-dependent measurements on 2D MHPs are typically limited to a relatively narrow range, in which case the temperature dependence, *i.e.* the form of $T^{-\alpha}$, is hard to extract.^{43,218,255,256}

By measuring the temperature-dependent thermal diffusivity of $(BA)_2PbI_4$ and $(PEA)_2PbI_4$ pellets with LFA, and the corresponding heat capacity with DSC, R.-I. Biega *et al.* obtained an almost constant κ of $\sim 0.135~W\cdot m^{-1}\cdot K^{-1}$ for $(PEA)_2PbI_4$ and $\sim 0.152~W\cdot m^{-1}\cdot K^{-1}$ for $(BA)_2PbI_4$ in a moderate temperature range of $300\sim385~K$ as summarized in **Fig. 13(b)**. Although the 3D counterpart, *i.e.*, MAPbI₃, undergoes a phase transition within this temperature range, 300~K is well above the transition temperature of both (BA)-based and (PEA)-based 2D MHPs. While a clear decreasing trend in the measured thermal diffusivities with increasing temperature was recognized, the corresponding increase in heat capacity compensates the trend, yielding a nearly invariant κ_{eff} , as dictated by eq. (2).

The evaluated $\kappa_{\rm eff}$ here are the effective values of the powder-compressed pellets, as opposed to values measured on single crystals or highly oriented films. 38,123,256,260 Moreover, the temperature range applied here is too small to accurately fit any $T^{-\alpha}$ dependence. In spite of the experimental difficulties, numerical methods such as MD simulations have been successfully applied to calculate the temperature-dependent κ_{\perp} of 2D MHPs in a relatively large temperature range, revealing a remarkably small temperature dependence for hybrid 2D MHPs, with $\alpha = 0.41$ for DJ-phase (4AMP)PbI₄ and $\alpha = 0.44$ for RP-phase (PEA)₂PbI₄ ²⁵⁷ as illustrated in **Fig. 13(c)**.

Temperature-dependent thermal transport measurements were also performed on allinorganic 2D MHPs. Although 3D all-inorganic MHPs suffer severe phase transitions even in ambient conditions, 332 a 2D all-inorganic RP-phase MHP, Cs₂PbI₂Cl₂ remains phase transitionfree over a large temperature range $(100 \sim 700 \text{ K})$, 333 making it a promising material to investigate the temperature-dependent thermal transport in 2D MHPs. Both κ_{\parallel} and κ_{\perp} of Cs₂PbI₂Cl₂ were measured in the temperature range of 295 \sim 523 K with LFA as shown in Fig. 13(d). 255 Temperature-dependent Raman spectra also revealed a decreasing phonon lifetime with increasing temperature, accounting for the decreasing κ . Interestingly, κ_{\parallel} shows a more prominent temperature dependence than κ_1 . This difference is consistent with the prediction made by the partially coherent thermal transport model, which states that cross-plane thermal transport that experiences more temperature-independent interface scattering should have a weaker temperature dependence than in-plane transport. This implies the potential existence of CLAPs in the allinorganic 2D MHPs. To this end, a quantitative analysis of the ratio of coherent and incoherent phonons responsible for the cross-plane thermal transport is theoretically possible through measuring the temperature-dependent κ_{\perp} and comparing the extent of discrepancies with both stacked-interface model and partially coherent model.

Another point to note is that $Cs_2PbI_2Cl_2$ intrinsically features higher κ in all temperatures than other hybrid 2D MHPs due to the absence of poorly conductive organic spacers separating the layers. Reduced acoustic impedance mismatch between adjacent layers also facilitates the thermal transport. Even so, $Cs_2PbI_2Cl_2$ still possesses much lower κ than other inorganic PV materials, originating from its layered structure, and strong anharmonic coupling between the acoustic phonons and flat, low-energy optical phonons. At the same time, the layered structure leads to a very low temperature dependence of $\kappa_{\perp}(T) \propto T^{-\alpha}$ with α much lower than other inorganic PV semiconductors, approaching the inorganic superlattices. Significantly, and strong an arrange of the layer of the same time, the layered structure leads to a very low temperature dependence of $\kappa_{\perp}(T) \propto T^{-\alpha}$ with α much lower than other inorganic PV semiconductors, approaching the inorganic superlattices.

An anomalous glass-like temperature dependance, $\alpha < 0$, was found in a (111)-oriented all-inorganic 2D MHP, Cs₃Bi₂I₆Cl₃ by P. Acharyya *et al.*.³²⁷ The κ below room temperature down to 2 K was measured using a physical properties measurement system (DynaCool PPMS) and thermal diffusivity from 300 to 400 K was measured by LFA to obtain the κ above room temperature. As shown in **Fig. 13(e)**, three counterintuitive features can be observed: (1) a deviation from the T^3 dependence at low temperature (below the Debye temperature); (2) the absence of a κ peak as present in general crystalline materials; and (3) a plateau in κ followed by a glass-like increase approaching the glass limit. The unexpected presence of these glass-like behaviors in single crystalline MHPs is attributed to low-frequency acoustic phonons and strong anharmonicity in the crystals.^{327,340}

4.6 Lower dimensionality

Lower-dimensional MHPs have been integrated into PV devices to achieve enhanced performance. $^{276,341-344}$ Further reducing the dimensionality of MHPs from 2D to 1D and 0D brings up different thermal properties. A decreasing κ is observed using SThM for all-inorganic MHPs as the dimensionality is reduced from 3D CsPbCl₃ (0.49 W·m⁻¹·K⁻¹) to 2D CsPb₂Cl₅ (0.40 W·m⁻¹·K⁻¹) and further to 0D Cs₄PbCl₆ (0.3 W·m⁻¹·K⁻¹) (**Fig. 14(a**)). 36,237 A 1D MHP, namely imidazolium lead iodide, (IMI)PbI₃, comprised of face-sharing octahedra chains was measured by LFA. 295 The porosity of the powder-compressed pellets necessitated by LFA was shown to influence the value of the measured κ , as evidenced by subsequent measurements in He and Ar atmosphere. After accounting for the dependence of κ on the porosity, effective "bulk" values of κ were extrapolated to be 0.156 W·m⁻¹·K⁻¹ that is almost constant in a temperature range of 300 ~ 500 K.

The low-toxicity and air-stable 0D Cs₃Bi₂I₉, which contains discrete face-sharing octahedra dimers [Bi₂I₉]³⁻ (**Fig. 14(b)**),³⁴⁵ are gaining substantial PV and photoelectric interests due to its excellent charge-transport properties despite the low dimensionality.^{346,347} As shown in **Fig. 14(b)**, a nearly temperature-independent low lattice κ of Cs₃Bi₂I₉ was measured to be ~ 0.20 W·m⁻¹·K⁻¹ within 30 ~ 523 K by LFA.³⁴⁸ At the lower temperature limit (< 30K), the κ is well-described by the Debye-Callaway model, with a peak (2.8 W·m⁻¹·K⁻¹) at 3 K. Notably, the κ at high temperature is approaching the diffusive κ limit (0.13 W·m⁻¹·K⁻¹) as indicated by the dashed line in **Fig. 14(b)**. This value ranks among the lowest κ for all-inorganic PV materials.³⁰⁰ Temperature-dependent Raman spectrum and DFT calculation revealed that this ultralow κ originates from (1) the soft crystal structure induced by the extended filled antibonding states near the Fermi level by Bi (6s) – I (5p) interaction; (2) the strong anharmonicity due to the bi-octahedral rotational and torsional modes; and (3) the strong coupling between the optical phonons associated with the Cs⁺ motion and the transverse acoustic phonon modes.

A similar lead-free 0D MHP, (MA)₃Bi₂I₉, has also been recognized as a potential candidate PV material. Due to its low toxicity and high stability, it has been adopted as the absorbing layer in replacement of or integrated with MAPbI₃. 342,349 An analogously low κ of $\sim 0.2~W \cdot m^{-1} \cdot K^{-1}$ insensitive to temperature change from 300 to 450 K was measured by LFA (**Fig. 14(c)**). 218,300 Similar to the isostructural Cs₃Bi₂I₉, the soft phonon dispersion, strong optical-acoustic phonon coupling and thus short phonon lifetimes, and weak chemical bonds all contribute to the poor thermal conduction in (MA)₃Bi₂I₉.

Another type of lead-free 0D MHP, [Mn(C₂H₆OS)₆]I₄, with a more preferable bandgap (1.6 eV) than both Cs₃Bi₂I₉ and (MA)₃Bi₂I₉ (~ 2 eV) for PV uses, is also found to exhibit a substantially low κ of 0.15 \pm 0.01 W·m⁻¹·K⁻¹ from 300 to 375 K.³⁵⁰ Moreover, the extending ligands on each individual [MnO₆]⁸⁻ octahedra interact to form a 3D supramolecular network through hydrogen bonding, resulting in effectively anisotropic thermal transport. By employing 3ω method on a highly oriented film, the in-plane κ_{\parallel} was consequently measured to be 0.21 \pm 0.01 W·m⁻¹·K⁻¹ at room temperature and rapidly decrease to ~ 0.08 W·m⁻¹·K⁻¹ at 345 K.

V. Compositional Origins of the ultralow thermal conductivities of MHPs

In general, the MHPs families, from 3D to 0D, exhibit significantly low thermal conductivities. Despite the difference in their crystal structues, dimensionalities, and compositions, similar phonon behaviors are common among them that contribute to their poor thermal conductive properties. While 3D MHPs features a general formula of ABX₃, quasi-2D perovskites have a more complex composition, $A_2A_{n-1}B_nX_{3n+1}$.

To provide guidance on thermal property tailoring by chemical engineering, in this section, we will present a general view of how the thermal transport properties of MHPs are related to their constituents. From Section 3.3, we discussed the dominating role of $[BX_6]^{4-}$ octahedral cages in influencing the thermal conductivities of 3D MHPs. Although by switching thee A-site cations from organic to inorganic ones (e.g., from MAPbI₃ to CsPbI₃), slightly higher thermal conductivity can be obtained, the values still lies within a low region. This behavior is not unique to 3D MHPs but a common trend found also in 2D MHPs. The low anisotropic ratio ($\kappa_{\parallel}/\kappa_{\perp}$) of quasi-2D MHPs compared with other layered materials, as discussed in Section 4.4, can be partially attributed to this feature. Whearas thermal transport along the in-plane direction usually features a much faster rate than that in cross-plane direction, the heat flow within the inorganic layer in 2D MHPs is still greatly hindered by the intrinsic poor thermal conductance of the octahedral network. Understanding the contributions of $[BX_6]^{4-}$ octahedra, and also the A-site (also A'-site) cation in the system will help provide more insights to the chemisists in engineering the thermal transport properties.

5.1 Role of A-site cation and $[BX_6]^{4-}$ octahedra

The correlation between heat transfer and phonon behavior is important for understanding the low κ of MHPs. Materials' phonon dispersion can be determined through inelastic scattering experiments or first-principle calculations to provide more wholistic information for understanding the roles of each constituents in thermal transport.

As discussed in **Section 3.3**, a decreasing trend in κ is observed when heavier halides (X⁻) is included, i.e., $\kappa_{Cl} > \kappa_{Br} > \kappa_{I}$. Such a trend can be well explained from the perspective of phonon behaviors. A. C. Ferreira *et al.* conducted coherent inelastic neutron scattering spectroscopy and

Brillouin light scattering to investigate the low-frequency acoustic phonons in several MHPs.³⁵¹ The speed of longitudinal acoustic (LA) and transverse acoustic (TA) phonons in different MHPs can be fitted from the slope of the acoustic phonon dispersion (**Fig. 15(a)(b)**). With the experimentally fitted phonon velocities, a complete set of elastic constants such as C_{11} , C_{44} , C_{12} and the bulk modulus were further deduced as listed in **Fig. 15(c)**. Their significant finding was that among these elastic constants, C_{44} is extremely small, which is likely related to the rotation and tilting of the Pb-X octahedra.³⁵² This finding revealed the dominating role of $[BX_6]^{4-}$ phonon modes in regulating the thermal transport.

Using inelastic neutron scattering, B. Li *et al.* investigated the atomic dynamics in MAPbI3 and revealed that the dynamics of A-site MA⁺ primarily influence the optical phonon properties of the material. Specifically, they distinguished the jumping rotational modes of MA⁺ in the orthorhombic phase, as well as an optical phonon mode related to the orientational disorder of MA⁺, which appears after the orthorhombic-to-tetragonal phase transition. The emergence of this orientational disorder reduces the relaxation time of the jumping mode by an order of magnitude. While the contribution of optical phonons to heat transfer is generally considered to be minimal, given their sub-ps lifetime and nearly zero group velocity, in the case of MAPbI3, optical phonons can indirectly influence the lifetime of acoustic phonons (from 5.4 ps to 3.61 ps) by phonon-phonon interactions, ultimately reducing κ . This explains the experimentally observed sudden change in κ during the orthorhombic-tetragonal phase transition of MAPbI3 from a microscopic perspective.

Numerical simulations were also employed to shed lights onto the origins of low κ in 3D MHPs. S. Yue *et al.* examined the effective phonon dispersions of the inorganic cages of MAPbI3 by freezing the A-site MA⁺ cations.²³³ Nonequilibrium *ab initio* MD simulations indicate that MA⁺ significantly influences the vibrational modes of the inorganic cages, although these effects are predominantly observed in the higher energy regions (**Fig. 15(d)**). In contrast, the impact of A-site organic cations on the low-energy phonon spectrum can be considered negligible, which supports the claim that low κ is an intrinsic characteristic of the octahedral network. DFT calculations further discovered that clusters composed of Pb and I atoms are important phonon scattering sources in the low-frequency region.²³⁵ The complex scattering mechanism results in a phonon MFP below 10 nm in many MHPs, *e.g.*, as low as 3.9 nm in CsSnI₃ and 5.6 nm in CsPbBr₃.²³⁵ Combining the BTE and DFT, the cumulative κ with respect to phonon MFPs was calculated (**Fig. 15(e)**).²³⁵ In the kinetic theory, the κ as a function of volumetric phonon heat capacity C, average group velocity v_g , and average MFP of phonons $\bar{\Lambda}$ is expressed as:^{34,247}

$$\kappa = \frac{1}{3}Cv_{\rm g}\bar{\Lambda} \tag{14}$$

With this relation, the experimental average MFP can be estimated if the velocity of phonon and heat capacity are known. Surprisingly, when the experimental data are organized by plotting κ as a function of Cv_g , the various 3D MHPs align quite linearly (**Fig. 15(f)**).³⁴ This suggests that all the 3D MHPs share a similarly low $\bar{\Lambda}$ less than 10 nm, and, importantly, that variations in κ among MHPs stem largely from differences in the sound speeds.

As for the layered quasi-2D MHPs, besides the layered interfaces that serve as extra phonon scattering sources in the system compared with their 3D counterparts, $[BX_6]^{4-}$ octahedra still play a crucial role in determing the phonon behaviors, in turn the thermal transport properties. The phonon modes of $(C_xH_{2x+1}NH_3)PbI_4$ (x = 4 - 9) in the range below 100 cm⁻¹ are predominantly

attributed to the motions of the Pb-I cage, as determined by investigating the influence of organic chain length on phonon spectrum with Raman spectroscopy (**Fig. 16(a**)). ²⁹⁹ Despite the high volumetric ratio of the organic sublattice in 2D organic-inorganic MHPs ($\sim 78\%$), the motion of the alkylammonium chain is shown to be primarily driven by the pulling of the heavy halide ions through Coulombic interactions and hydrogen bonding. This dynamic nature results in an almost invariant phonon mode frequency even when the organic chain length is doubled. Evidently, the halide ions dominate the overall vibrational modes, which suggests the feasibility of phonon engineering on both 3D and 2D MHPs, and consequently κ modification, by altering the [BX₆]⁴ cages (e.g., constituents, connectivities, and distortions).

For instance, an effective κ of $0.33 \pm 0.02~W \cdot m^{-1} \cdot K^{-1}$, along with a thermal diffusivity of $0.3 \pm 0.1~mm^2 \cdot s^{-1}$ and a small heat capacity of $0.18 \pm 0.6~J \cdot g^{-1} \cdot K^{-1}$ were measured and mapped simultaneously with 3ω -based SThM on thin film CsPb₂Br₅.²³⁶ In contrast, the effective κ of 2D CsPb₂Cl₅ was measured to be $0.40~W \cdot m^{-1} \cdot K^{-1}$.³⁶ The higher κ in chloride-based 2D MHPs compared to the bromide-based ones aligns with the general trend that lighter halide ions lead to higher κ as observed in most MHPs regardless of dimensionalities.

5.2 Role of A'-site organic spacers in 2D MHPs

In spite of the common roles of $[BX_6]^{4-}$ in contributing to the low κ of MHPs, 2D (and quasi-2D) MHPs are subject to the impact of another constituents, A-site spacers. In **Section IV**, we primarily discussed the structural origins of the ultralow κ in 2D MHPs, which is even lower than their 3D counterparts due to the introduced interfacial scatterings. Here the intrinsic influences of the A'-site spacers are discussed, which can serve as another dimensionality to engineer the thermal transport properties of 2D MHPs. Note that we will primarily focus on the roles of organic spacers in hybrid 2D MHPs, as all-inorganic 2D MHPs with inorganic A'-site spacers generally contain mixed halides to form a stable structure (examples in Section 4.4 & 4.5) and the sole effect of spacers are hard to distinguish.

Despite the insignificant role of organic-spacer lengths in dictating the thermal transport properties of 2D hybrid MHPs, 256,299 the lateral spacing and rigidity of the organic spacers were found to induce considerable changes in κ . 257,316,354 As shown in **Fig. 16(b)**, MD simulations predict drastically increased κ in both the in-plane and cross-plane directions when the lateral distance between the adjacent organic chains is decreased. 257 The lateral van der Waals interactions between the organic chains contribute to the stiffness of the organic layer. The enhanced κ arises from the vibrational hardening, *i.e.* higher vibrational frequency, of the organic layer due to the increased van der Waals interactions at closer distances. 316 Experimentally, the lateral distance between the organic chains in the spacer layer can be tuned by varying the organic cations inside the inorganic subphase, or other constituent elements, thereby allowing synthetical manipulation of the metal-halide bond lengths, which in turn modifies the organic chain spacing. 290

The rigidity of the organic spacer molecules also plays a crucial role. 2D hybrid MHPs with aromatic groups as spacers, e.g. (PEA)₂PbI₄ and (PEA)₂PbBr₄, were measured to have higher thermal diffusivities than those with alkyl chain groups, ^{38,257} originating from the increased rigidity of organic spacer molecules via strong π - π bonding that facilitates faster energy transport³⁵⁵ and decreases the phonon dephasing rates, *i.e.*, weakens the phonon anharmonicity. ^{43,354} Temperature-dependent phonon dephasing rates of (PEA)₂PbBr₄ and (BA)₂PbBr₄ were simulated with MD from 50 K to 300 K (**Fig. 16(c**)). A smaller phonon dephasing rate across all temperatures for (PEA)₂PbBr₄ was present, indicating smaller anharmonicity. Additionally, the phonon dephasing

of $(BA)_2PbBr_4$ showed very weak temperature dependence, which was attributed to the more significant disorder in its lattice, quantified by the spatial correlation relation between the nitrogencarbon dipoles as $C(r) = \langle \mu(0) \cdot \mu(r) \rangle$. Here μ is the dipole moment separated by a distance of r. As shown in Fig. 16(c), the lower long-range correlation in $(BA)_2PbBr_4$ implies a more amorphous packing which is responsible for its temperature insensitive phonon relaxation rate. Note that although PEA-based 2D MHPs generally exhibit larger thermal diffusivities than the BA-based counterparts, the thermal conductivities are mostly the opposite trend. The origin of this discrepancy is that thermal diffusivity and thermal conductivity are two properties describing different aspects of thermal transport. Thermal diffusivity is a measure of speed or rate of heat flow, and mainly correlates to how quickly the materials respond to temperature change. On the other hand, thermal conductivity is a measure of ability to conduct heat, which is about the magnitude of heat flow rather than speed, and influenced by other material properties such as density and heat capacity as in eq. (2).

For RP phase 2D MHPs wherein monovalent cation spacers are included, the interaction strength at the interfaces of two spacers were shown to have significant influence on both thermal and mechanical behaviors of the materials. 259,356 While a positive correlation between elastic modulus and κ are usually observed for soft materials, ^{357,358} by engineering the interactions between spacers, A. Negi et al. achieved an anomalous correlations, i.e. anti-correlation and uncorrelation, between these two properties as summarized in Fig. 16(d).²⁵⁹ Grounded in the tendency that stronger interactions at the interfaces generally lead to improved thermal transport across the interface (i.e. higher interfacial thermal conductance), ^{267,358,359} and higher stiffness (i.e. larger elastic modulus), ³⁶⁰⁻³⁶² independent modification on the thermal and mechanical properties of 2D RP MHPs were managed by choosing the bonding types and ratios at the spacer interfaces. When both alkyl and aryl spacers are present, possible interactions at the interfaces include van der Waals (alkyl-alkyl), CH- π (alkyl-aryl), and π - π (aryl-aryl) with increasing strengths. Hard but thermally insulative or soft but thermally conductive 2D MHPs exhibiting anti-correlation can thus be designed through tailoring the spacer interactions by mixing different spacers, as illustrated in the yellow marked materials in Fig. 16(d). Furthermore, introduction of chiral spacers was found to affect the structural and molecular packing, and also induce diverse orientations of phenyl rings, which contribute collectively to almost constant (uncorrelated) κ with increased elastic modulus.

VI. Other third-generation photovoltaic materials

Beyond MHPs, thermal transport measurements of other third-generation PV materials, such as zero-dimensional (0D) quantum dots and environmental-friendly copper zinc tin sulfide (CZTS), are summarized in this section. We note that the thermal transport properties of conventional PV materials, such as silicon, GaAs, cadmium telluride (CdTe) and copper indium gallium (di)selenide (CIGS) have been extensively studied with the steady-state heat flow, ^{336,363} laser flash, ^{42,364} and photoacoustic methods. ^{334,365,366}

6.1 Quantum Dots (QDs)

As a branch of third-generation PV materials, colloidal quantum dots (QDs) hold promise for exceeding the Shockley-Queisser single-junction limit through the more efficient multiple carrier generation.³⁶⁷ Various materials in their QD form have been successfully integrated into solar cells, such as PbS,³⁶⁸ PbSe,³⁶⁹ CdTe,^{370,371} CdSe,^{370,372,373} CdS ^{373,374} and graphene.³⁷⁵⁻³⁷⁸

The phonon bottleneck effect, which slows the hot carrier cooling rate, can facilitate the impact ionization effect for multiple exciton generation in these materials, potentially resulting in higher PV efficiency. Such effect was first reported for CdSe QDs^{379,380} and later also observed in hybrid MHPs.²⁹⁴ As mentioned in previous sections, a stronger phonon bottleneck effect could benefit from the low κ of the materials. On the other hand, the low κ of QDs also presents challenges for heat dissipation in practical solar cells and LEDs with high operating temperatures to ensure a longer device lifetime and more stable performance.³⁸¹⁻³⁸³ The low κ and appropriate electrical conductivity also make them favorable for thermoelectrics.³⁸⁴ Despite numerous efforts on measuring the electrical transport properties of QDs, research focusing on their thermal transport properties remains relatively limited,^{170,385-397} yet equally important for both better thermal managements and PV performance.

6.1.1 Metal chalcogenide QDs

Two features that significantly influence the thermal transport properties of QDs or nanocrystals (NCs) comes with the intrinsic low dimensionality (several digits of nm in sizes). One is the increased heat capacity due to increased surface-to-volume ratio, 395,398,399 second is the high density of organic/inorganic interfaces between the ligands and cores, 400 both of which will largely suppress the thermal transport. The first systematic investigation on the thermal transport properties and influencing factors is credited to W.L. Ong *et al.*, who measured ultralow κ of several NCs using FDTR and managed a high tunability on thermal transport properties by modifying the surface chemistry. 390

Besides the poor thermal conductive nature of QDs (NCs), multiple factors have been reported to influence the thermal transport properties, among which the size effect is a most prominent factor. As shown in **Fig. 17(a)**, QDs (NCs) with larger particle sizes exhibit higher κ , 391,396,401 which is attributed to the decreased heat capacity, 390,395 and interface density. Concurrently, the sound speed and phonon MFPs were also found to increase with sizes, all the above contributions lead to an over 100% enhancement in κ of PbS NC superlattice, from 0.32 W·m⁻¹·K⁻¹ to 0.75 W·m⁻¹·K⁻¹, when the diameters of PbS NCs increase from 3 nm to 6.1 nm. Similarly, highly grain-size dependent κ of CdSe NC films were measured to range 0.2 \sim 0.45 W·m⁻¹·K⁻¹ for grain sizes within 3 \sim 6 nm, the value of which is notably lower than the amorphous limit. The greatly suppressed thermal transport and strong size effect of κ suggest the dominant role of boundary scatterings in these systems.

In addition to the particle sizes, other factors also provide approaches to engineer the thermal transport properties of QDs (NCs), such as the ligand chemistry. Modification of the surface chemistry by exchanging the ligands is vastly applied to enhance the electrical properties of QDs, $^{402-404}$ and is also found to greatly influence the thermal transport properties. 389,390,405 The ligand chemistry may influence the overall κ in different ways as summarized in **Fig. 17(b)**. Firstly, the weak ligand-ligand interaction strength is considered as the primary limiting factors for efficient thermal transport. 389 The organic ligands connect with the inorganic core by strong covalent bonding, while the ligands interact with each other or the environment with relatively week van der Waals bonding. $^{406-408}$ Empirically, the rate of thermal transport across these interfaces scales with the interaction strength, *i.e.* stronger interaction at the interfaces should result in a larger interfacial thermal conductance. 359 While it was found that with careful choices of ligands to strengthen the ligand-ligand interactions, κ of PbS QDs films was enhanced by up to 150%, little effect of ligand-core interaction or κ of cores was shown. 389,390 Secondly, in a system where QDs are dispersed in a matrix solvent, interaction between the ligand and environments

provides another dimension to modify the thermal transport. Solvent with better solubility and more matching vibrational energies with the ligands were shown to facilitate the cooling of QDs by efficiently taking the heat away. Exchanging the organic ligands with inorganic chalcogen ligands, such as Se^{2-} , enables simultaneous enhancement in electronic and mechanical coupling between the QDs and environments, leading to better electrical conductivity and faster heat dissipation. Moreover, even if the ligands have the same chemistry characteristics, simply altering the length of the ligands to modify the spacing between cores will modify thermal transport properties, wherein a higher κ is observed for smaller spacing. Wherein a higher κ is observed for smaller spacing. Other factors such as the long-range ordering, and ligand grafting density also influence the thermal transport in QDs (NCs), with κ in ordered PbS NC superlattice up to \sim 3 times higher than randomly oriented films, and larger interfacial thermal conductance between the core and ligands in QDs with larger ligand grafting density. 266,389,397

The predominant role of ligand-ligand and ligand-environment interaction, and negligible effect of the core properties on the overall κ were explicitly verified by Y. Liang *et al.* using an infrared-pump-electronic-probe (IPEP) spectroscopy,³⁹⁷ which is a similar technique to VPVP as discussed in Section 3.2.4. By vibrationally exciting the C-H bond in the ligands with an ultrashort infrared laser, the heat flow across the ligand/core and ligand/environment interfaces during the heat-cool period of CdSe QDs were monitored by the transient absorption redshift of CdSe core using a visible probe light.^{392,393} In contrast to other works discussed here that measure the overall thermal transport of the entity, this ultrafast spectroscopic method distinguishes the thermal transport across the core/ligand and ligand/solvent interfaces in the QDs suspensions. As expected from the distinct bonding energies between the covalent and van der Waals bonds, the interfacial thermal conductance between the oleate ligand and CdSe core, $h_{NC-lig} \approx 103 \text{ MW} \cdot \text{m}^{-2} \cdot \text{K}^{-1}$ was found to be almost an order of magnitude higher than that between ligands and solvent, $h_{lig-sol} \approx 14 \text{ MW} \cdot \text{m}^{-2} \cdot \text{K}^{-1}$ for a broadband of grafting densities and sizes as illustrated in Fig. 17(c).³⁹⁷ The finding again attributed the ligand-solvent interaction as the bottleneck to thermal transport in QDs matrices.

6.1.2 Graphene ODs

As metal sulfides and metal selenides QDs have been the prevailing focus on the photovoltaics, another promising carbon-based QDs, graphene QDs (GQDs), are emerging for their advantageous features such as low toxicity, excellent biocompatibility and high photostability 375,377 . In addition to their wide applications as absorbers, 410 carrier transport layers 376,411 and sensitizers 412,413 in solar cells, their intrinsically ultra-high κ makes them potential candidates for thermal management layers. 388,414 One of the primary configurations of incorporating QDs into solar cells is to disperse the QDs in the electron/hole conducting polymers, 23,415 which can alter the effective thermal transport properties. Therefore, instead of exploring the thermal transport in bare GQDs, 388,416 researchers focus more on the properties when GQDs are in suspended forms or form a composite with other polymers. The enhancement in κ when GQDs are added are summarized in **Fig. 17(d)**.

Nanofluids, formed by suspended nanoparticles in a base fluid, have shown their superiorities in applications in solar energy systems. 417 The small particle sizes, thus the high surface area, lead to significantly increased specific heat, favorable for solar collectors. The presence of nanoparticles also enhances the κ of base fluids, which helps achieve improved thermal management in these systems. Dispersing GQDs in nanofluids has been shown to considerably

increase the κ of base fluids. ⁴¹⁸⁻⁴²⁰ Enhancements of as much as 53%, 21% and 18% in the κ have been achieved with 0.5%wt GQDs suspended in water, ethylene glycol, and a 6:4 water/ethylene glycol mixture at 323 K, respectively. ⁴²⁰ A concentration dependence revealed an increase in κ enhancement from 5% to 7% when the concentration of GQDs in car radiator coolant varies from 100 to 500 ppm. ⁴¹⁹ Apart from increased κ , a massive enhancement in the electrical conductivity (up to 140 times) was also reported for GQDs dispersed in distilled water. ⁴¹⁸ Besides GQDs nanofluids, composites formed with GQDs dispersed in polymers also exhibit superior thermal transport performance. Enhancements of up to 144% in κ , as well as 260% in toughness, have been found for 5%wt loading of GQDs in epoxy. ^{170,421} Furthermore, by carefully mixing graphite with different thickness and lateral sizes in a specific ratio, the κ of epoxy can be enhanced by a record-high value of 2300%. ⁴²²

6.2 Copper zinc tin sulfide/selenide (CZTS/Se)

Another class of third-generation PV materials attracting much attention are Cu_2ZnSnS_4 (CZTS) and $Cu_2ZnSnSe_4$ (CZTSe). CZTS and CZTSe are considered promising alternatives to CIGS due to a replacement of the rare indium and gallium with the non-toxic and earth-abundant zinc and tin. Compared with other all-inorganic PV materials, CZTS/Se feature a remarkably low κ , making them also potential candidates for thermoelectric applications. A23-425 Note that although single crystalline CZTS/Se were measured and calculated to have much higher κ than thin films, PV uses.

CZTS, also referred to as the kesterite, usually forms a stable crystallographic structure of ordered tetragonal (space group *I*-4), which evolves into a disordered tetragonal structure (*I*-42m) above 532 K through a reversible phase transition. We have 1 W·m⁻¹·K⁻¹ were found for tetragonal CZTS over a wide temperature range from 80 to 700 K by various methods, specifically 3ω , 423,429 TDTR, 430 and LFA. 428,431 The low κ are generally attributed to the crystal complexity of the quaternary compounds and the abundant presence of defects, mainly cationic disorders and vacancies.

Additionally, a disordered cubic phase CZTS that remains stable at temperatures up to 650 K can be synthesized by high-energy mechanical alloying. Such an uncommon phase of CZTS was found to exhibit largely suppressed (\sim 3 times reduction) and temperature-insensitive κ in the temperature window below 650 K as present in Fig. 18(a). Above 650 K, it goes through a phase transition back to the tetragonal phase. More intriguingly, an over 2-fold enhancement in electrical conductivity was simultaneously achieved in CZTS when transformed into the cubic phase. The peculiar behavior was attributed to the strong localization of s^2 lone pair electrons in some Sn atoms that (1) leads to Sn ions rattling, evident in the low frequency optical phonon modes via which lattice energy dissipates; and (2) causes p-type doping-like effect with highly localized acceptor levels originating from the presence of charge-deficient Sn-S bonds.

For tetragonal CZTS, a flexible tunning (either increasing or decreasing) of its κ can be achieved via manipulating defect concentrations. By sulfurizing CZTS thin films to reduce the number of sulfur vacancies, a 4.5-fold increasement in κ at room temperature was achieved, from 0.9 to 4.0 W·m⁻¹·K⁻¹.⁴²⁹ Such enhancement is even more prominent under low temperatures, reaching a peak κ of 6.8 W·m⁻¹·K⁻¹ at 145 K (**Fig. 18(b)**). Thermal treatment after the film growth can also modify the thermal transport properties by introducing a higher degree of cation disorders.⁴³⁰ While the standard ordered CZTS films were measured to exhibit a κ of 0.69 W·m⁻¹·K⁻¹ with TDTR, the highly disordered crystals produced by thermal annealing under different

temperatures show lower κ , spanning $0.38 \sim 0.54~\rm W\cdot m^{-1}\cdot K^{-1}$ as summarized in Fig. 18(c). The structural disorder from the stacking faults as well as the inhomogeneity from randomly ordered cations were found to contribute to the reduced κ . At the same time, introducing excess ZnS during synthesis to grow Zn-rich CZTS can further modify the density of crystallographic defects, achieving a remarkable tunability in κ of carefully engineered CZTS films from as low as 0.4 W·m⁻¹·K⁻¹ to as high as 0.8 W·m⁻¹·K⁻¹ (Fig. 18(c)). Incorporating metal nanoparticles such as Ag and Cu has been a common strategy to modify the thermal and electrical conductivities of semiconductors. A small addition of Ag nanoparticles into CZTS was shown to suppress thermal transport through enhanced phonon scattering originating from the increased grain boundaries while simultaneously increase its electrical conductivity. Further addition of Ag nanoparticles, on the other hand, facilitates thermal transport because of the large intrinsic κ of Ag as shown in Fig. 18(d). As for CZTSe, although sharing similar crystallographic structure and properties to CZTS, CZTSe generally feature higher κ due to the softer phonon modes and thus longer phonon lifetime.

VII. Summary and Outlook

Third-generation PV materials, particularly MHPs, semiconducting QDs, and CZTS/Se, are emerging as promising candidates to supersede conventional solar cells in large-scale applications. Despite advantageous electrical and optical properties, the ubiquitously low thermal conductivities observed in these materials present formidable challenges in efficient heat dissipation during practical uses. Effective thermal management is pivotal to mitigating heat accumulation, which can precipitate thermal degradation, curtailed operational lifespan, diminished stability and reduced efficiency. Consequently, there has been a paradigm shift from solely enhancing electrical transport to a more holistic approach that also emphasizes the significance of thermal transport in these materials. The development of more precise and versatile measurement techniques, along with a thorough understanding of thermal transport, are essential for formulating strategies to enhance thermal management, thereby achieving higher efficiency and more stable device performance.

Motivated by these considerations, we presented a comprehensive review of the techniques widely employed to measure the thermal transport properties of various third-generation PV materials. We elucidated and compared the working principles, application conditions, sample requirements, specialties, and data interpretation of various photothermal and electrothermal methods. While electrothermal methods boast a longer developmental history and ease of implementation, the non-contact and more versatile optical methods offer robust and flexible approaches to measure various types of materials, extending beyond photovoltaics, and encompassing a broad spectrum of properties beyond thermal transport. In addition to the methods we discussed here, the innovation of novel optical methods for thermal transport measurement that provides both temporal and spatial resolution, such as thermal imaging, represents a burgeoning field that will pave the way for advanced thermal management from macroscopic to microscopic scales.

From a materials perspective, we delved into the fundamental origins of the ultralow thermal conductivities of these third-generation PV materials. The inorganic octahedra in both 3D and 2D forms of MHPs play a predominant role in determining the phonon dispersions and vibrational modes, which in turn influence the thermal transport properties. This characteristic permits thermal

property engineering by adjusting the constituent metal and halide ions. Lower-dimensional 2D MHPs exhibit stronger exitonic effects, higher moisture stability and improved structural diversity over their 3D counterparts. However, the high concentration of organic/inorganic interfaces in the layered structures of 2D MHPs further impedes thermal transport in the cross-plane direction, rendering efficient heat dissipation more challenging. Strategies to address the low thermal conductivity of the broad MHPs family include phonon engineering through constructing phononic structure,⁴³⁸ composition modification on the [BX₆]⁴⁻ octahedra,^{36,301} and morphology tailoring of the film by controlling the grain sizes and orientations. 9,150,439,440 Unique to quasi-2D MHPs, thermal transport can be enhanced by augmenting the portion of heat carried by the coherent longitudinal acoustic phonons through phonon band structure engineering, similar to the approach used in superlattice. 263,317 Additionally, exploiting the anisotropic nature of the structure can facilitate faster heat transfer in the in-plane direction, analogous to the accelerated charge transport observed along this direction.⁴⁴¹ Furthermore, the structurally and compositionally more complex 2D MHPs offer greater flexibility to independently modulate their thermal transport, optical, electrical, and mechanical properties. 257,259,289 Apart from enhancing the intrinsic thermal conductivity of MHPs, strengthening their mechanical coupling with adjacent layers in devices (e.g., ETL and HTL) through interfacial toughening can also promote better heat dissipation. This approach not only improves thermal management but also enhances PV efficiencies by simultaneously boosting charge transport across the contact interfaces. 442-444

Metal chalcogenide QDs, akin to 2D MHPs, exhibit tunable optoelectronic properties through scalable quantum confinements. Despite the shared origins of ultralow thermal conductivities with 2D MHPs, *i.e.* organic-inorganic interfaces, the thermal transport properties of QDs are predominantly influenced by the organic ligands, including their lengths, functional groups, solubility to the solvents and rigidity. Surface chemistry modification through different ligand choices provides a potential approach to tune the thermal properties of QDs. Conversely, graphene QDs possess relatively high thermal conductivities, promising superior thermal management when integrated into a matrix material. The low thermal conductivities of CZTS/Se, attributable to the high level of cation disorder in their complex crystal structures, can also be managed by defect engineering or phase control.

In summation, measuring and comprehending the thermal transport properties of third-generation PV materials are as pivotal as the optoelectronic properties for further advancing PV performance. While the intrinsically poor thermal conductance of these promising materials imposes challenges for more efficient heat dissipation in applications such as solar cells, LEDs, photodetectors and other electronics and optoelectronics, various strategies have been proposed to surmount this limitation. Meanwhile, low thermal conductivities could be advantageous for enhanced phonon bottleneck effects that elevate PV efficiencies, and for other energy applications such as thermoelectrics. These factors underscore the imperative for more sophisticated thermal management strategies in these materials.

Data availability

Data sharing is not applicable to this article as no new data were created or analyzed in the study.

Acknowledgements

This material is based upon the work supported by the National Science Foundation under Grant DMR-2313648.

Author contributions

D.C., S.L. and B.L. wrote the manuscript under the supervision of P.G.. P.G. edited the manuscript.

Conflict of interest: The authors have no conflicts to disclose.

Correspondence and requests for materials should be addressed to Peijun Guo.

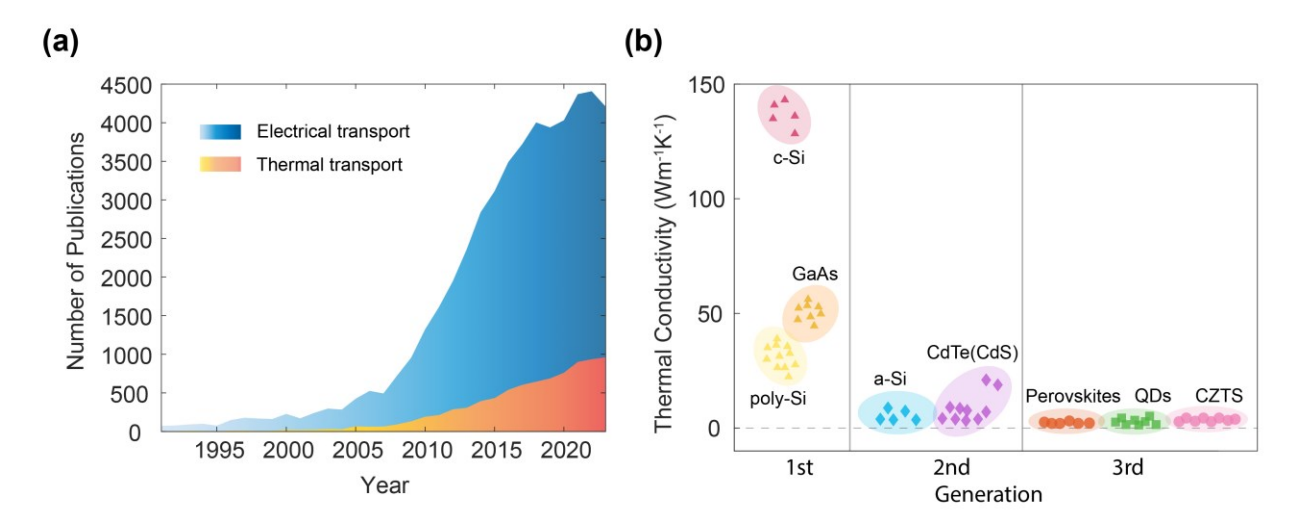


FIG. 1. (a) Number of publications on the electrical (blue) and thermal transport (orange) measurement and properties of photovoltaic materials as a function of years. (b) Thermal conductivity ranges of the first-, second-, and third-generation photovoltaic materials. c-Si: single crystalline silicon. poly-Si: polycrystalline silicon. a-Si: amorphous silicon. QDs: quantum dots. CZTS: copper zinc tin sulfide.

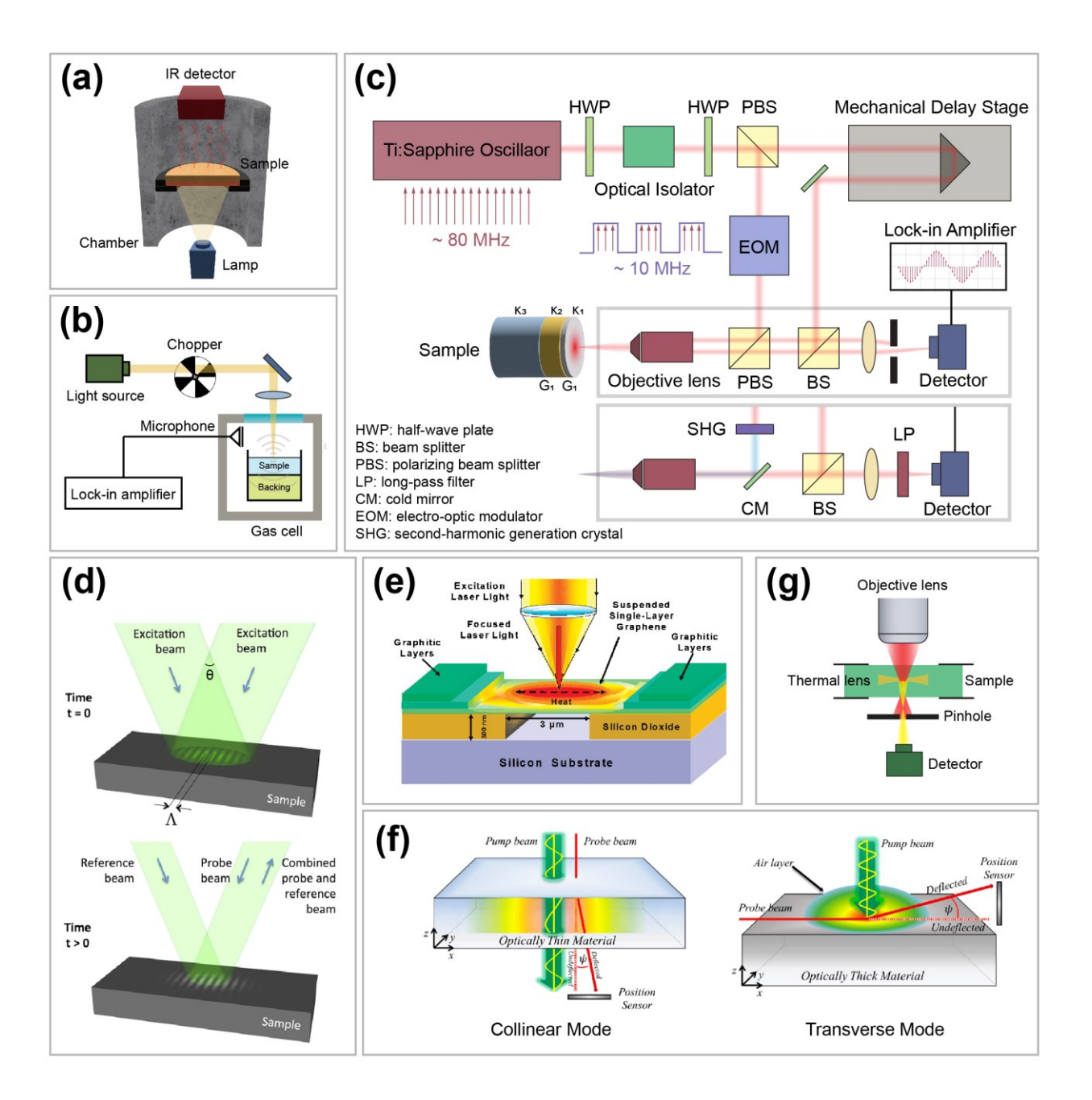


FIG. 2. Schematics of photothermal-based thermal transport measurement techniques (a) Laser flash analysis (LFA). (b) Photoacoustic spectroscopy (PAS) with front-surface illumination and using a microphone as the sensor. (c) Time-domain thermoreflectance (TDTR) with spatially separated (upper boxed panel) or spectrally separated (lower boxed panel) pump and probe beams. (d) Transient thermal grating (TTG). Upper panel: absorption grating with a periodicity of Λ excited by two overlapped pump beams at an angle of θ . Lower panel: transient detection of the resulting thermal grating by a reflected probe beam. Reproduced with permission from Sci. Rep. 5, 16042 (2015). Copyright 2015 Springer Nature. (e) Optothermal Raman spectroscopy (OTRS) on a graphene monolayer suspended across a trench. Reproduced with permission from Nano Lett. 8, 902-907 (2008). Copyright 2008 American Chemical Society. (f) Photothermal deflection

spectroscopy (PDS) in collinear mode (left panel) for transparent materials and transverse mode (right panel) for opaque materials. Reproduced with permission from Appl. Sci. 9, 1522 (2019). Copyright 2019 Authors, licensed under a Creative Commons Attribution (CC-BY) license. (g) Thermal lens spectroscopy (TLS). A diverging thermal lens formed inside the sample deflects (defocuses) the light, allowing it to pass through the pinhole and be detected.

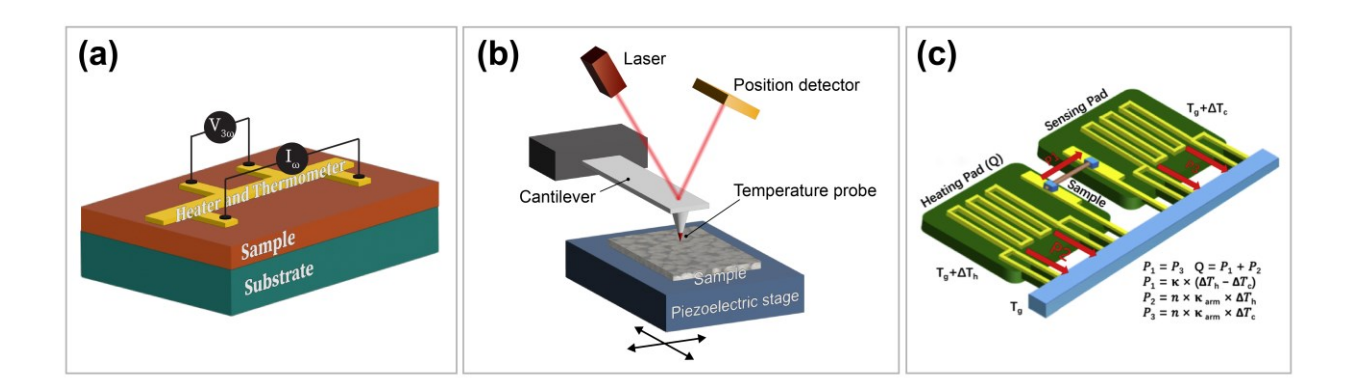


FIG. 3. Schematics of electrothermal-based thermal transport measurement techniques. (a) 3ω method adopting four-point probe configuration. (b) Scanning thermal microscopy (SThM) method. (c) Suspended-pad method. Reproduced with permission from Joule 2, 442-463 (2018). Copyright 2018 Elsevier. ¹⁶¹

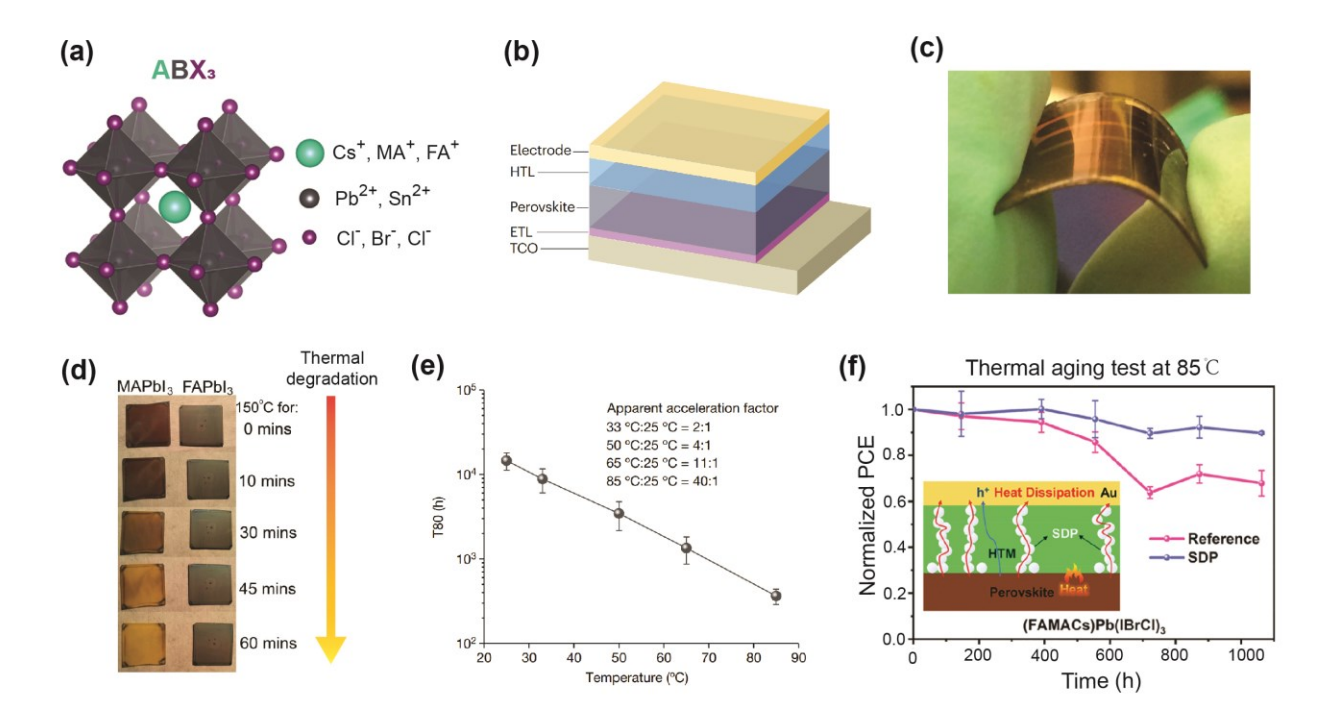


FIG. 4. (a) Schematic diagram of the structure of 3D MHPs. (b) Schematic drawing of a regular PSC structure (*n-i-p* type). Reproduced with permission from Nat. Rev. Mater. 9, 399-419 (2024). Copyright 2024 Springer Nature.¹⁷² (c) Photograph of a flexible PSC on PET/ITO substrate. Reproduced with permission from ACS Nano 8, 1674-1680 (2014). Copyright 2014 American Chemical Society.¹⁸⁷ (d) Thermal degradation of MAPbI₃ and FAPbI₃, when bare spin-coated films of each MHP are heated in air at 150 °C for durations indicated. Reproduced with permission from Energy Environ. Sci. 7, 982-988 (2014). Copyright 2014 RSC Publishing.¹⁹¹ (e) T80 (time for a solar cell to degrade to 80% of its maximum efficiency) as a function of temperature. Reproduced with permission from Nature 623, 313-318 (2023). Copyright 2023 Springer Nature.²⁰¹ (f) Long-term thermal stability of unencapsulated PSCs based on mixed MHP absorbers with/without silicon dioxide particles (SDP). Reproduced with permission from ACS Energy Lett. 6, 3029-3036 (2021). Copyright 2021 American Chemical Society.²⁰⁴

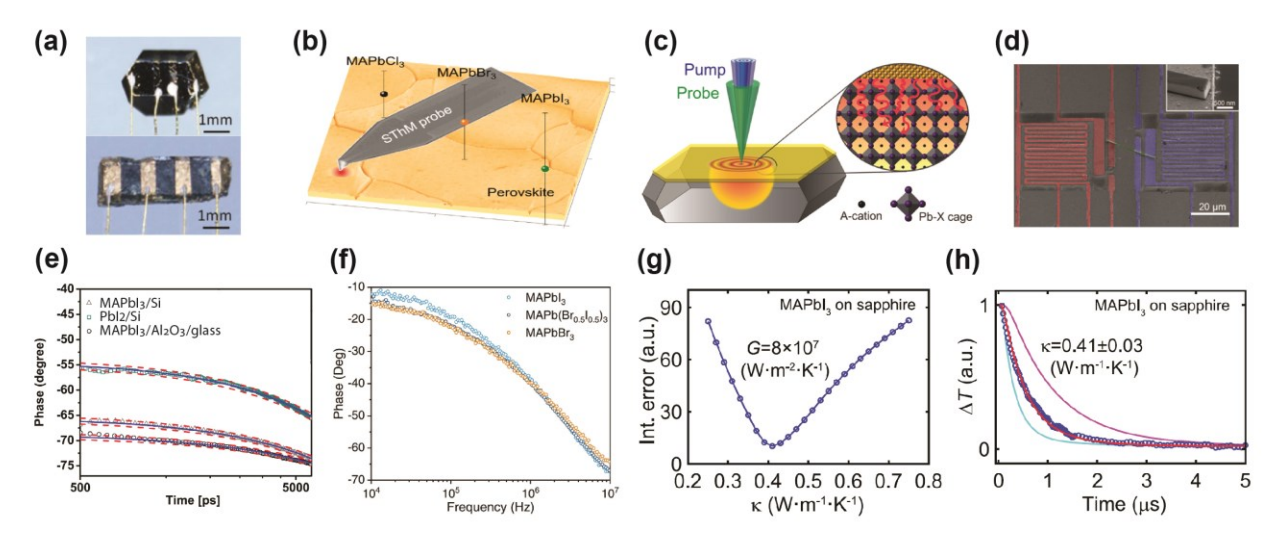


FIG. 5. (a) Photographs of a single MAPbI₃ single crystal (top) and polycrystal (bottom) used in electrical and thermal transport measurements with the four-point probe method. Reproduced with permission from J. Phys. Chem. Lett. 5, 2488-2492 (2014). Copyright 2014 American Chemical Society.³⁷ (b-d) Schematics of (b) SThM. Reproduced with permission from J. Phys. Chem. C 121, 28306-28311 (2017). Copyright 2017 American Chemical Society. (c) TDTR/FDTR. Reproduced with permission from Nano Lett. 17, 5734-5739 (2017). Copyright 2017 American Chemical Society. (d) Suspended-pad methods for MAPbI3 thermal conductivity measurements. Reproduced with permission from Nano Lett. 18, 2772-2779 (2018). Copyright 2018 American Chemical Society. ^{34,210,220} (e) The TDTR phase of signals measured on different substrates at 294 K with 3 MHz modulation. Solid lines are fitting curves using a pulse accumulation heat conduction model. Red-dash lines represent the 90% confidence interval of the film thermal conductivity. Reproduced with permission from J. Phys. Chem. C 120, 6394-6401 (2016). Copyright 2016 American Chemical Society.²¹⁴ (f) Representative plots of phase of signals as a function of pump-beam modulation frequency for three samples from FDTR experiments. Reproduced with permission from Adv. Sci. 11, 2401194 (2024). Copyright 2024 Authors, licensed under a Creative Commons Attribution (CC-BY) license. 215 (g) Integrated error as a function of κ under a fixed G (interfacial thermal conductance between the sample and substrate) value of 8×10⁷ W·m⁻²·K⁻¹.¹¹² (h) Temperature decay profiles from finite-element computation (red curve) and experiments (blue open circles) using the optimal κ value of 0.41 W·m⁻¹·K⁻¹ (G value is taken as 8×10⁷ W·m⁻²·K⁻¹). The magenta curve shows the computation result using the smallest value for κ (0.24 W·m⁻¹·K⁻¹) in the parametric sweeps, and the cyan curve shows the computation result using the largest values for κ (0.69 W·m⁻¹·K⁻¹). Reproduced from Rev. Sci. Instrum. 93, 053003 (2022), with the permission of AIP Publishing. 112

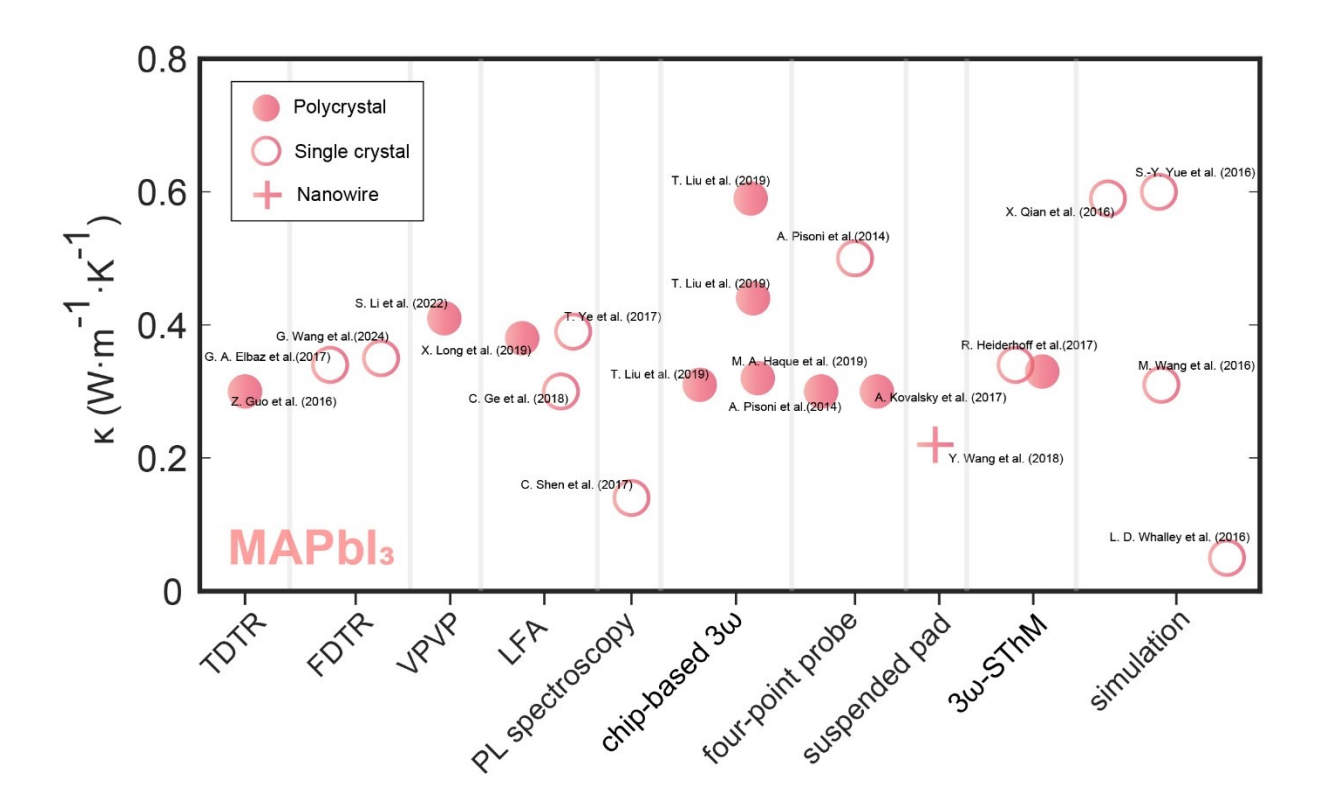


FIG. 6. Summary of reported thermal conductivities of MAPbI₃ measured with different methods (simulations include both MD and DFT). Detailed values and references of the data points are summarized in **Table 1**.

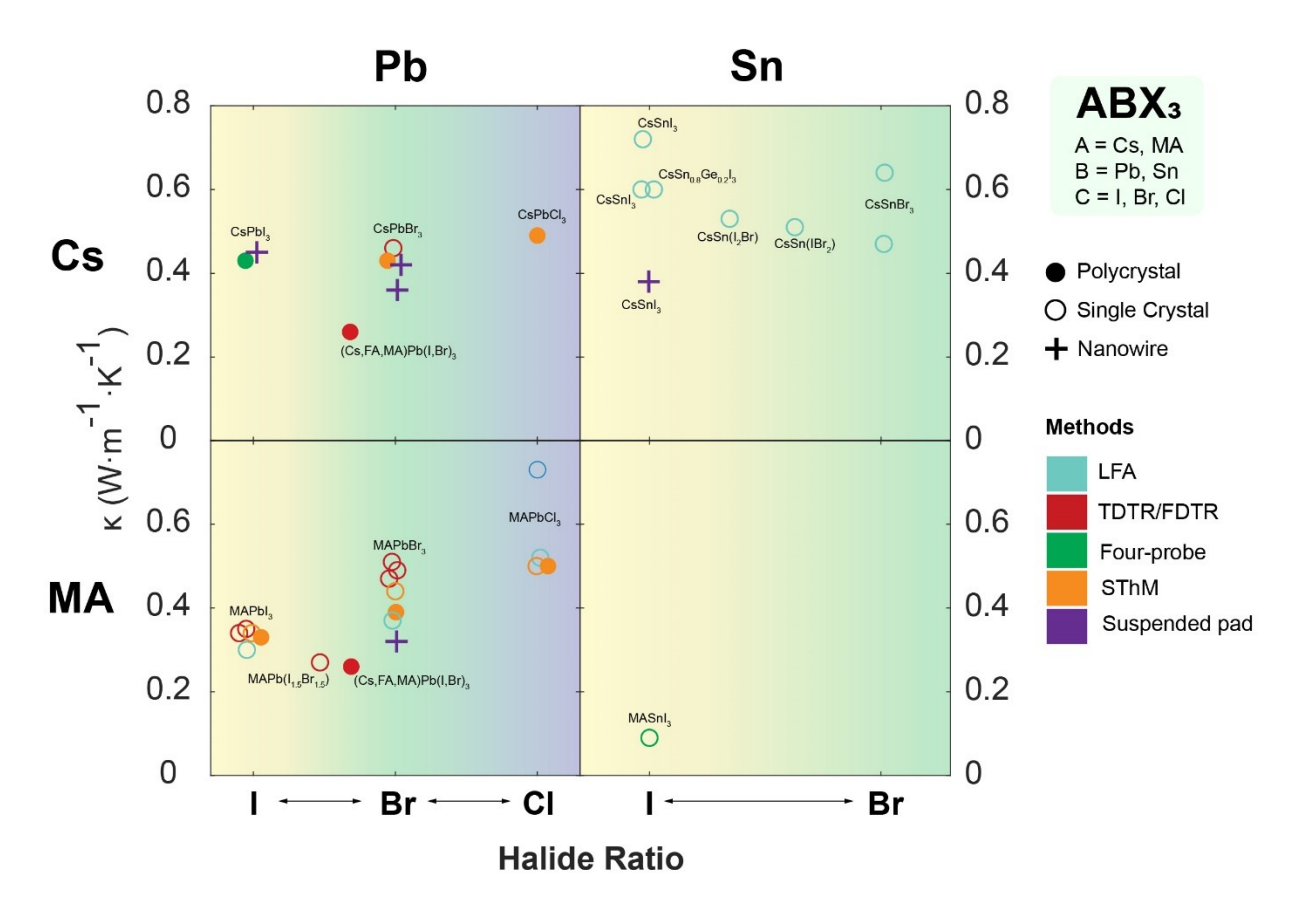


FIG. 7. Summary of thermal conductivities of 3D MHPs (ABX₃) with varying halide elements (X) and mixing ratios. Values and references of the data points are summarized in **Table 2**.

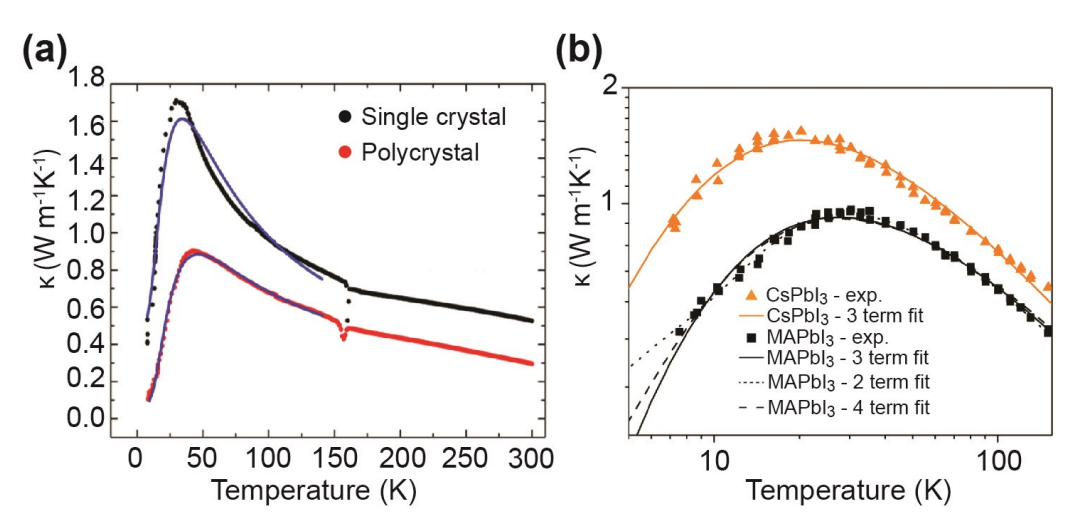


FIG. 8. (a) Temperature dependence of thermal conductivities of single crystalline (black) and polycrystalline (red) MAPbI₃ samples. Blue lines are obtained from the theoretical model. Reproduced with permission from J. Phys. Chem. Lett. 5, 2488-2492 (2014). Copyright 2014 American Chemical Society.³⁷ (b) Thermal conductivities of MAPbI₃ and CsPbI₃ plotted on a logarithmic scale. Solid lines represent model fitting considering three phonon scattering mechanisms (grain boundaries, point defects and Umklapp scattering). Dotted lines represent modified model containing two scattering terms (both Umklapp and resonant scattering). Dashed lines represent the model taking into account all four relevant phonon scattering mechanisms. Reproduced with permission from J. Phys. Chem. C 121, 3228-3233 (2017). Copyright 2017 American Chemical Society.²⁰⁹

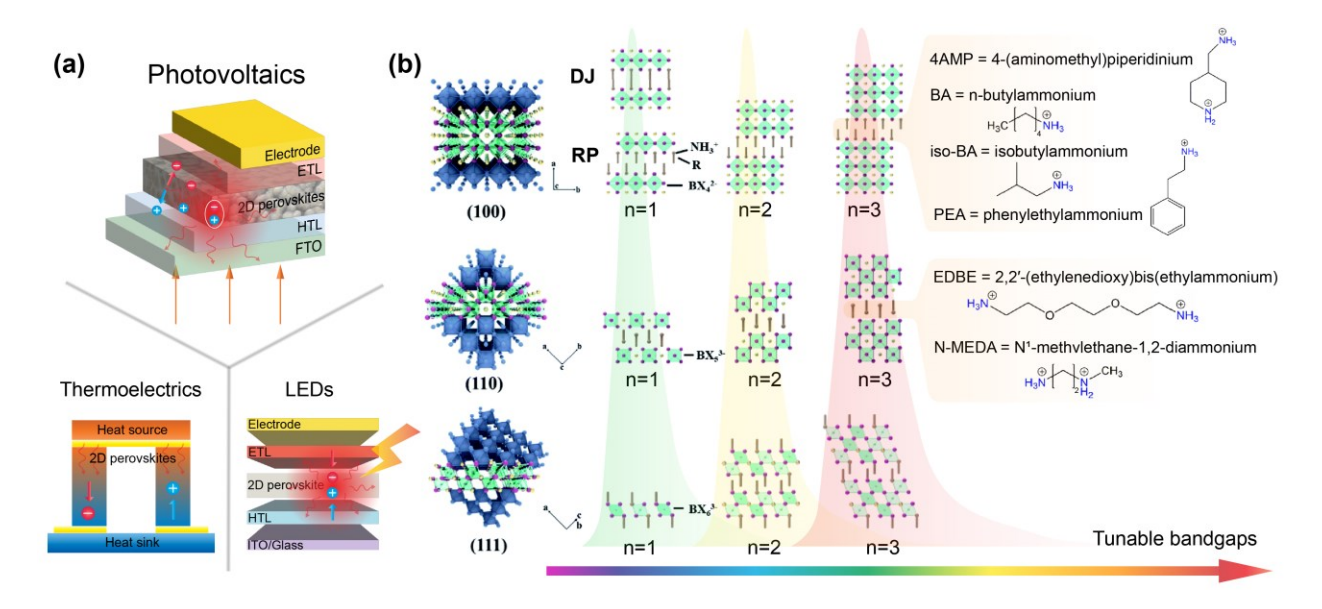


FIG. 9. (a) Upper panel: Schematic of representative PV application of 2D MHPs with free carriers and heat generated simultaneously following the absorption of lights. ETL: electron transport layer. HTL: hole transport layer. FTO: fluorine-doped tin oxide. Lower panel: Thermoelectrics adopting 2D MHPs with efficient charge transfer and suppressed thermal transport between the heat source and sink (left). LEDs enabled by the strong exitonic effect in 2D MHPs and heat accumulation from the carrier recombination (right). (b) Crystal structures of (100)-, (110)-, and (111)-oriented 2D MHPs with tunable bandgaps achieved by varying the thickness of the inorganic layers (*e.g.* from n = 1 to n = 3). Reproduced with permission from Sustainable Energy Fuels **5**, 3950-3978 (2021). Copyright 2021 Royal Society of Chemistry.²⁸⁰ Some typical organic spacers that provide feasible approaches to modify the materials such as the structure orientation are also presented. Reproduced with permission from J. Am. Chem. Soc. **141**, 1171-1190 (2019). Copyright 2019 American Chemical Society.²⁹⁰

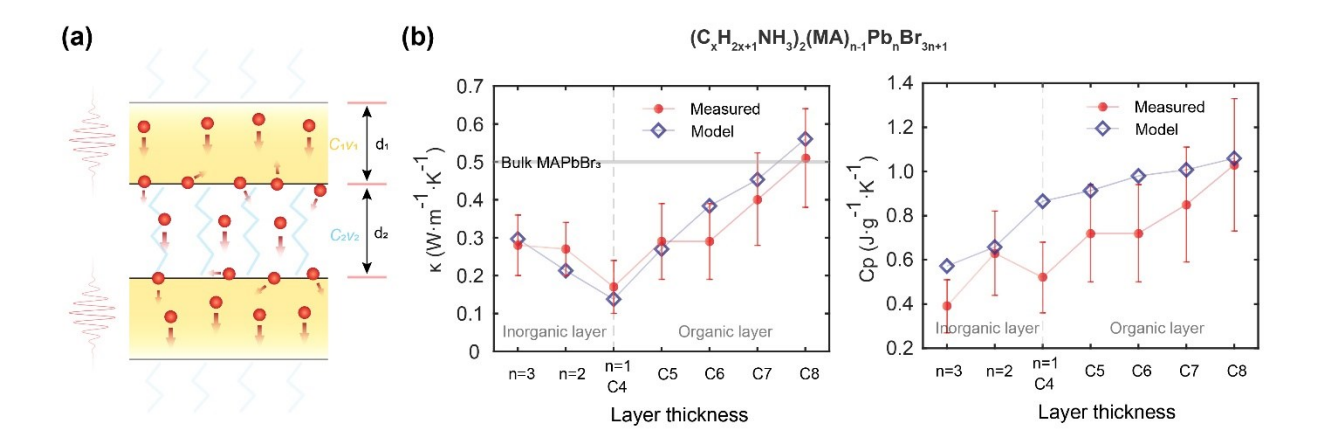


FIG. 10. (a) Incoherent thermal transport in the cross-plane direction of 2D hybrid MHPs where short-wavelength particle-like phonons travel ballistically through the interior of individual layer and scatter diffusively at the organic-inorganic interfaces. The cross-plane κ is solely determined by the specific heat (C), phonon group velocity (v) and layer thickness (d) of the organic and inorganic layers. (b) Thermal conductivity (left panel) and heat capacity (right panel) trend of $(C_xH_{2x+1}NH_3)_2(MA)_{n-1}Pb_nI_{3n+1}$ with increasing thickness of inorganic (n value) and organic (n value) layers. Reproduced with permission from arXiv:2303.17397. Copyright 2024 Authors, licensed under a Creative Commons Attribution (CC-BY) license.²⁵⁸

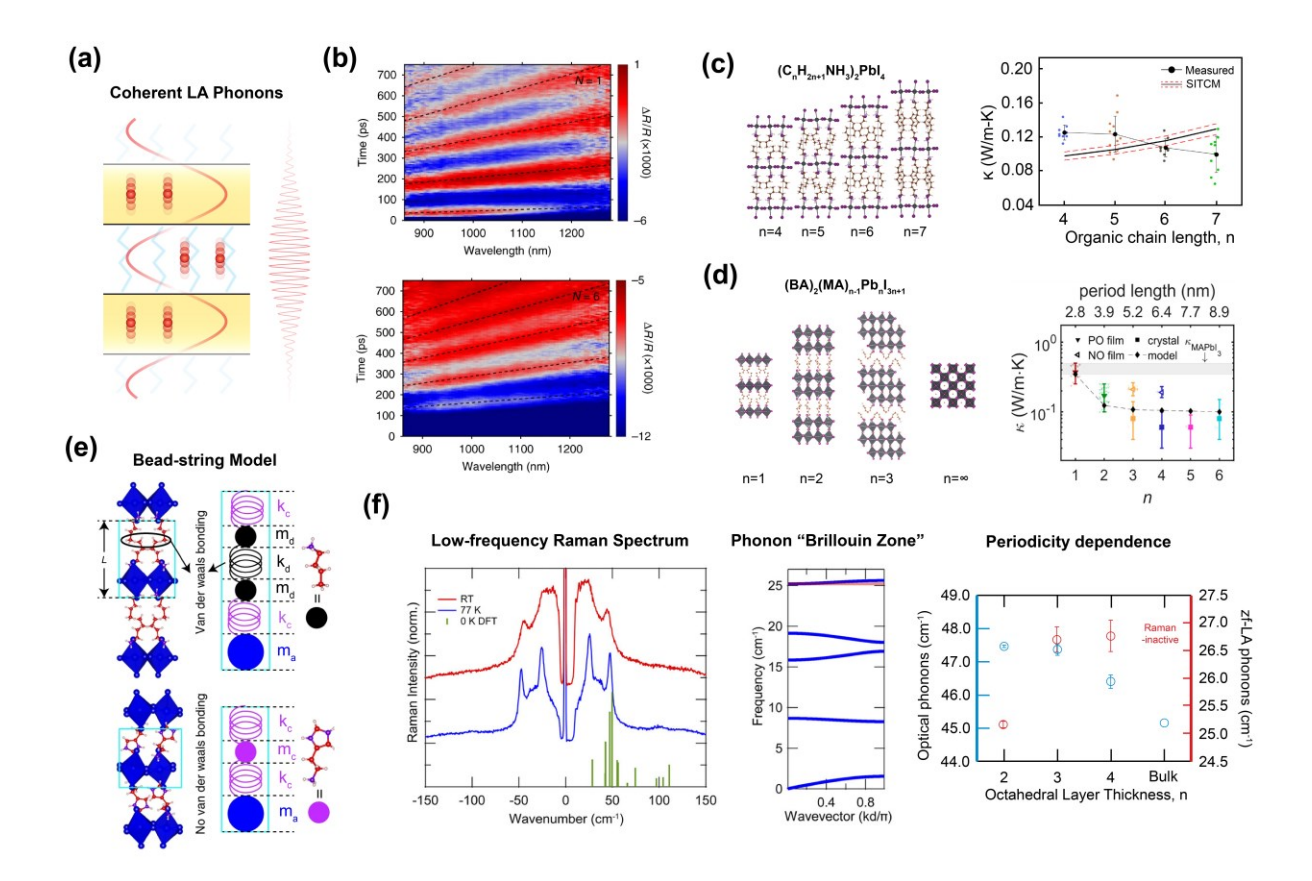


FIG. 11. (a) Coherent thermal transport in the cross-plane direction of 2D hybrid MHPs where coherent LA phonons with MFPs spanning several layers behave wave-like and travel coherently across layers with minimal or no interface scattering. (b) Transient reflection ($\Delta R/R$) spectral maps for $(BA)_2(MA)_{N-1}Pb_NI_{3N+1}$ with N=1 (upper panel) and N=6 (lower panel) showing oscillations that indicate the presence of longitudinal coherent acoustic phonons. Reproduced with permission from Nat. Commun. 9, 2019 (2018). Copyright 2018 Authors, licensed under a Creative Commons Attribution (CC-BY) license. ²⁶¹ (c) Decreasing thermal conductivity of RP-phase 2D MHPs with increasing thickness of organic layers, i.e. number of carbons in the alkylammonium chain length from n = 4 to 7, measured with TDTR (indicated by the scatters), and an opposite trend predicted by the stacked interface model (solid and dashed lines). Reproduced with permission from ACS Appl. Mater. Interfaces 12, 53705-53711 (2020). Copyright 2020 American Chemical Society.²⁵⁶ (d) Decreasing thermal conductivity of RP-phase 2D MHPs with increasing thickness of inorganic layers measured with FDTR on single crystals and films, and calculated with a harmonic beadstring model. Reproduced with permission from ACS Nano 15, 4165-4172 (2021). Copyright 2021 American Chemical Society.²⁶⁰ (e) A harmonic bead-string model for the cross-plane thermal transport of 2D hybrid MHPs with monovalent spacer cation (upper panel) and divalent spacer cation (lower panel). Reproduced with permission from Nat. Commun. 9, 2019 (2018). Copyright 2018 Authors, licensed under a Creative Commons Attribution (CC-BY) license.²⁶¹ (f) Left panel: low-frequency Raman spectra of n = 2 (BA)₂MAPb₂I₇, measured at room temperature (red) and 77 K (blue), and calculated at 0 K with DFT (green). The sharp peaks at 47.5 cm⁻¹ and 25.2 cm⁻¹ correspond to the inorganic cage distortion and zone-fold longitudinal acoustic (zf-LA) phonon mode, respectively. Middle panel: Calculated phonon "Brillouin zone" dispersion (blue) and

experimentally measured zf-LA phonon mode frequency (red). Right panel: Periodicity dependence of the optical (blue) and zf-LA (red) phonon energy, measured with increasing inorganic layer thickness from n = 2 to 4 and for bulk MAPbI₃. Reproduced from J. Chem. Phys. **153**, 044710 (2020), with the permission of AIP Publishing.³⁰³

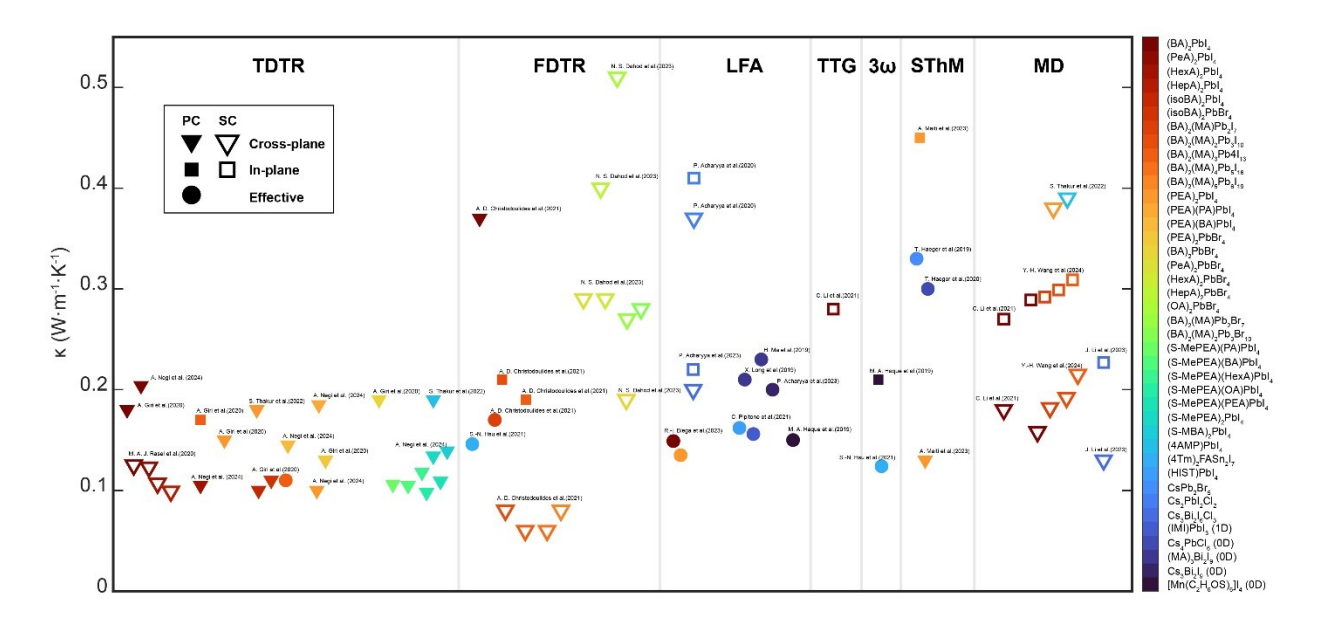


FIG. 12. Summary of anisotropic thermal conductivities of quasi-2D and other lower-dimensional MHPs measured (and calculated) with different techniques. The color of the marker indicates the specific material. The triangular and square markers represent the cross-plane and in-plane thermal conductivities, respectively. The effective (circular marker) values come from measurements on randomly oriented polycrystals. The hollowed markers strand for values of single crystals, while the filled markers are for polycrystalline samples, including films, powders, and powder-pressed pellets. A summary of thermal conductivity values, specific heat, and references can be found in Table 3.

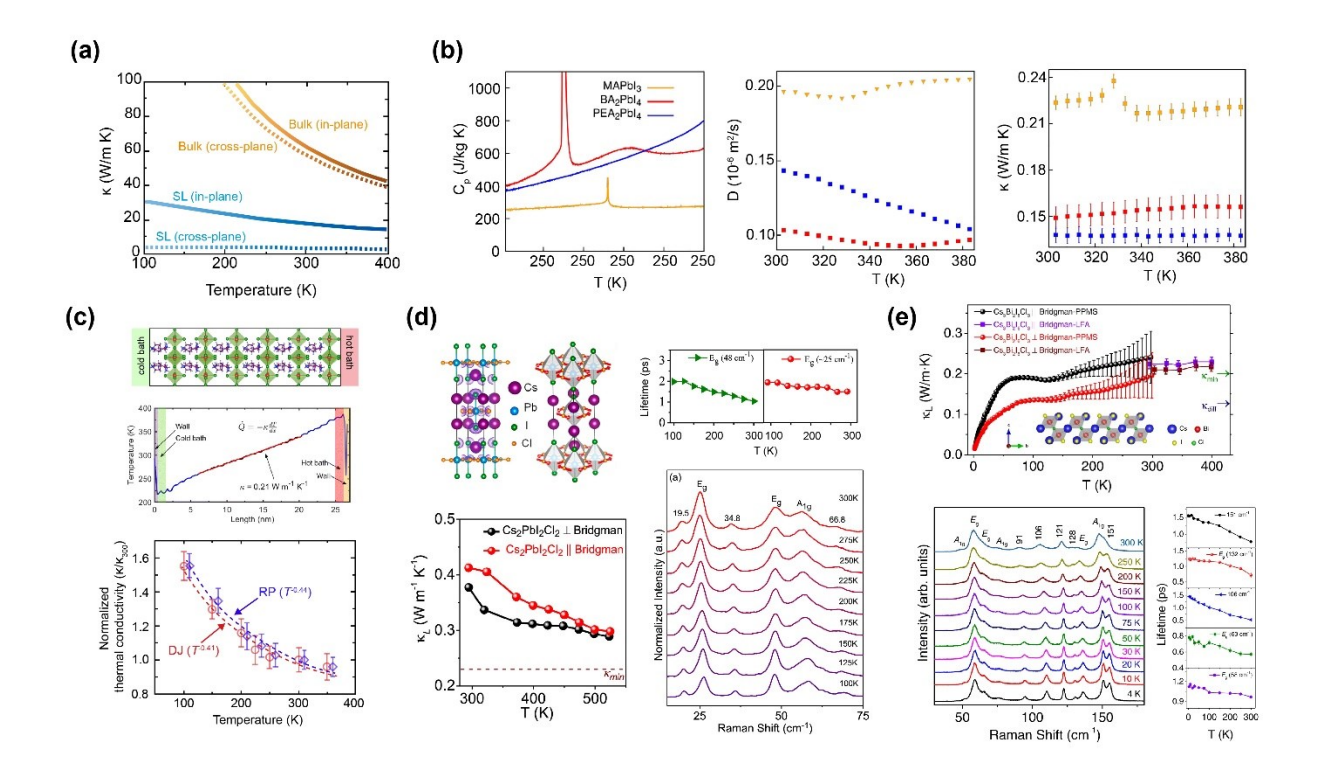


FIG. 13. (a) Temperature-dependent thermal conductivity of a typical superlattice (SL), GaAs/AlAs, calculated with the partially coherent model, and effective bulk values based on Fourier's law as $\kappa_{\text{bulk,in-plane}} = (\kappa_1 + \kappa_2)/2$, and $\kappa_{\text{bulk,cross-plane}} = 2\kappa_1 \kappa_1/(\kappa_1 + \kappa_2)$. Reproduced with permission from Phys. Rev. B 67, 195311 (2003). Copyright 2003 American Physical Society.²⁶⁵ (b) Measured heat capacity, thermal diffusivity, and determined thermal conductivity of 3D MAPbI₃ (yellow), 2D (BA)₂PbI₄ (red) and (PEA)₂PbI₄ (blue) from 300 to 385 K. Reproduced with permission from J. Phys. Chem. C 127, 9183-9195 (2023). Copyright 2023 American Chemical Society. 43 (c) Upper panel: Schematic of MD simulation domain for DJ-phase 2D MHPs. Middle panel: thermal conductivity calculation from the temperature gradient across the domain when subjected a cross-plane heat flux invoking Fourier's law. Lower panel: Predicted temperature-dependent thermal conductivities of DJ-phase (4AMP)PbI₄ and RP-phase (PEA)₂PbI₄ from 100 to 350 K (normalized by the thermal conductivity of DJ phase at 300 K). Temperature dependence $(T^{-\alpha})$ of $\alpha = 0.41$ and 0.44 are extracted from the fitted curve for DJ and RP phase, respectively. Reproduced with permission from Mater. Horiz. 9, 3087-3094 (2022). Copyright 2022 Royal Society of Chemistry.²⁵⁷ (d) Crystal structure (upper left), temperature-dependent lattice thermal conductivity along the in-plane (||) and cross-plane direction (\pm) (lower left), and temperature-dependent Raman spectra (lower right) of all-inorganic 2D RP-phase Cs₂PbI₂Cl₂ showing decreasing lifetime of the two E_g phonon modes with increasing temperature (upper right). Reproduced with permission from J. Am. Chem. Soc. 140, 11085-11090 (2018). Copyright 2018 American Chemical Society.333 (e) Upper panel: Temperature-dependent lattice thermal conductivity of (111)-oriented all-inorganic 2D MHP, Cs₃Bi₂I₆Cl₃, along in-plane (||) and cross-

plane (\perp) direction measured with DynaCool physical property measurement system (PPMS) in 2 ~ 300 K and with LFA in $300 \sim 400$ K. The inset shows one slice of the layered crystal structure. Lower panel: Temperature-dependent Raman spectra and temperature variation of phonon lifetime for the modes at 151 cm⁻¹ (black), 132 cm⁻¹ (red), 106 cm⁻¹ (blue), 63 cm⁻¹ (green), and 58 cm⁻¹ (purple). Reproduced with permission from Nat. Commun. 13, 5053 (2022). Copyright 2022 Authors, licensed under a Creative Commons Attribution (CC-BY) license.³²⁷

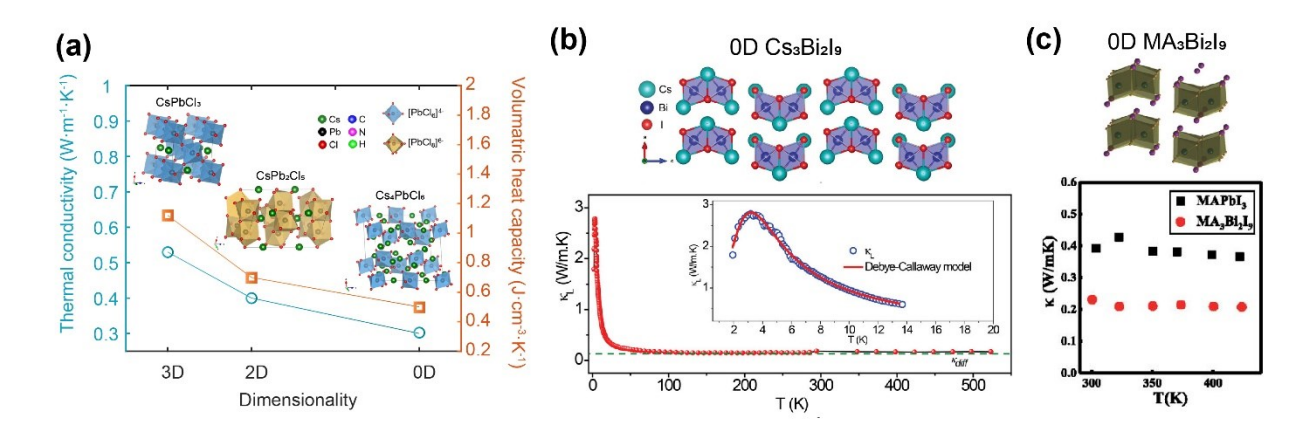


FIG. 14. (a) Crystal structures⁴⁴⁷ and dimensionality-dependent thermal conductivities³⁶ of 3D CsPbCl₃, 2D CsPb₂Cl₅, and 0D Cs₄PbCl₆. Reproduced with permission from ACS Mater. Lett. 4, 1255-1263 (2022). Copyright 2022 American Chemical Society. Reproduced with permission from J. Mater. Chem. C 8, 14289-14311 (2020). Copyright 2020 Royal Society of Chemistry. (b) Crystal structure and thermal conductivity of 0D Cs₃Bi₂I₉ as a function of temperature in 2 ~ 532 K measured by LFA. Reproduced with permission from Adv. Funct. Mater. 33, 2304607 (2023). Copyright 2023 John Wiley and Sons.³⁴⁸ (c) Crystal structure³⁴² and thermal conductivity of 0D MA₃Bi₂I₉ as a function of temperature from 300 to 450 K measured by LFA.²¹⁸ Reproduced with permission from Adv. Energy Mater. 8, 1703620 (2018). Copyright 2018 John Wiley and Sons. Reproduced from Appl. Phys. Lett. 115, 072104 (2019), with the permission of AIP Publishing.

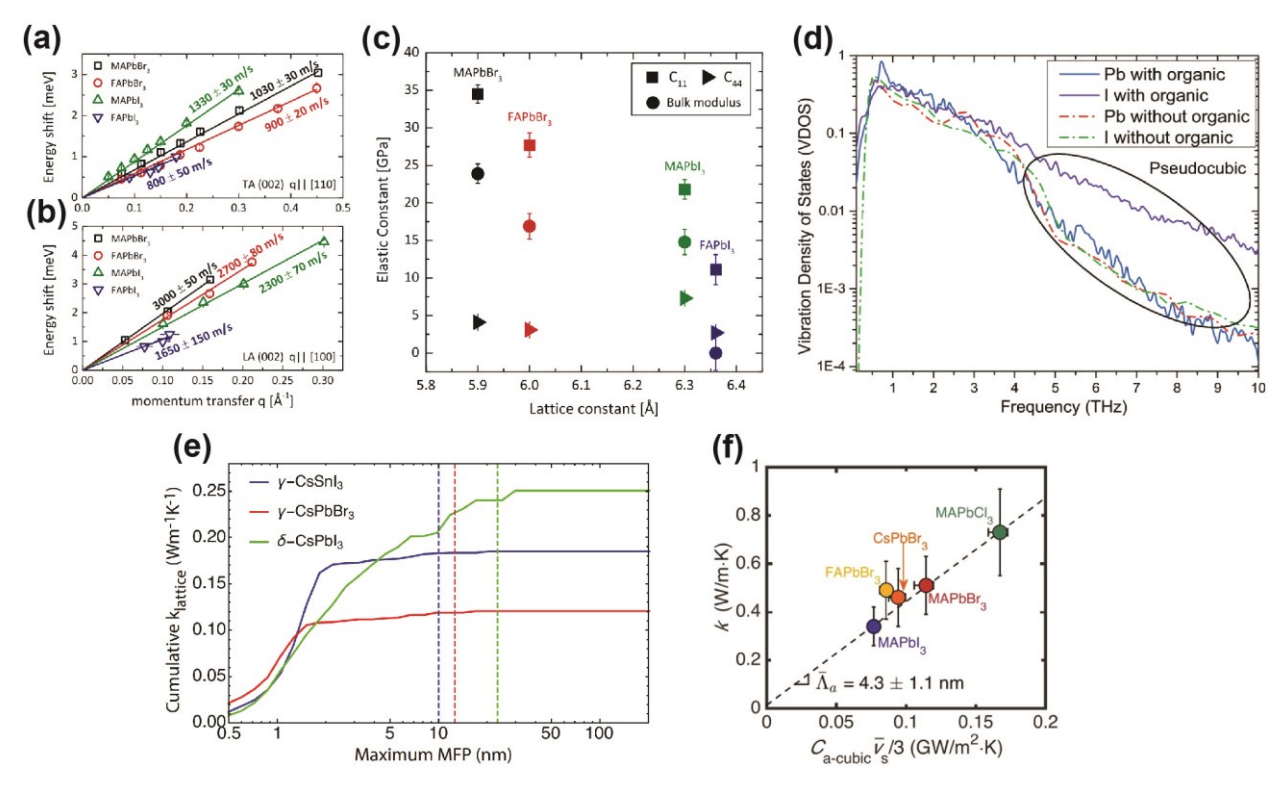


FIG. 15. (a) Transverse and (b) Longitudinal acoustic phonon dispersion curves of MAPbBr₃ (black), FAPbBr₃ (red), MAPbI₃ (green), and FAPbI₃ (blue) at around the (002) Bragg reflection, measured by INS.³⁵¹ (c) Elastic constants C_{11} and C_{44} as well as the bulk modulus K as functions of the cubic lattice constant of each compound. Reproduced with permission from Phys. Rev. Lett. 121, 085502 (2018). Copyright 2018 American Physical Society.³⁵¹ (d) Comparison of the partial vibrational density of states of Pb and I ions in the inorganic cages with and without organic MA⁺ clusters. The solid lines are the results of normal pseudocubic structures (with MA⁺) and the dashed-dotted lines represent the empty pseudocubic inorganic cages (without MA⁺). Reproduced with permission from Phys. Rev. B. 94, 115427 (2016). Copyright 2016 American Physical Society. ²³³ (e) Cumulative $\kappa_{lattice}$ with respect to phonon MFPsat room temperature computed by a combination of BTE and DFT. Reproduced with permission from Proc. Natl. Acad. Sci. 114, 8693-8697 (2017). Copyright 2017 National Academy of Sciences. 235 (f) κ as a function of $C_{\text{a-cubic}}\overline{v_s}/3$, where $C_{\text{a-cubic}}$ is the volumetric heat capacity of acoustic phonons based on a cubic unit cell. The dashed line is a linear fit for MAPbX₃. CsPbBr₃ is on the trendline, while FAPbBr₃ is above the trendline. The slope of the fit gives the average acoustic phonon mean free path $\bar{\Lambda}_a$ = 4.3 ± 1.1 nm. Reproduced with permission from Nano Lett. 17, 5734-5739 (2017). Copyright 2017 American Chemical Society.³⁴

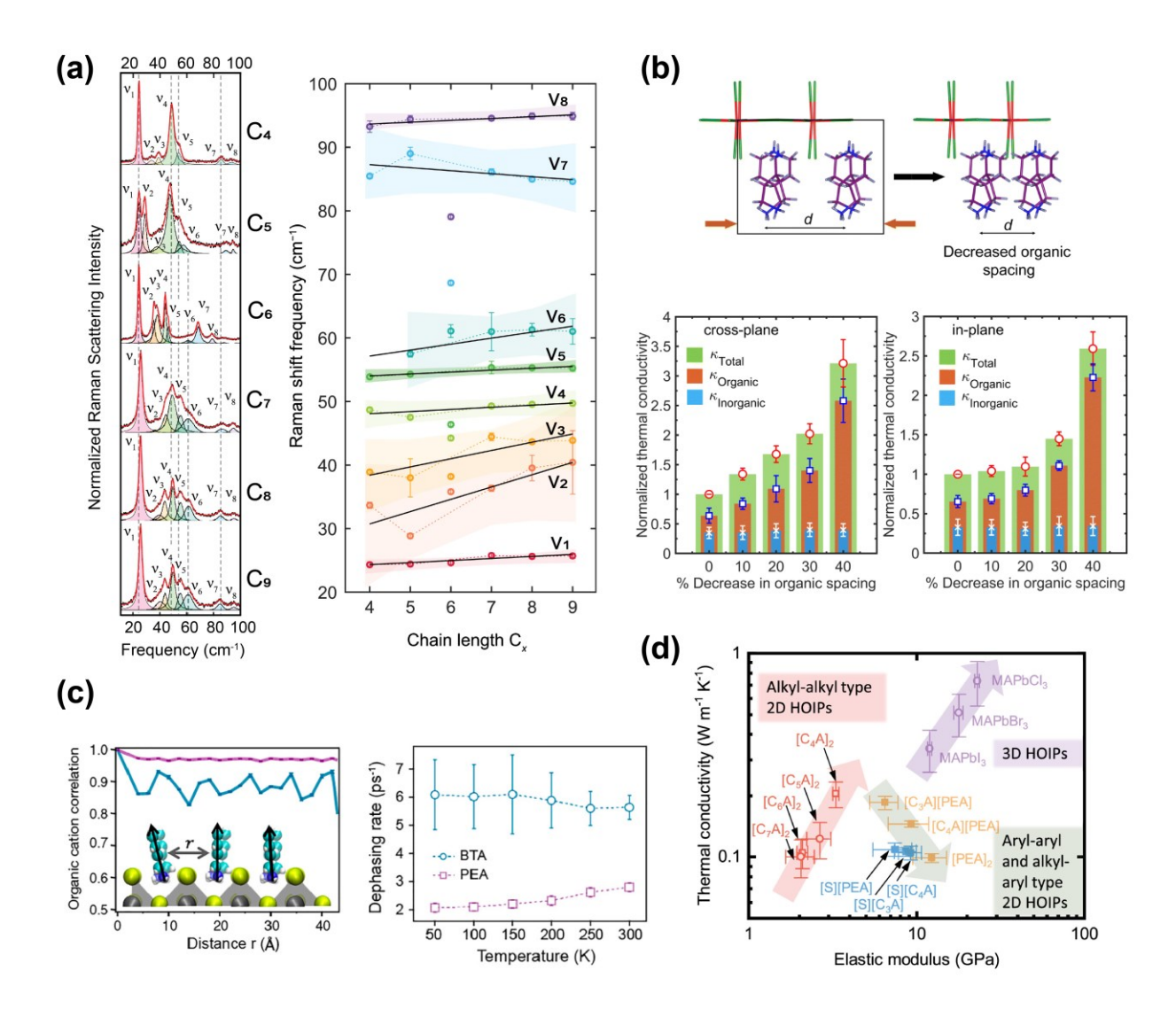


FIG. 16. (a) Left panel: Nonresonant continuous wave Raman spectra of 2D MHPs with varying lengths of alkylammonium (number of carbons from 4 to 9) at 78 K. Right panel: Raman shifts of the modes as a function of chain lengths. Reproduced with permission from J. Phys. Chem. C 123, 27904-27916 (2019). Copyright 2019 American Chemical Society.²⁹⁹ (b) Enhanced thermal conductivities in both cross-plane and in-plane directions with decreasing lateral spacing between the organic spacers, calculated with MD simulation. Reproduced with permission from Mater. Horiz. 9, 3087-3094 (2022). Copyright 2022 Royal Society of Chemistry.²⁵⁷ (c) MD-simulated spatial correlations between the nitrogen-carbon dipole in the organic spacers as a function of the lateral distance between the dipoles (left panel), and the dephasing rate of the lowest optical mode (right panel) in (BA)₂PbBr₄ (blue) and (PEA)₂PbBr₄ (purple). Reproduced with permission from Proc. Natl. Acad. Sci. 118, e2104425118 (2021). Copyright 2021 National Academy of Sciences.³⁵⁴ (d) Correlations between thermal conductivities and elastic moduli of various 2D MHPs. Different interactions are present in 2D MHPs with different spacers incorporated. [C_nA]

represents $(C_nH_{2n+1}NH_3)^+$, and [S] represents (S-MePEA) $^+$. Reproduced with permission from ACS Nano **18**, 14218-14230 (2024). Copyright 2024 American Chemical Society. ²⁵⁹

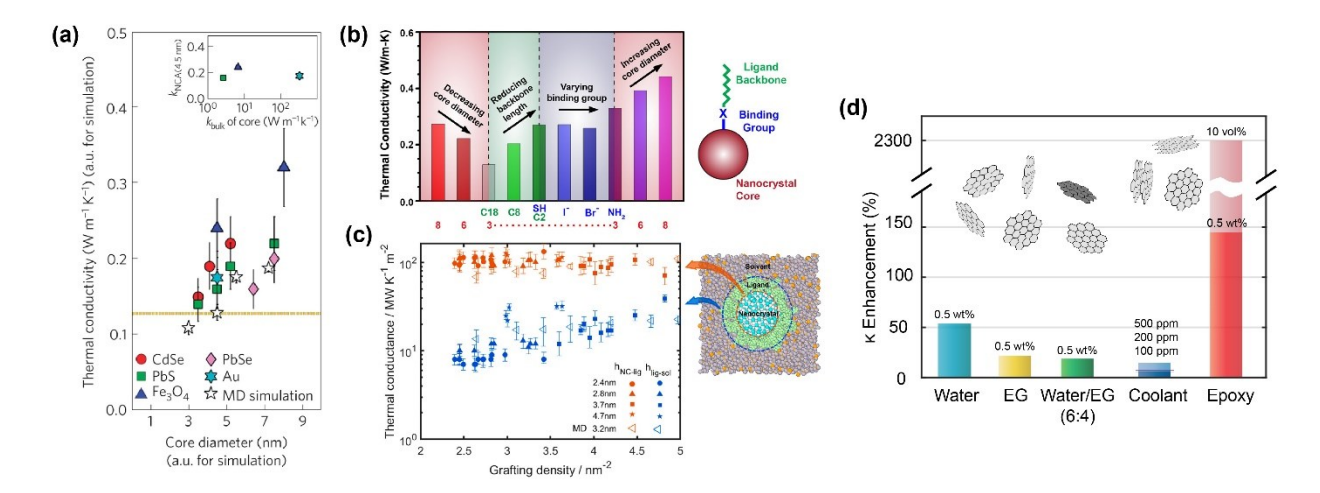


FIG. 17. (a) Size-dependent thermal conductivities of nanocrystalline CdSe, PbSe, PbS, Au, and Fe₃O₄ films measured with FDTR, together with MD simulated values. The inset shows that the nanocrystal κ is insensitive to the bulk κ of the core materials. The orange-dash line represents the κ of Pb oleate at 300 K. Reproduced with permission from Nat. Mater. 12, 410-415 (2013). Copyright 2013 Springer Nature.³⁹⁰ (b) Thermal conductivities of PbS nanocrystals modified by core diameters (red and purple), ligand lengths (green), and ligand binding strengths (blue). Reproduced with permission from ACS Nano 9, 12079-12087 (2015). Copyright 2015 American Chemical Society.³⁸⁹ (c) Interfacial thermal conductance of the nanocrystal-ligand (orange) and ligand-solvent (blue) interfaces with varying grafting densities and crystal sizes. Reproduced with permission from Nano Lett. 23, 3687-3693 (2023). Copyright 2023 American Chemical Society. 397 (d) Thermal conductivity enhancement of the base material when a small amount of graphene (and/or multilayer-graphene) nanoplatelets are added into distilled water, ethylene glycol (EG), a mixture of water and EG (6:4), car coolant, and epoxy. Increased particle concentration (100 ppm, 200 ppm, and 500 ppm) results in higher enhancement. The light red bar shows the epoxy incorporated with a mixture of mono- and multi-layer graphene. Data are taken from references. 418-422

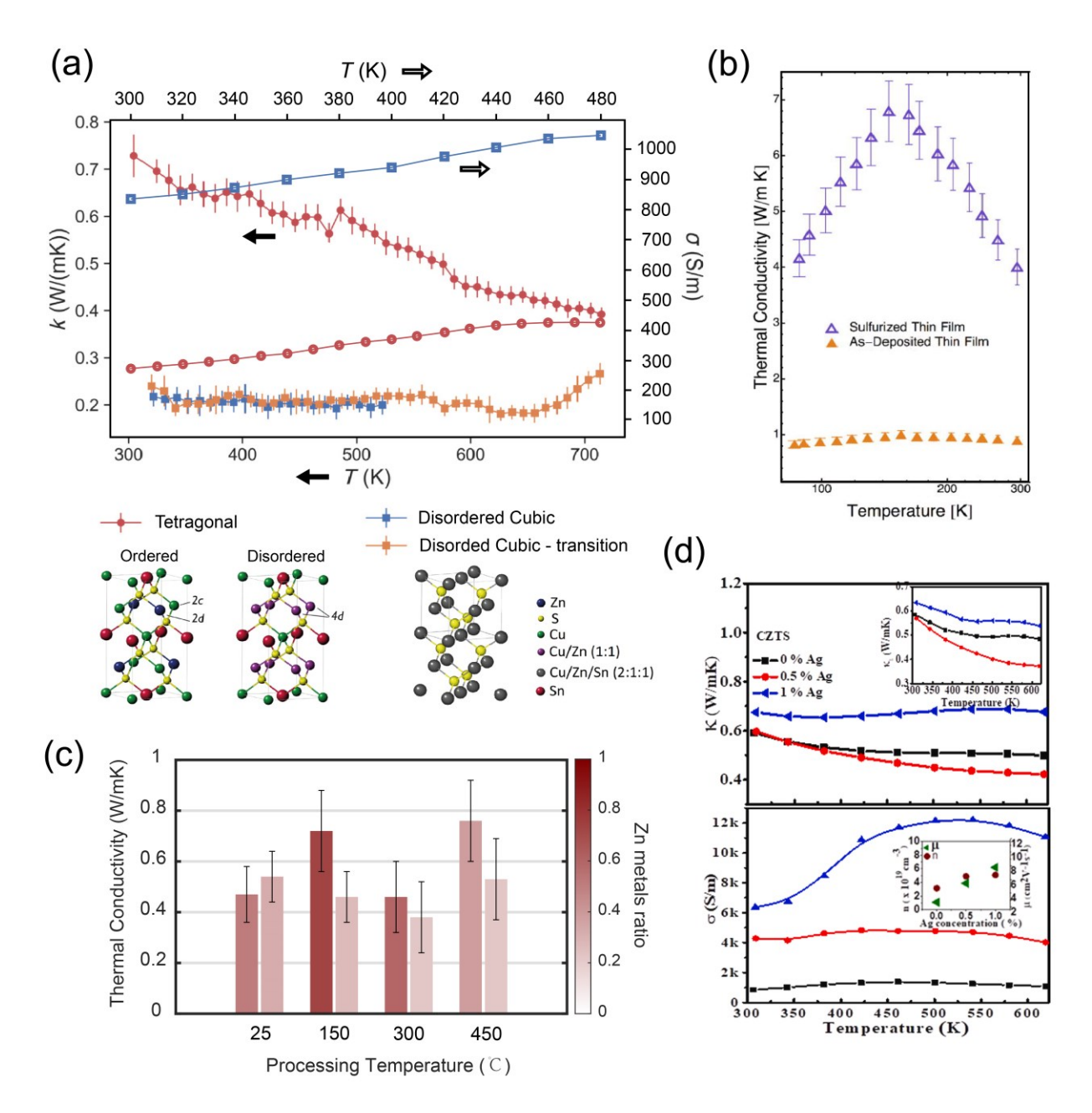


FIG. 18. (a) Thermal conductivities (filled markers) and electrical conductivities (empty markers) of CZTS in tetragonal and cubic phases as a function of temperature measured with LFA. Reproduced with permission from Phys. Rev. Applied 14, 064073 (2020). Copyright 2020 American Physical Society. (b) Thermal conductivities of the pulsed-laser-deposited pristine (orange) and sulfurized (purple) CZTS thin films as a function of temperature measured with 3ω method. Reproduced from J. Appl. Phys. 119, 095108 (2016), with the permission of AIP Publishing. (c) Flexible tunning of thermal conductivities of CZTS thin film by adjusting the Zn metals ratio and annealing temperatures after film growth measured with TDTR. Reproduced with permission from Chem. Mater. 31, 8402-8412 (2019). Copyright 2019 American Chemical Society. (d) Thermal conductivities (upper panel) and electrical conductivities (lower panel) of

CZTS incorporated with varying amounts of Ag nanoparticles measured with LFA. Reproduced with permission from Ceram. Int. **45**, 2060-2068 (2019). Copyright 2019 Elsevier. ⁴³¹

Table 1 Summary of thermal conductivities of MAPbI₃.

Material form	κ (W·m ⁻¹ ·K ⁻¹)	method	ref.
SC	0.5	four-point probe	37
PC	0.3	four-point probe	37
PC	0.3	four-point probe	209
SC	0.34 ± 0.12	SThM	210
film	0.33 ± 0.12	SThM	210
film (on Si)	11.2 ± 0.8	TDTR	213
film (on Sapphire)	0.41 ± 0.03	VPVP	112
film (on quartz)	0.3 ± 0.02	VPVP	112
film (on CaF ₂)	0.51 ± 0.02	VPVP	112
film (in mesostructured Al ₂ O ₃)	0.2	TDTR	214
film (on Si)	0.3	TDTR	214
SC	0.34 ± 0.08	FDTR	34
SC	0.35 ± 0.11	FDTR	215
SC	0.14 ± 0.02	PL spectroscopy	221
SC	0.3	LFA	217
PC	0.38	LFA	218
SC	0.39	LFA	216
nanowire	0.22	suspended pad	220
film	0.32 ± 0.03	chip-based 3ω	219
film (65 nm)	0.31 ± 0.03	chip-based 3ω	150
film (80 nm)	0.44 ± 0.03	chip-based 3ω	150
Film (100 nm)	0.59 ± 0.04	chip-based 3ω	150
SC	0.59	MD	231
SC	0.6	MD	233
SC	0.31	MD	202

SC	0.05	DFT	234

Table 2 Summary of thermal conductivities of 3D perovskites other than $MAPbI_3$

Materials	form	κ (W·m ⁻¹ ·K ⁻¹)	method	ref.
$MASnI_3$	SC	0.09 ± 0.01	four-point probe	448
MAPbBr ₃	SC	0.44 ± 0.08	SThM	210
MAPbBr ₃	film	0.39 ± 0.05	SThM	210
MAPbCl ₃	SC	0.5 ± 0.05	SThM	210
MAPbCl ₃	film	0.5 ± 0.12	SThM	210
CsPbI ₃	PC	0.43	four-point probe	209
CsPbI ₃	nanowire	0.45 ± 0.05	suspended pad	235
CsPbBr ₃	nanowire	0.42 ± 0.04	suspended pad	235
$CsSnI_3$	nanowire	0.38 ± 0.04	suspended pad	235
MAPbBr ₃	SC	0.37	LFA	217
MAPbCl ₃	SC	0.52	LFA	217
MAPbBr ₃	nanowire	0.32	suspended pad	220
CsPbBr ₃	nanowire	0.36	suspended pad	220
CsPbBr ₃	film	0.43 ± 0.03	SThM	219
CsPbCl ₃	film	0.49 ± 0.04	SThM	219
(Cs,FA,MA)Pb(I,Br) ₃	film	0.26 ± 0.03	TDTR	238
$CsSnI_3$	SC	0.72	LFA	239
CsSnBr ₃	SC	0.47	LFA	240
CsSnBr ₃	SC	0.64	LFA	241
CsSnBr ₂ I	SC	0.51	LFA	241
$CsSnBrI_2$	SC	0.53	LFA	241
CsSnI ₃	SC	0.6	LFA	241
$MAPbBr_3$	SC	0.51 ± 0.12	FDTR	34
MAPbCl ₃	SC	0.73 ± 0.18	FDTR	34
CsPbBr ₃	SC	0.46 ± 0.12	FDTR	34

FAPbBr ₃	SC	0.49 ± 0.12	FDTR	34
MAPbBr ₃	SC	0.47 ± 0.09	FDTR	215
$MAPbI_3$	SC	0.35 ± 0.11	FDTR	215
$MAPbBr_{1.5}I_{1.5}$	SC	0.27 ± 0.07	FDTR	215

Table 3 Summary of heat capacity and thermal conductivities of quasi-2D and lower dimensional (1D and 0D) MHPs.

Material	Form	Heat capacity (J/g/K)	κ _⊥ (W/m/K)	κ (W/m/K)	Method s	Ref
(BA) ₂ PbI ₄	Film	0.439	0.18 ± 0.04		TDTR	38
	Film		$0.37 \pm 0.13/0.12$		FDTR	260
	Film		0.204 ± 0.009		TDTR	259
	SC	0.546	0.125 ± 0.009 (330 K)		TDTR	256
	SC	0.48		0.28 ± 0.01	TTG	123
	SC		0.18 ± 0.01	0.27 ± 0.01	MD	123
	powder	0.25 (200 K) 0.30 (300 K) 0.28 (450 K)	0.149 (300 K) ~ 0.1	55 (385 K)	LFA	43
	SC		0.158	0.289	MD	262
*(PeA) ₂ PbI ₄	SC	0.697	0.123 ± 0.021 (330 K)		TDTR	256
*(HexA) ₂ PbI ₄	SC	0.675	0.107 ± 0.011 (330 K)		TDTR	256
	Film		0.105 ± 0.007		TDTR	259
*(HepA) ₂ PbI ₄	SC	0.879	0.099 ± 0.021 (330 K)		TDTR	256
(isoBA) ₂ PbI ₄	Film	0.437	0.10 ± 0.02		TDTR	38
(isoBA) ₂ PbBr ₄	Film	0.576	0.11 ± 0.02		TDTR	38
$(BA)_2(MA)Pb_2I_7$	Film		$0.17 \pm 0.08/0.07$	l	FDTR	260
	SC		0.182	0.292	MD	262

$(BA)_2(MA)_2Pb_3I_{10}$	Film			0.21 ± 0.05/0.04	FDTR	260
	SC		$0.08 \pm 0.06 / 0.04$		FDTR	260
	SC		0.192	0.299	MD	262
$(BA)_2(MA)_3Pb_4I_{13}$	Film			0.17 ± 0.03	TDTR	38
	Film		0.11 ± 0.02	1	TDTR	38
	Film			0.19±0.04/0. 03	FDTR	260
	SC		$0.06 \pm 0.04/0.03$		FDTR	260
	SC		0.215	0.309	MD	262
$(BA)_2(MA)_4Pb_5I_{16}$	SC		0.06 ± 0.03		FDTR	260
$(\mathrm{BA})_2(\mathrm{MA})_5\mathrm{Pb}_6\mathrm{I}_{19}$	SC		$0.08 \pm 0.07/0.04$		FDTR	260
(PEA) ₂ PbI ₄	Film	0.467	0.15 ± 0.03		TDTR	38
	Film		0.18 ± 0.03		TDTR	257
	Film		0.13 ± 0.05	0.45 ± 0.05	SThM	325
	Film		0.100 ± 0.005		TDTR	259
	SC		0.38		MD	257
	Powder	0.38 (200 K) 0.45 (300 K) 0.80 (450 K)	0.135 (300 ~ 380 K	(3)	LFA	43
*(PEA)(PA)PbI ₄	Film		0.185 ± 0.014		TDTR	259
(PEA)(BA)PbI ₄	Film		0.145 ± 0.005		TDTR	259
(PEA) ₂ PbBr ₄	Film	0.535	0.13 ± 0.03		TDTR	38
(BA) ₂ PbBr ₄	Film	0.578	0.19 ± 0.04		TDTR	38
	SC	0.52 ± 0.16	0.19 ± 0.07		FDTR	258
(PeA) ₂ PbBr ₄	SC	0.72 ± 0.22	0.29 ± 0.1		FDTR	258

(HexA) ₂ PbBr ₄	SC	0.72 ± 0.22	0.29 ± 0.1		FDTR	258
()2 -						
(HepA) ₂ PbBr ₄	SC	0.85 ± 0.26	0.40 ± 0.12		FDTR	258
*(OA) ₂ PbBr ₄	SC	1.03 ± 0.3	0.51 ± 0.13		FDTR	258
(BA) ₂ (MA)Pb ₂ Br ₇	SC	0.63 ± 0.19	0.27 ± 0.07		FDTR	258
$(BA)_2(MA)_2Pb_3Br_{10}$	SC	0.39 ± 0.12	0.28 ± 0.08		FDTR	258
*(S-MePEA)(PA)PbI ₄	Film		0.106 ± 0.005		TDTR	259
(S-MePEA)(BA)PbI ₄	Film		0.105 ± 0.008		TDTR	259
(S- MePEA)(HexA)PbI ₄	Film		0.118 ± 0.0075		TDTR	259
(S-MePEA)(OA)PbI ₄	Film		0.098 ± 0.0055		TDTR	259
(S-MePEA)(PEA)PbI ₄	Film		0.109 ± 0.008		TDTR	259
(S-MePEA) ₂ PbI ₄	Film		0.134 ± 0.006		TDTR	259
*(S-MBA) ₂ PbI ₄	Film		0.139 ± 0.0055		TDTR	259
*(4AMP)PbI ₄	Film		0.19 ± 0.03		TDTR	257
	SC		0.39		MD	257
*(4Tm) ₂ FASn ₂ I ₇	Film		0.124		3ω	288
	Film		0.146		TDTR	288
*(HIST)PbI ₄	powder		0.162		LFA	295
CsPb ₂ Br ₅	Film	0.18	0.33 ± 0.02		3ω- SThM	236
$Cs_2PbI_2Cl_2$	SC		0.37 (300K) ~ 0.28 (523 K)	0.41 (300 K) ~ 0.3 (532 K)	LFA	255
$Cs_3Bi_2I_6Cl_3$	SC		0.20	0.22	LFA	327
	SC		0.130	0.227	MD	340

*(PA) ₄ CuInCl ₈	Powder		0.15	0.28	PPMS	51
*(4N4) ₂ CuInCl ₈	Powder			0.27	PPMS	51
*(4N4) ₂ CuRuCl ₈	Powder			0.3	PPMS	51
*(IMI)PbI ₃ (1D)	Powder		0.156		LFA	295
Cs ₄ PbCl ₆ (0D)	Film	0.15 ± 0.08	0.30 ± 0.03		3ω- SThM	237
$(MA)_3Bi_2I_9(0D)$	Powder	0.34	0.21 (300 ~ 450 K)		LFA	218
	Powder	0.34	0.23 ± 0.02		LFA	300
$Cs_3Bi_2I_9(0D)$	Powder		0.20 (30 ~ 523 K)		LFA	348
$[Mn(C_2H_6OS)_6]I_4(0D)$	Powder		0.15 ± 0.01		LFA	350
	Film			0.21 ± 0.01	3ω	350

*

PA = Propyl ammonium

PeA = Pentyl ammonium

HexA = Hexyl ammonium

HepA = Heptyl ammonium

OA = Octyl ammonium

 $S\text{-}MePEA = (S)\text{-}Methyl\text{-}phenyl\text{-}ethyl\text{-}ammonium}$

S-MBA = (S)-Methyl-benzyl-ammonium

 $4Tm = 2-(3^{\prime\prime\prime},4^{\prime}-dimethyl[2,2^{\prime}:5^{\prime\prime},2^{\prime\prime\prime}-quaterthiophen]-5-yl)ethan-1-ammonium$

HIST = Histammonium

4N4 = 1,4-butane diammonium

IMI = Imidazolium

References

Uncategorized References

- G. F. Brown and J. Wu, Laser & Photonics Reviews **3** (4), 394 (2009).
- Martin A Green, (2006).
- ³ A. Kojima, K. Teshima, Y. Shirai, and T. Miyasaka, J Am Chem Soc **131** (17), 6050 (2009).
- Martin A. Green, Anita Ho-Baillie, and Henry J. Snaith, Nature Photonics 8 (7), 506 (2014).
- Huanping Zhou, Qi Chen, Gang Li, Song Luo, Tze-bing Song, Hsin-Sheng Duan, Ziruo Hong, Jingbi You, Yongsheng Liu, and Yang Yang, Science **345** (6196), 542 (2014).
- H. S. Kim, C. R. Lee, J. H. Im, K. B. Lee, T. Moehl, A. Marchioro, S. J. Moon, R. Humphry-Baker, J. H. Yum, J. E. Moser, M. Grätzel, and N. G. Park, Scientific Reports **2** (2012).
- N. J. Jeon, J. H. Noh, Y. C. Kim, W. S. Yang, S. Ryu, and S. I. Seok, Nature Materials 13 (9), 897 (2014).
- Sanwan Liu, Jingbai Li, Wenshan Xiao, Rui Chen, Zhenxing Sun, Yong Zhang, Xia Lei, Shuaifeng Hu, Manuel Kober-Czerny, Jianan Wang, Fumeng Ren, Qisen Zhou, Hasan Raza, You Gao, Yitong Ji, Sibo Li, Huan Li, Longbin Qiu, Wenchao Huang, Yan Zhao, Baomin Xu, Zonghao Liu, Henry J. Snaith, Nam-Gyu Park, and Wei Chen, Nature (2024).
- Jeong-Hyeok Im, In-Hyuk Jang, Norman Pellet, Michael Grätzel, and Nam-Gyu Park, Nature Nanotechnology **9** (11), 927 (2014).
- Hanul Min, Do Yoon Lee, Junu Kim, Gwisu Kim, Kyoung Su Lee, Jongbeom Kim, Min Jae Paik, Young Ki Kim, Kwang S. Kim, Min Gyu Kim, Tae Joo Shin, and Sang Il Seok, Nature **598** (7881), 444 (2021).
- Jason J. Yoo, Gabkyung Seo, Matthew R. Chua, Tae Gwan Park, Yongli Lu, Fabian Rotermund, Young-Ki Kim, Chan Su Moon, Nam Joong Jeon, Juan-Pablo Correa-Baena, Vladimir Bulović, Seong Sik Shin, Moungi G. Bawendi, and Jangwon Seo, Nature **590** (7847), 587 (2021).
- Xiong Li, Dongqin Bi, Chenyi Yi, Jean-David Décoppet, Jingshan Luo, Shaik Mohammed Zakeeruddin, Anders Hagfeldt, and Michael Grätzel, Science 353 (6294), 58 (2016).
- Yani Chen, Yong Sun, Jiajun Peng, Junhui Tang, Kaibo Zheng, and Ziqi Liang, Advanced Materials **30** (2), 1703487 (2018).
- Rachel E. Beal, Daniel J. Slotcavage, Tomas Leijtens, Andrea R. Bowring, Rebecca A. Belisle, William H. Nguyen, George F. Burkhard, Eric T. Hoke, and Michael D. McGehee, The Journal of Physical Chemistry Letters **7** (5), 746 (2016).
- James M. Ball and Annamaria Petrozza, Nature Energy 1 (11), 16149 (2016).
- Jongseob Kim, Sung-Hoon Lee, Jung Hoon Lee, and Ki-Ha Hong, The Journal of Physical Chemistry Letters **5** (8), 1312 (2014).
- Ajay Kumar Jena, Ashish Kulkarni, and Tsutomu Miyasaka, Chemical Reviews **119** (5), 3036 (2019).
- Wan-Jian Yin, Tingting Shi, and Yanfa Yan, The Journal of Physical Chemistry C 119 (10), 5253 (2015).

- Machteld E. Kamminga, Hong-Hua Fang, Marina R. Filip, Feliciano Giustino, Jacob Baas, Graeme R. Blake, Maria Antonietta Loi, and Thomas T. M. Palstra, Chemistry of Materials **28** (13), 4554 (2016).
- CBea Murray, David J Norris, and Moungi G Bawendi, Journal of the American Chemical Society **115** (19), 8706 (1993).
- L. E. Brus, The Journal of Chemical Physics **80** (9), 4403 (1984).
- ²² A. Shabaev, Al L. Efros, and A. J. Nozik, Nano Letters **6** (12), 2856 (2006).
- Octavi E. Semonin, Joseph M. Luther, and Matthew C. Beard, Materials Today **15** (11), 508 (2012).
- M. Ravindiran and C. Praveenkumar, Renewable and Sustainable Energy Reviews **94**, 317 (2018).
- Hironori Katagiri, Kazuo Jimbo, Win Shwe Maw, Koichiro Oishi, Makoto Yamazaki, Hideaki Araki, and Akiko Takeuchi, Thin Solid Films **517** (7), 2455 (2009).
- Arif D. Sheikh, Rahim Munir, Md Azimul Haque, Ashok Bera, Weijin Hu, Parvez Shaikh, Aram Amassian, and Tom Wu, ACS Applied Materials & Interfaces 9 (40), 35018 (2017).
- Rebecca L. Milot, Giles E. Eperon, Henry J. Snaith, Michael B. Johnston, and Laura M. Herz, Advanced Functional Materials **25** (39), 6218 (2015).
- Claudio Quarti, Edoardo Mosconi, James M Ball, Valerio D'Innocenzo, Chen Tao, Sandeep Pathak, Henry J Snaith, Annamaria Petrozza, and Filippo De Angelis, Energy & Environmental Science 9 (1), 155 (2016).
- Amalie Dualeh, Peng Gao, Sang II Seok, Mohammad Khaja Nazeeruddin, and Michael Grätzel, Chemistry of Materials **26** (21), 6160 (2014).
- Jiang He, Tianhui Li, Xueping Liu, Hang Su, Zhiliang Ku, Jie Zhong, Fuzhi Huang, Yong Peng, and Yi-Bing Cheng, Solar Energy **188**, 312 (2019).
- Emilio J. Juarez-Perez, Zafer Hawash, Sonia R. Raga, Luis K. Ono, and Yabing Qi, Energy & Environmental Science 9 (11), 3406 (2016).
- Zheng Fan, Hai Xiao, Yiliu Wang, Zipeng Zhao, Zhaoyang Lin, Hung-Chieh Cheng, Sung-Joon Lee, Gongming Wang, Ziying Feng, William A. Goddard, Yu Huang, and Xiangfeng Duan, Joule 1 (3), 548 (2017).
- Bert Conings, Jeroen Drijkoningen, Nicolas Gauquelin, Aslihan Babayigit, Jan D'Haen, Lien D'Olieslaeger, Anitha Ethirajan, Jo Verbeeck, Jean Manca, Edoardo Mosconi, Filippo De Angelis, and Hans-Gerd Boyen, Adv. Energy Mater. **5** (15), 1500477 (2015).
- G. A. Elbaz, W. L. Ong, E. A. Doud, P. Kim, D. W. Paley, X. Roy, and J. A. Malen, Nano Lett 17 (9), 5734 (2017).
- Sandip Thakur and Ashutosh Giri, ACS Applied Materials & Interfaces **15** (22), 26755 (2023).
- Tobias Haeger, Ralf Heiderhoff, and Thomas Riedl, Journal of Materials Chemistry C **8** (41), 14289 (2020).
- A. Pisoni, J. Jacimovic, O. S. Barisic, M. Spina, R. Gaal, L. Forro, and E. Horvath, J. Phys Chem Lett 5 (14), 2488 (2014).
- Ashutosh Giri, Alexander Z. Chen, Alessandro Mattoni, Kiumars Aryana, Depei Zhang, Xiao Hu, Seung-Hun Lee, Joshua J. Choi, and Patrick E. Hopkins, Nano Letters **20** (5), 3331 (2020).
- Xinyu Wang, Weitao Wang, Chao Yang, Dan Han, Hongzhao Fan, and Jingchao Zhang, Journal of Applied Physics **130** (17) (2021).

- AJ Angström, The London, Edinburgh, and Dublin Philosophical Magazine and Journal of Science **25** (166), 130 (1863).
- W. J. Parker, R. J. Jenkins, C. P. Butler, and G. L. Abbott, Journal of Applied Physics 32 (9), 1679 (1961).
- S. Sen, W. H. Konkel, S. J. Tighe, L. G. Bland, S. R. Sharma, and R. E. Taylor, Journal of Crystal Growth 86 (1), 111 (1988).
- Raisa-Ioana Biega, Menno Bokdam, Kai Herrmann, John Mohanraj, Dominik Skrybeck, Mukundan Thelakkat, Markus Retsch, and Linn Leppert, The Journal of Physical Chemistry C **127** (19), 9183 (2023).
- ⁴⁴ M. Wolf and D. Cahen, Solar Cells **27** (1), 247 (1989).
- I ISO. and BIPM OIML, Guide to the Expression of Uncertainty in Measurement. (Aenor, 1993).
- B. Hay, J. R. Filtz, J. Hameury, and L. Rongione, International Journal of Thermophysics **26** (6), 1883 (2005).
- Artem Lunev and Robert Heymer, Review of Scientific Instruments **91** (6) (2020).
- Baba Tetsuya and Ono Akira, Measurement Science and Technology **12** (12), 2046 (2001).
- 49 K. Shinzato and T. Baba, Journal of Thermal Analysis and Calorimetry **64** (1), 413 (2001).
- Jerzy Szalapak, Konrad Kiełbasiński, Jakub Krzemiński, Anna Mlozniak, Elżbieta Zwierkowska, Malgorzata Jakubowska, and Radosław Pawłowski, Metrology and Measurement Systems **22**, 521 (2015).
- Arnab Mandal, Sayan Goswami, Subarna Das, Diptikanta Swain, and Kanishka Biswas, Angewandte Chemie International Edition **63** (34), e202406616 (2024).
- Andrzej Kusiak, Jiri Martan, Jean-Luc Battaglia, and Rostislav Daniel, Thermochimica Acta **556**, 1 (2013).
- A. C. Tam and H. Sontag, in *Nondestructive Characterization of Materials II*, edited by Jean F. Bussière, Jean-Pierre Monchalin, Clayton O. Ruud et al. (Springer US, Boston, MA, 1987), pp. 355.
- J. W. Maclachlan and J. C. Murphy, in *Nondestructive Characterization of Materials II*, edited by Jean F. Bussière, Jean-Pierre Monchalin, Clayton O. Ruud et al. (Springer US, Boston, MA, 1987), pp. 777.
- Alexander Graham Bell, American Journal of Science **s3-20**, 305 (1880).
- ⁵⁶ Randall T Swimm, Appl. Phys. Lett. **42** (11), 955 (1983).
- P Charpentier, F Lepoutre, and L Bertrand, Journal of Applied Physics **53** (1), 608 (1982).
- O Pessoa, CL Cesar, NA Patel, H Vargas, CC Ghizoni, and LCM Miranda, Journal of applied physics **59** (4), 1316 (1986).
- ⁵⁹ Andrew C. Tam, Reviews of Modern Physics **58** (2), 381 (1986).
- 60 Edwin L Kerr, Applied Optics **12** (10), 2520 (1973).
- A. Rosencwaig, Analytical Chemistry 47 (6), 592A (1975).
- H. K. Wickramasinghe, R. C. Bray, V. Jipson, C. F. Quate, and J. R. Salcedo, Appl. Phys. Lett. 33 (11), 923 (1978).
- S. Govorkov, W. Ruderman, M. W. Horn, R. B. Goodman, and M. Rothschild, Review of Scientific Instruments **68** (10), 3828 (1997).
- ⁶⁴ M. J. Adams and G. F. Kirkbright, Analyst **102** (1213), 281 (1977).

- Yoh-Han Pao, Optoacoustic spectroscopy and detection. (Elsevier, 2012).
- Michael M. Farrow, Roger K. Burnham, Max Auzanneau, Steven L. Olsen, Neil Purdie, and Edward M. Eyring, Applied Optics 17 (7), 1093 (1978).
- Jing Wang, Tan Liu, Shuliang Jiao, Ruimin Chen, Qifa Zhou, K Kirk Shung, Lihong V Wang, and Hao F Zhang, Journal of biomedical optics **15** (2), 021317 (2010).
- 68 G. Busse and A. Ograbeck, Journal of Applied Physics **51** (7), 3576 (1980).
- 69 CL Cesar, H Vargas, and LCM Miranda, Appl. Phys. Lett. **43** (6), 555 (1983).
- Hanping Hu, Xinwei Wang, and Xianfan Xu, Journal of Applied Physics **86** (7), 3953 (1999).
- ⁷¹ Gu Liu, Applied Optics **21** (5), 955 (1982).
- Jean-Marc Heritier, Optics Communications **44** (4), 267 (1983).
- H. M. Lai and K. Young, The Journal of the Acoustical Society of America **72** (6), 2000 (1982).
- V. S. Teslenko, Soviet Journal of Quantum Electronics 7 (8), 981 (1977).
- TJ Burkey, M Majewski, and D Griller, Journal of the American Chemical Society **108** (9), 2218 (1986).
- V. A. Sablikov and V. B. Sandomirskii, physica status solidi (b) **120** (2), 471 (1983).
- ⁷⁷ R. Rosei and D. W. Lynch, Physical Review B **5** (10), 3883 (1972).
- E. Matatagui, A. G. Thompson, and Manuel Cardona, Physical Review **176** (3), 950 (1968).
- ⁷⁹ R. B. Wilson, Brent A. Apgar, Lane W. Martin, and David G. Cahill, Opt. Express **20** (27), 28829 (2012).
- Kikuo Ujihara, Journal of Applied Physics 43 (5), 2376 (1972).
- D. A. Young, C. Thomsen, H. T. Grahn, H. J. Maris, and J. Tauc, presented at the Phonon Scattering in Condensed Matter V, Berlin, Heidelberg, 1986 (unpublished).
- 82 Carolyn A. Paddock and Gary L. Eesley, Opt. Lett. **11** (5), 273 (1986).
- David G. Cahill, Wayne K. Ford, Kenneth E. Goodson, Gerald D. Mahan, Arun Majumdar, Humphrey J. Maris, Roberto Merlin, and Simon R. Phillpot, Journal of Applied Physics **93** (2), 793 (2003).
- Jun Liu, Jie Zhu, Miao Tian, Xiaokun Gu, Aaron Schmidt, and Ronggui Yang, Review of Scientific Instruments **84** (3) (2013).
- Zhe Cheng, Alex Weidenbach, Tianli Feng, M. Brooks Tellekamp, Sebastian Howard, Matthew J. Wahila, Bill Zivasatienraj, Brian Foley, Sokrates T. Pantelides, Louis F. J. Piper, William Doolittle, and Samuel Graham, Physical Review Materials **3** (2), 025002 (2019).
- Catalin Chiritescu, David G. Cahill, Ngoc Nguyen, David Johnson, Arun Bodapati, Pawel Keblinski, and Paul Zschack, Science **315** (5810), 351 (2007).
- Puqing Jiang, Xin Qian, and Ronggui Yang, Review of Scientific Instruments **88** (7) (2017).
- Puqing Jiang, Xin Qian, and Ronggui Yang, Journal of Applied Physics **124** (16) (2018).
- Aaron J. Schmidt, Xiaoyuan Chen, and Gang Chen, Review of Scientific Instruments **79** (11) (2008).
- T. Favaloro, J.-H. Bahk, and A. Shakouri, Review of Scientific Instruments **86** (2) (2015).
- Bo Sun and Yee Kan Koh, Review of Scientific Instruments **87** (6) (2016).

- Jie Zhu, Dawei Tang, Wei Wang, Jun Liu, Kristopher W. Holub, and Ronggui Yang, Journal of Applied Physics **108** (9) (2010).
- W. S. Capinski, H. J. Maris, T. Ruf, M. Cardona, K. Ploog, and D. S. Katzer, Physical Review B **59** (12), 8105 (1999).
- ⁹⁴ Yee Kan Koh, David G. Cahill, and Bo Sun, Physical Review B **90** (20), 205412 (2014).
- Ruxandra M. Costescu, Marcel A. Wall, and David G. Cahill, Physical Review B **67** (5), 054302 (2003).
- Aaron J. Schmidt, Ramez Cheaito, and Matteo Chiesa, Review of Scientific Instruments **80** (9) (2009).
- David G. Cahill, Review of Scientific Instruments **75** (12), 5119 (2004).
- Jia Yang, Elbara Ziade, and Aaron J. Schmidt, Review of Scientific Instruments 87 (1) (2016).
- ⁹⁹ Jeffrey L. Braun and Patrick E. Hopkins, Journal of Applied Physics **121** (17) (2017).
- David G. Cahill, Paul V. Braun, Gang Chen, David R. Clarke, Shanhui Fan, Kenneth E. Goodson, Pawel Keblinski, William P. King, Gerald D. Mahan, Arun Majumdar, Humphrey J. Maris, Simon R. Phillpot, Eric Pop, and Li Shi, Applied Physics Reviews 1 (1) (2014).
- Puqing Jiang, Xin Qian, and Ronggui Yang, Review of Scientific Instruments **89** (9) (2018).
- Zhe Cheng, Fengwen Mu, Xiaoyang Ji, Tiangui You, Wenhui Xu, Tadatomo Suga, Xin Ou, David G. Cahill, and Samuel Graham, ACS Appl. Mater. Interfaces 13 (27), 31843 (2021).
- David H. Olson, Jeffrey L. Braun, and Patrick E. Hopkins, Journal of Applied Physics **126** (15) (2019).
- Jeffrey L. Braun, David H. Olson, John T. Gaskins, and Patrick E. Hopkins, Review of Scientific Instruments **90** (2) (2019).
- David Rodin and Shannon K. Yee, Review of Scientific Instruments **88** (1) (2017).
- Keith T. Regner, Daniel P. Sellan, Zonghui Su, Cristina H. Amon, Alan J. H. McGaughey, and Jonathan A. Malen, Nature Communications **4** (1), 1640 (2013).
- A. J. Minnich, J. A. Johnson, A. J. Schmidt, K. Esfarjani, M. S. Dresselhaus, K. A. Nelson, and G. Chen, Phys. Rev. Lett. **107** (9), 095901 (2011).
- Hang Zhang, Xiangwen Chen, Young-Dahl Jho, and Austin J. Minnich, Nano Letters **16** (3), 1643 (2016).
- L. Wang, R. Cheaito, J. L. Braun, A. Giri, and P. E. Hopkins, Review of Scientific Instruments 87 (9) (2016).
- Xin Qian, Zhiwei Ding, Jungwoo Shin, Aaron J. Schmidt, and Gang Chen, Review of Scientific Instruments **91** (6) (2020).
- Christina M. Rost, Jeffrey Braun, Kevin Ferri, Lavina Backman, Ashutosh Giri, Elizabeth J. Opila, Jon-Paul Maria, and Patrick E. Hopkins, Appl. Phys. Lett. **111** (15) (2017).
- S. Li, Z. Dai, L. Li, N. P. Padture, and P. Guo, Rev Sci Instrum **93** (5), 053003 (2022).
- Bowen Li, Joy Xu, Conrad A. Kocoj, Shunran Li, Yanyan Li, Du Chen, Shuchen Zhang, Letian Dou, and Peijun Guo, Journal of the American Chemical Society **146** (3), 2187 (2024).
- Du Chen, Matthieu Fortin-Deschênes, Yuchen Lou, Huiju Lee, Joy Xu, Abrar A. Sheikh, Kenji Watanabe, Takashi Taniguchi, Yi Xia, Fengnian Xia, and Peijun Guo, The Journal of Physical Chemistry C **127** (19), 9121 (2023).

- Usama Choudhry, Taeyong Kim, Melanie Adams, Jeewan Ranasinghe, Runqing Yang, and Bolin Liao, Journal of Applied Physics **130** (23) (2021).
- Hans Joachim Eichler, Peter Günter, and Dieter W. Pohl, in *Laser-Induced Dynamic Gratings* (Springer Berlin Heidelberg, Berlin, Heidelberg, 1986), pp. 13.
- H. Eichler, G. Salje, and H. Stahl, Journal of Applied Physics 44 (12), 5383 (1973).
- Todd S. Rose, Roberto Righini, and M. D. Fayer, Chemical Physics Letters **106** (1), 13 (1984).
- Yu Bi, Eline M. Hutter, Yanjun Fang, Qingfeng Dong, Jinsong Huang, and Tom J. Savenije, The Journal of Physical Chemistry Letters 7 (5), 923 (2016).
- Felix Hofmann, Michael P. Short, and Cody A. Dennett, MRS Bull. 44 (5), 392 (2019).
- M. Fayer, IEEE Journal of Quantum Electronics 22 (8), 1437 (1986).
- Akira Harata, Hiroyuki Nishimura, and Tsuguo Sawada, Appl. Phys. Lett. **57** (2), 132 (1990).
- Chen Li, Hao Ma, Tianyang Li, Jinghang Dai, Md Abu Jafar Rasel, Alessandro Mattoni, Ahmet Alatas, Malcolm G. Thomas, Zachary W. Rouse, Avi Shragai, Shefford P. Baker, B. J. Ramshaw, Joseph P. Feser, David B. Mitzi, and Zhiting Tian, Nano Letters **21** (9), 3708 (2021).
- Lukas Rieland, Julian Wagner, Robin Bernhardt, Tianyi Wang, Omar Abdul-Aziz, Philipp Stein, Eva A. A. Pogna, Stefano Dal Conte, Giulio Cerullo, Hamoon Hedayat, and Paul H. M. van Loosdrecht, Nano Letters (2024).
- P. Ščajev, R. Aleksiejūnas, S. Terakawa, C. Qin, T. Fujihara, T. Matsushima, C. Adachi, and S. Juršėnas, The Journal of Physical Chemistry C **123** (24), 14914 (2019).
- O. W. Käding, H. Skurk, A. A. Maznev, and E. Matthias, Applied Physics A **61** (3), 253 (1995).
- W. B. Jackson, N. M. Amer, A. C. Boccara, and D. Fournier, Applied Optics 20 (8), 1333 (1981).
- ¹²⁸ A. C. Boccara, D. Fournier, and J. Badoz, Appl. Phys. Lett. **36** (2), 130 (1980).
- S. Akhmanov, D. Krindach, A. Migulin, A. Sukhorukov, and R. Khokhlov, IEEE Journal of Quantum Electronics 4 (10), 568 (1968).
- ¹³⁰ M. E. Long, Robert L. Swofford, and A. C. Albrecht, Science **191** (4223), 183 (1976).
- Susanne Sandell, Emigdio Chávez-Ángel, Alexandros El Sachat, Jianying He, Clivia M. Sotomayor Torres, and Jeremie Maire, Journal of Applied Physics **128** (13) (2020).
- Jay Deep Gupta, Priyanka Jangra, and Ashish Kumar Mishra, in *Raman Spectroscopy: Advances and Applications*, edited by Dheeraj Kumar Singh, Ashish Kumar Mishra, and Arnulf Materny (Springer Nature Singapore, Singapore, 2024), pp. 75.
- Ayberk Özden, Felix Drechsler, Jens Kortus, Marin Alexe, and Cameliu Himcinschi, Physical Review Materials **8** (1), 014407 (2024).
- Shaili Sett, Vishal Kumar Aggarwal, Achintya Singha, and A. K. Raychaudhuri, Physical Review Applied **13** (5), 054008 (2020).
- Alexander A. Balandin, Suchismita Ghosh, Wenzhong Bao, Irene Calizo, Desalegne Teweldebrhan, Feng Miao, and Chun Ning Lau, Nano Letters **8** (3), 902 (2008).
- Eilam Yalon, Burak Aslan, Kirby K. H. Smithe, Connor J. McClellan, Saurabh V. Suryavanshi, Feng Xiong, Aditya Sood, Christopher M. Neumann, Xiaoqing Xu, Kenneth E. Goodson, Tony F. Heinz, and Eric Pop, ACS Applied Materials & Interfaces 9 (49), 43013 (2017).

- Qin-Yi Li, Kailun Xia, Ji Zhang, Yingying Zhang, Qunyang Li, Koji Takahashi, and Xing Zhang, Nanoscale **9** (30), 10784 (2017).
- Shiqi Yin, Weitao Zhang, Chaoyang Tan, Lijie Chen, Jiawang Chen, Gang Li, Hanlin Zhang, Yu Zhang, Weike Wang, and Liang Li, The Journal of Physical Chemistry C **125** (29), 16129 (2021).
- Qin-Yi Li, Xing Zhang, and Yu-Dong Hu, Thermochimica Acta **592**, 67 (2014).
- Mladen Franko and Chieu D Tran, Encyclopedia of analytical chemistry, 1249 (2010).
- Andrew Skumanich, Daniele Fournier, A. Claude Boccara, and Nabil M. Amer, Appl. Phys. Lett. **47** (4), 402 (1985).
- Daniele Fournier, Claude Boccara, Andrew Skumanich, and Nabil M. Amer, Journal of Applied Physics **59** (3), 787 (1986).
- David G. Cahill, Review of Scientific Instruments **61** (2), 802 (1990).
- Dong-Wook Oh, Ankur Jain, John K. Eaton, Kenneth E. Goodson, and Joon Sik Lee, International Journal of Heat and Fluid Flow **29** (5), 1456 (2008).
- David G Cahill, My Katiyar, and JR Abelson, Physical review B **50** (9), 6077 (1994).
- 146 CE Raudzis, F Schatz, and D Wharam, Journal of applied physics 93 (10), 6050 (2003).
- Lorenzo Peri, Domenic Prete, Valeria Demontis, Elena Degoli, Alice Ruini, Rita Magri, and Francesco Rossella, Nanotechnology **34** (43), 435403 (2023).
- J. Pelzl, M. Chirtoc, and R. Meckenstock, International Journal of Thermophysics **34** (8), 1353 (2013).
- Braulio Beltrán-Pitarch, Benny Guralnik, Neetu Lamba, Andreas R. Stilling-Andersen, Lars Nørregaard, Torben M. Hansen, Ole Hansen, Nini Pryds, Peter F. Nielsen, and Dirch H. Petersen, Materials Today Physics **31**, 100963 (2023).
- T. Liu, S. Y. Yue, S. Ratnasingham, T. Degousee, P. Varsini, J. Briscoe, M. A. McLachlan, M. Hu, and O. Fenwick, ACS Appl Mater Interfaces 11 (50), 47507 (2019).
- 151 CC Williams and HK Wickramasinghe, Microelectronic Engineering 5 (1-4), 509 (1986).
- Yun Zhang, Wenkai Zhu, Fei Hui, Mario Lanza, Theodorian Borca-Tasciuc, and Miguel Muñoz Rojo, Advanced Functional Materials **30** (18), 1900892 (2020).
- G Mills, H Zhou, A Midha, L Donaldson, and JMR Weaver, Applied physics letters 72 (22), 2900 (1998).
- 154 I. W. Rangelow, T. Gotszalk, P. Grabiec, K. Edinger, and N. Abedinov, Microelectronic Engineering **57-58**, 737 (2001).
- Russell J Pylkki, Patrick J Moyer Patrick J Moyer, and Paul E West Paul E West, Japanese journal of applied physics **33** (6S), 3785 (1994).
- Stéphane Lefevre, J-B Saulnier, Catherine Fuentes, and Sebastian Volz, Superlattices and Microstructures **35** (3-6), 283 (2004).
- E Oesterschulze, M Stopka, L Ackermann, W Scholz, and S Werner, Journal of Vacuum Science & Technology B: Microelectronics and Nanometer Structures Processing, Measurement, and Phenomena **14** (2), 832 (1996).
- Séverine Gomès, Ali Assy, and Pierre Olivier Chapuis, physica status solidi (a) **212** (3), 477 (2015).
- Stéphane Lefevre, Sebastian Volz, Jean-Bernard Saulnier, Catherine Fuentes, and Nathalie Trannoy, Review of scientific instruments **74** (4), 2418 (2003).

- K. Luo, Z. Shi, J. Varesi, and A. Majumdar, Journal of Vacuum Science & Technology B: Microelectronics and Nanometer Structures Processing, Measurement, and Phenomena 15 (2), 349 (1997).
- Houfu Song, Jiaman Liu, Bilu Liu, Junqiao Wu, Hui-Ming Cheng, and Feiyu Kang, Joule **2** (3), 442 (2018).
- Weiwei Cai, Arden L. Moore, Yanwu Zhu, Xuesong Li, Shanshan Chen, Li Shi, and Rodney S. Ruoff, Nano Letters **10** (5), 1645 (2010).
- Insun Jo, Michael Thompson Pettes, Jaehyun Kim, Kenji Watanabe, Takashi Taniguchi, Zhen Yao, and Li Shi, Nano Letters **13** (2), 550 (2013).
- Motoo Fujii, Xing Zhang, Huaqing Xie, Hiroki Ago, Koji Takahashi, Tatsuya Ikuta, Hidekazu Abe, and Tetsuo Shimizu, Physical Review Letters **95** (6), 065502 (2005).
- P. Kim, L. Shi, A. Majumdar, and P. L. McEuen, Physical Review Letters **87** (21), 215502 (2001).
- Li Shi, Deyu Li, Choongho Yu, Wanyoung Jang, Dohyung Kim, Zhen Yao, Philip Kim, and Arunava Majumdar, Journal of Heat Transfer **125** (5), 881 (2003).
- Deyu Li, Yiying Wu, Philip Kim, Li Shi, Peidong Yang, and Arun Majumdar, Appl. Phys. Lett. **83** (14), 2934 (2003).
- Ernesto Freire, in *Protein Stability and Folding: Theory and Practice*, edited by Bret A. Shirley (Humana Press, Totowa, NJ, 1995), pp. 191.
- G. W. H. Höhne, W. F. Hemminger, and H.-J. Flammersheim, in *Differential Scanning Calorimetry* (Springer Berlin Heidelberg, Berlin, Heidelberg, 2003), pp. 147.
- Joel R. Seibert, Özgür Keleş, Jun Wang, and Folarin Erogbogbo, Polymer **185**, 121988 (2019).
- H. Chen, C. Liu, J. Xu, A. Maxwell, W. Zhou, Y. Yang, Q. Zhou, A. S. R. Bati, H. Wan, Z. Wang, L. Zeng, J. Wang, P. Serles, Y. Liu, S. Teale, Y. Liu, M. I. Saidaminov, M. Li, N. Rolston, S. Hoogland, T. Filleter, M. G. Kanatzidis, B. Chen, Z. Ning, and E. H. Sargent, Science 384 (6692), 189 (2024).
- Oi Jiang and Kai Zhu, Nature Reviews Materials (2024).
- Samuel D. Stranks, Victor M. Burlakov, Tomas Leijtens, James M. Ball, Alain Goriely, and Henry J. Snaith, Physical Review Applied 2 (3) (2014).
- T. Leijtens, S. D. Stranks, G. E. Eperon, R. Lindblad, E. M. Johansson, I. J. McPherson, H. Rensmo, J. M. Ball, M. M. Lee, and H. J. Snaith, ACS Nano 8 (7), 7147 (2014).
- S. D. Stranks, G. E. Eperon, G. Grancini, C. Menelaou, M. J. Alcocer, T. Leijtens, L. M. Herz, A. Petrozza, and H. J. Snaith, Science **342** (6156), 341 (2013).
- G. Xing, N. Mathews, S. Sun, S. S. Lim, Y. M. Lam, M. Gratzel, S. Mhaisalkar, and T. C. Sum, Science 342 (6156), 344 (2013).
- ¹⁷⁷ Q. Dong, Y. Fang, Y. Shao, P. Mulligan, J. Qiu, L. Cao, and J. Huang, Science **347** (6225), 967 (2015).
- D. Shi, V. Adinolfi, R. Comin, M. Yuan, E. Alarousu, A. Buin, Y. Chen, S. Hoogland, A. Rothenberger, K. Katsiev, Y. Losovyj, X. Zhang, P. A. Dowben, O. F. Mohammed, E. H. Sargent, and O. M. Bakr, Science **347** (6221), 519 (2015).
- M. Li, Y. Yang, Z. Kuang, C. Hao, S. Wang, F. Lu, Z. Liu, J. Liu, L. Zeng, Y. Cai, Y. Mao, J. Guo, H. Tian, G. Xing, Y. Cao, C. Ma, N. Wang, Q. Peng, L. Zhu, W. Huang, and J. Wang, Nature (2024).
- C. Qin, A. S. D. Sandanayaka, C. Zhao, T. Matsushima, D. Zhang, T. Fujihara, and C. Adachi, Nature **585** (7823), 53 (2020).

- ¹⁸¹ L. Yi, B. Hou, H. Zhao, and X. Liu, Nature **618** (7964), 281 (2023).
- J. Burschka, N. Pellet, S. J. Moon, R. Humphry-Baker, P. Gao, M. K. Nazeeruddin, and M. Gratzel, Nature **499** (7458), 316 (2013).
- Q. Chen, H. Zhou, Z. Hong, S. Luo, H. S. Duan, H. H. Wang, Y. Liu, G. Li, and Y. Yang, J Am Chem Soc **136** (2), 622 (2014).
- Luis K. Ono, Shenghao Wang, Yuichi Kato, Sonia R. Raga, and Yabing Qi, Energy Environ. Sci. 7 (12), 3989 (2014).
- B. R. Sutherland, S. Hoogland, M. M. Adachi, P. Kanjanaboos, C. T. Wong, J. J. McDowell, J. Xu, O. Voznyy, Z. Ning, A. J. Houtepen, and E. H. Sargent, Adv Mater 27 (1), 53 (2015).
- Hyun Suk Jung, Gill Sang Han, Nam-Gyu Park, and Min Jae Ko, Joule **3** (8), 1850 (2019).
- J. You, Z. Hong, Y. M. Yang, Q. Chen, M. Cai, T. B. Song, C. C. Chen, S. Lu, Y. Liu, H. Zhou, and Y. Yang, ACS Nano 8 (2), 1674 (2014).
- M. Saliba, T. Matsui, K. Domanski, J. Y. Seo, A. Ummadisingu, S. M. Zakeeruddin, J. P. Correa-Baena, W. R. Tress, A. Abate, A. Hagfeldt, and M. Gratzel, Science **354** (6309), 206 (2016).
- J. You, L. Meng, T. B. Song, T. F. Guo, Y. M. Yang, W. H. Chang, Z. Hong, H. Chen, H. Zhou, Q. Chen, Y. Liu, N. De Marco, and Y. Yang, Nat Nanotechnol 11 (1), 75 (2016).
- Y. Lin, Y. Bai, Y. Fang, Z. Chen, S. Yang, X. Zheng, S. Tang, Y. Liu, J. Zhao, and J. Huang, J Phys Chem Lett 9 (3), 654 (2018).
- Giles E. Eperon, Samuel D. Stranks, Christopher Menelaou, Michael B. Johnston, Laura M. Herz, and Henry J. Snaith, Energy & Environmental Science 7 (3) (2014).
- ¹⁹² S. H. Turren-Cruz, A. Hagfeldt, and M. Saliba, Science **362** (6413), 449 (2018).
- ¹⁹³ Fei Zhang and Kai Zhu, Adv. Energy Mater. **10** (13) (2019).
- Nicholas Rolston, Adam D. Printz, Jared M. Tracy, Hasitha C. Weerasinghe, Doojin Vak, Lew Jia Haur, Anish Priyadarshi, Nripan Mathews, Daniel J. Slotcavage, Michael D. McGehee, Roghi E. Kalan, Kenneth Zielinski, Ronald L. Grimm, Hsinhan Tsai, Wanyi Nie, Aditya D. Mohite, Somayeh Gholipour, Michael Saliba, Michael Grätzel, and Reinhold H. Dauskardt, Adv. Energy Mater. 8 (9) (2017).
- Sai Ma, Guizhou Yuan, Ying Zhang, Ning Yang, Yujing Li, and Qi Chen, Energy & Environmental Science **15** (1), 13 (2022).
- Hasitha C. Weerasinghe, Yasmina Dkhissi, Andrew D. Scully, Rachel A. Caruso, and Yi-Bing Cheng, Nano Energy **18**, 118 (2015).
- G. Grancini, C. Roldan-Carmona, I. Zimmermann, E. Mosconi, X. Lee, D. Martineau, S. Narbey, F. Oswald, F. De Angelis, M. Graetzel, and M. K. Nazeeruddin, Nat Commun 8, 15684 (2017).
- Jiangzhao Chen and Nam-Gyu Park, ACS Energy Letters 5 (8), 2742 (2020).
- Yanbo Wang, Youfeng Yue, Xudong Yang, and Liyuan Han, Adv. Energy Mater. **8** (22) (2018).
- Seong Sik Shin, Seon Joo Lee, and Sang Il Seok, Advanced Functional Materials **29** (47) (2019).
- Q. Jiang, R. Tirawat, R. A. Kerner, E. A. Gaulding, Y. Xian, X. Wang, J. M. Newkirk, Y. Yan, J. J. Berry, and K. Zhu, Nature 623 (7986), 313 (2023).
- Mingchao Wang and Shangchao Lin, Advanced Functional Materials **26** (29), 5297 (2016).

- L. Zhao, K. Roh, S. Kacmoli, K. Al Kurdi, S. Jhulki, S. Barlow, S. R. Marder, C. Gmachl, and B. P. Rand, Adv Mater 32 (25), e2000752 (2020).
- Fengtao Pei, Nengxu Li, Yihua Chen, Xiuxiu Niu, Yu Zhang, Zhenyu Guo, Zijian Huang, Huachao Zai, Guilin Liu, Yuanmou Zhang, Yang Bai, Xiao Zhang, Cheng Zhu, Qi Chen, Yan Li, and Huanping Zhou, ACS Energy Letters **6** (9), 3029 (2021).
- yong song Zhang, Zhen He, Jian Xiong, Shiping Zhan, Fu Liu, Meng Su, Dongjie Wang, Yu Huang, Qiaogan Liao, Jiang-rong Lu, Zheling Zhang, Changlai Yuan, Jiang Wang, Qilin Dai, and Jian Zhang, J. Mater. Chem. A (2024).
- Robert G. Morris and Jerome G. Hust, Physical Review 124 (5), 1426 (1961).
- R. O. Carlson, G. A. Slack, and S. J. Silverman, Journal of Applied Physics **36** (2), 505 (1965).
- Wenjun Liu and Mehdi Asheghi, Journal of Heat Transfer **128** (1), 75 (2006).
- Anton Kovalsky, Lili Wang, Gage T. Marek, Clemens Burda, and Jeffrey S. Dyck, The Journal of Physical Chemistry C **121** (6), 3228 (2017).
- Ralf Heiderhoff, Tobias Haeger, Neda Pourdavoud, Ting Hu, Mine Al-Khafaji, Andre Mayer, Yiwang Chen, Hella-Christin Scheer, and Thomas Riedl, The Journal of Physical Chemistry C **121** (51), 28306 (2017).
- Roman Anufriev, Jose Ordonez-Miranda, and Masahiro Nomura, Physical Review B **101** (11) (2020).
- J. Zhao, Y. Ying, H. Zeng, K. Zhao, G. Li, and W. Li, ACS Appl Mater Interfaces 15 (9), 12502 (2023).
- Qi Chen, Chunfeng Zhang, Mengya Zhu, Shenghua Liu, Mark E. Siemens, Shuai Gu, Jia Zhu, Jiancang Shen, Xinglong Wu, Chen Liao, Jiayu Zhang, Xiaoyong Wang, and Min Xiao, Appl. Phys. Lett. **108** (8) (2016).
- ²¹⁴ Zhi Guo, Seog Joon Yoon, Joseph S. Manser, Prashant V. Kamat, and Tengfei Luo, The Journal of Physical Chemistry C **120** (12), 6394 (2016).
- G. Wang, H. Fan, Z. Chen, Y. Gao, Z. Wang, Z. Li, H. Lu, and Y. Zhou, Adv Sci (Weinh), e2401194 (2024).
- Tao Ye, Xizu Wang, Xianqiang Li, Alex Qingyu Yan, Seeram Ramakrishna, and Jianwei Xu, Journal of Materials Chemistry C **5** (5), 1255 (2017).
- Chunyu Ge, Mingyu Hu, Peng Wu, Qi Tan, Zhizhong Chen, Yiping Wang, Jian Shi, and Jing Feng, The Journal of Physical Chemistry C **122** (28), 15973 (2018).
- Xiang Long, Zhenyu Pan, Zhuolei Zhang, Jeffrey J. Urban, and Heng Wang, Applied Physics Letters **115** (7) (2019).
- Md Azimul Haque, Mohamad Insan Nugraha, Sri Harish Kumar Paleti, and Derya Baran, The Journal of Physical Chemistry C **123** (24), 14928 (2019).
- Y. Wang, R. Lin, P. Zhu, Q. Zheng, Q. Wang, D. Li, and J. Zhu, Nano Lett **18** (5), 2772 (2018).
- C. Shen, W. Du, Z. Wu, J. Xing, S. T. Ha, Q. Shang, W. Xu, Q. Xiong, X. Liu, and Q. Zhang, Nanoscale 9 (24), 8281 (2017).
- Namphung Peimyoo, Jingzhi Shang, Weihuang Yang, Yanlong Wang, Chunxiao Cong, and Ting Yu, Nano Research 8 (4), 1210 (2014).
- Satyaprakash Sahoo, Anand P. S. Gaur, Majid Ahmadi, Maxime J. F. Guinel, and Ram S. Katiyar, The Journal of Physical Chemistry C **117** (17), 9042 (2013).
- ²²⁴ S. Zhou, X. Tao, and Y. Gu, The Journal of Physical Chemistry C **120** (9), 4753 (2016).

- ²²⁵ A. A. Balandin, S. Ghosh, W. Bao, I. Calizo, D. Teweldebrhan, F. Miao, and C. N. Lau, Nano Lett **8** (3), 902 (2008).
- Xiaobo Li, Kurt Maute, Martin L. Dunn, and Ronggui Yang, Physical Review B **81** (24) (2010).
- Xin Qian, Xiaokun Gu, and Ronggui Yang, The Journal of Physical Chemistry C 119 (51), 28300 (2015).
- Ashutosh Giri, Sandip Thakur, and Alessandro Mattoni, Chemistry of Materials **34** (21), 9569 (2022).
- Sebastian G. Volz and Gang Chen, Physical Review B 61 (4), 2651 (2000).
- ²³⁰ A. J. Ladd, B. Moran, and W. G. Hoover, Phys Rev B Condens Matter **34** (8), 5058 (1986).
- Xin Qian, Xiaokun Gu, and Ronggui Yang, Appl. Phys. Lett. 108 (6) (2016).
- Jun Kang and Lin-Wang Wang, Physical Review B **96** (2) (2017).
- Sheng-Ying Yue, Xiaoliang Zhang, Guangzhao Qin, Jiayue Yang, and Ming Hu, Physical Review B **94** (11) (2016).
- Lucy D. Whalley, Jonathan M. Skelton, Jarvist M. Frost, and Aron Walsh, Physical Review B **94** (22) (2016).
- W. Lee, H. Li, A. B. Wong, D. Zhang, M. Lai, Y. Yu, Q. Kong, E. Lin, J. J. Urban, J. C. Grossman, and P. Yang, Proc Natl Acad Sci U S A 114 (33), 8693 (2017).
- Tobias Haeger, Maximilian Wilmes, Ralf Heiderhoff, and Thomas Riedl, The Journal of Physical Chemistry Letters **10** (11), 3019 (2019).
- Tobias Haeger, Moritz Ketterer, Johannes Bahr, Neda Pourdavoud, Manuel Runkel, Ralf Heiderhoff, and Thomas Riedl, Journal of Physics: Materials **3** (2), 024004 (2020).
- Zhelu Hu, Lionel Aigouy, Zhuoying Chen, and Danièle Fournier, Journal of Applied Physics **127** (12) (2020).
- Feng Qian, Mingyu Hu, Jue Gong, Chunyu Ge, Yunxuan Zhou, Jun Guo, Min Chen, Zhenhua Ge, Nitin P. Padture, Yuanyuan Zhou, and Jing Feng, The Journal of Physical Chemistry C **124** (22), 11749 (2020).
- Yingyue Zhang, Qishun Yao, Jiangchao Qian, Xiaohui Zhao, Dongdong Li, and Qixi Mi, Chemical Physics Letters **754** (2020).
- H. Xie, S. Hao, J. Bao, T. J. Slade, G. J. Snyder, C. Wolverton, and M. G. Kanatzidis, J Am Chem Soc 142 (20), 9553 (2020).
- Arnab Mandal, Sayan Goswami, Subarna Das, Diptikanta Swain, and Kanishka Biswas, Angewandte Chemie International Edition **n/a** (n/a), e202406616.
- Tiejun Zhu, Yintu Liu, Chenguang Fu, Joseph P. Heremans, Jeffrey G. Snyder, and Xinbing Zhao, Advanced Materials **29** (14), 1605884 (2017).
- Xiaoying Huang, Mojgan Roushan, Thomas J. Emge, Wenhua Bi, Suraj Thiagarajan,
 Jen-Hao Cheng, Ronggui Yang, and Jing Li, Angewandte Chemie International Edition
 48 (42), 7871 (2009).
- Kristopher J Erickson, François Léonard, Vitalie Stavila, Michael E Foster, Catalin D Spataru, Reese E Jones, Brian M Foley, Patrick E Hopkins, Mark D Allendorf, and A Alec Talin, Advanced Materials **27** (22), 3453 (2015).
- Yu-Ran Luo, Comprehensive Handbook of Chemical Bond Energies. (2007).
- E. Isotta, W. Peng, A. Balodhi, and A. Zevalkink, Angew Chem Int Ed Engl **62** (12), e202213649 (2023).
- ²⁴⁸ Z. Fan, H. Wang, Y. Wu, X. J. Liu, and Z. P. Lu, RSC Adv. 6 (57), 52164 (2016).

- Xueliang Yan, Loic Constantin, Yongfeng Lu, Jean François Silvain, Michael Nastasi, and Bai Cui, Journal of the American Ceramic Society **101** (10), 4486 (2018).
- Jianfeng Cai, Junxuan Yang, Guoqiang Liu, Hongxiang Wang, Fanfan Shi, Xiaojian Tan, Zhenhua Ge, and Jun Jiang, Materials Today Physics **18** (2021).
- ²⁵¹ Joseph Callaway, Physical Review **113** (4), 1046 (1959).
- W. R. Thurber and A. J. H. Mante, Physical Review **139** (5A), A1655 (1965).
- John S. Tse and Mary Anne White, The Journal of Physical Chemistry **92** (17), 5006 (2002).
- Y. Bouyrie, C. Candolfi, S. Pailhes, M. M. Koza, B. Malaman, A. Dauscher, J. Tobola, O. Boisron, L. Saviot, and B. Lenoir, Phys Chem Chem Phys 17 (30), 19751 (2015).
- Paribesh Acharyya, Tanmoy Ghosh, Koushik Pal, Kaushik Kundu, Kewal Singh Rana, Juhi Pandey, Ajay Soni, Umesh V. Waghmare, and Kanishka Biswas, Journal of the American Chemical Society 142 (36), 15595 (2020).
- Md Abu Jafar Rasel, Ashutosh Giri, David H. Olson, Chaoying Ni, Patrick E. Hopkins, and Joseph P. Feser, ACS Appl. Mater. Interfaces **12** (48), 53705 (2020).
- Sandip Thakur, Zhenghong Dai, Pravin Karna, Nitin P. Padture, and Ashutosh Giri, Materials Horizons 9 (12), 3087 (2022).
- Nabeel S Dahod, Watcharaphol Paritmongkol, and William A Tisdale, arXiv preprint arXiv:2303.17397 (2023).
- Ankit Negi, Liang Yan, Cong Yang, Yeonju Yu, Doyun Kim, Subhrangsu Mukherjee, Andrew H. Comstock, Saqlain Raza, Ziqi Wang, Dali Sun, Harald Ade, Qing Tu, Wei You, and Jun Liu, ACS Nano **18** (22), 14218 (2024).
- Alexander D. Christodoulides, Peijun Guo, Lingyun Dai, Justin M. Hoffman, Xiaotong Li, Xiaobing Zuo, Daniel Rosenmann, Alexandra Brumberg, Mercouri G. Kanatzidis, Richard D. Schaller, and Jonathan A. Malen, ACS Nano 15 (3), 4165 (2021).
- Peijun Guo, Constantinos C. Stoumpos, Lingling Mao, Sridhar Sadasivam, John B. Ketterson, Pierre Darancet, Mercouri G. Kanatzidis, and Richard D. Schaller, Nature Communications 9 (1), 2019 (2018).
- Yi-Hsiang Wang, Cheng-Hsien Yeh, I-Ta Hsieh, Po-Yu Yang, Yuan-Wen Hsiao, Hsuan-Ta Wu, Chun-Wei Pao, and Chuan-Feng Shih, Nanomaterials **14** (5), 446 (2024).
- Maria N. Luckyanova, Jivtesh Garg, Keivan Esfarjani, Adam Jandl, Mayank T. Bulsara, Aaron J. Schmidt, Austin J. Minnich, Shuo Chen, Mildred S. Dresselhaus, Zhifeng Ren, Eugene A. Fitzgerald, and Gang Chen, Science **338** (6109), 936 (2012).
- ²⁶⁴ G. Chen and M. Neagu, Appl. Phys. Lett. **71** (19), 2761 (1997).
- ²⁶⁵ B. Yang and G. Chen, Physical Review B **67** (19), 195311 (2003).
- Wee-Liat Ong, Shubhaditya Majumdar, Jonathan A. Malen, and Alan J. H. McGaughey, The Journal of Physical Chemistry C **118** (14), 7288 (2014).
- Mark D. Losego, Martha E. Grady, Nancy R. Sottos, David G. Cahill, and Paul V. Braun, Nat. Mater. 11 (6), 502 (2012).
- Zhaohui Wang, Jeffrey A. Carter, Alexei Lagutchev, Yee Kan Koh, Nak-Hyun Seong,
 David G. Cahill, and Dana D. Dlott, Science 317 (5839), 787 (2007).
- Muhan Cao, Yashvi Damji, Congyang Zhang, Linzhong Wu, Qixuan Zhong, Pengli Li, Di Yang, Yong Xu, and Qiao Zhang, Small Methods 4 (12), 2000303 (2020).
- Duyen H. Cao, Constantinos C. Stoumpos, Omar K. Farha, Joseph T. Hupp, and Mercouri G. Kanatzidis, Journal of the American Chemical Society **137** (24), 7843 (2015).

- Hsinhan Tsai, Wanyi Nie, Jean-Christophe Blancon, Constantinos C. Stoumpos, Reza Asadpour, Boris Harutyunyan, Amanda J. Neukirch, Rafael Verduzco, Jared J. Crochet, Sergei Tretiak, Laurent Pedesseau, Jacky Even, Muhammad A. Alam, Gautam Gupta, Jun Lou, Pulickel M. Ajayan, Michael J. Bedzyk, Mercouri G. Kanatzidis, and Aditya D. Mohite, Nature **536** (7616), 312 (2016).
- Ming Shao, Tong Bie, Lvpeng Yang, Yerun Gao, Xing Jin, Feng He, Nan Zheng, Yu Yu, and Xinliang Zhang, Advanced Materials **34** (1), 2107211 (2022).
- Martin A. Green, Ewan D. Dunlop, Masahiro Yoshita, Nikos Kopidakis, Karsten Bothe, Gerald Siefer, and Xiaojing Hao, Progress in Photovoltaics: Research and Applications **31** (7), 651 (2023).
- Ian C. Smith, Eric T. Hoke, Diego Solis-Ibarra, Michael D. McGehee, and Hemamala I. Karunadasa, Angewandte Chemie International Edition **53** (42), 11232 (2014).
- Lioz Etgar, Energy & Environmental Science 11 (2), 234 (2018).
- Mohamed M. Elsenety, Maria Antoniadou, Nikolaos Balis, Andreas Kaltzoglou, Labrini Sygellou, Anastasios Stergiou, Nikos Tagmatarchis, and Polycarpos Falaras, ACS Applied Energy Materials **3** (3), 2465 (2020).
- Anurag Krishna, Sébastien Gottis, Mohammad Khaja Nazeeruddin, and Frédéric Sauvage, Advanced Functional Materials **29** (8), 1806482 (2019).
- Andrew H. Proppe, Andrew Johnston, Sam Teale, Arup Mahata, Rafael Quintero-Bermudez, Eui Hyuk Jung, Luke Grater, Teng Cui, Tobin Filleter, Chang-Yong Kim, Shana O. Kelley, Filippo De Angelis, and Edward H. Sargent, Nature Communications 12 (1), 3472 (2021).
- Tianwei Duan, Shuai You, Min Chen, Wenjian Yu, Yanyan Li, Peijun Guo, Joseph J. Berry, Joseph M. Luther, Kai Zhu, and Yuanyuan Zhou, Science **384** (6698), 878 (2024).
- Peirong Liu, Shouwu Yu, and Shujuan Xiao, Sustainable Energy & Fuels **5** (16), 3950 (2021).
- Bayrammurad Saparov and David B. Mitzi, Chemical Reviews 116 (7), 4558 (2016).
- Daniel B. Straus and Cherie R. Kagan, The Journal of Physical Chemistry Letters 9 (6), 1434 (2018).
- Claudine Katan, Nicolas Mercier, and Jacky Even, Chemical Reviews **119** (5), 3140 (2019).
- Huan Wang and Dong Ha Kim, Chemical Society Reviews 46 (17), 5204 (2017).
- Jinwoo Byun, Himchan Cho, Christoph Wolf, Mi Jang, Aditya Sadhanala, Richard H. Friend, Hoichang Yang, and Tae-Woo Lee, Advanced Materials **28** (34), 7515 (2016).
- Chuanjiang Qin, Toshinori Matsushima, William J. Potscavage, Atula S. D. Sandanayaka, Matthew R. Leyden, Fatima Bencheikh, Kenichi Goushi, Fabrice Mathevet, Benoît Heinrich, Go Yumoto, Yoshihiko Kanemitsu, and Chihaya Adachi, Nature Photonics 14 (2), 70 (2020).
- Jun Xing, Yongbiao Zhao, Mikhail Askerka, Li Na Quan, Xiwen Gong, Weijie Zhao, Jiaxin Zhao, Hairen Tan, Guankui Long, Liang Gao, Zhenyu Yang, Oleksandr Voznyy, Jiang Tang, Zheng-Hong Lu, Qihua Xiong, and Edward H. Sargent, Nature Communications 9 (1), 3541 (2018).
- Sheng-Ning Hsu, Wenchao Zhao, Yao Gao, Akriti, Mauricio Segovia, Xianfan Xu, Bryan W. Boudouris, and Letian Dou, Nano Letters **21** (18), 7839 (2021).
- Xiaotong Li, Justin M. Hoffman, and Mercouri G. Kanatzidis, Chemical Reviews 121
 (4), 2230 (2021).

- Lingling Mao, Constantinos C. Stoumpos, and Mercouri G. Kanatzidis, Journal of the American Chemical Society **141** (3), 1171 (2019).
- Constantinos C. Stoumpos, Duyen H. Cao, Daniel J. Clark, Joshua Young, James M. Rondinelli, Joon I. Jang, Joseph T. Hupp, and Mercouri G. Kanatzidis, Chemistry of Materials 28 (8), 2852 (2016).
- Haiyan Wang, Qiaohe Wang, Mengxin Ning, Sen Li, Renzhong Xue, Peng Chen, and Zijiong Li, RSC Adv. **13** (33), 22886 (2023).
- Shuai Wang, Jiaqi Ma, Wancai Li, Jun Wang, Haizhen Wang, Hongzhi Shen, Junze Li, Jiaqi Wang, Hongmei Luo, and Dehui Li, The Journal of Physical Chemistry Letters **10** (10), 2546 (2019).
- Jianfeng Yang, Xiaoming Wen, Hongze Xia, Rui Sheng, Qingshan Ma, Jincheol Kim, Patrick Tapping, Takaaki Harada, Tak W. Kee, Fuzhi Huang, Yi-Bing Cheng, Martin Green, Anita Ho-Baillie, Shujuan Huang, Santosh Shrestha, Robert Patterson, and Gavin Conibeer, Nature Communications 8 (1), 14120 (2017).
- Candida Pipitone, Stefano Boldrini, Alberto Ferrario, Gonzalo Garcia-Espejo, Antonietta Guagliardi, Norberto Masciocchi, Antonino Martorana, and Francesco Giannici, Appl. Phys. Lett. 119 (10) (2021).
- ²⁹⁶ C. J. Glassbrenner and Glen A. Slack, Physical Review **134** (4A), A1058 (1964).
- ²⁹⁷ A. V. Inyushkin, Journal of Applied Physics **134** (22) (2023).
- ²⁹⁸ Nurul Ahad Akil and San-Dong Guo, J. Electron. Mater. **52** (5), 3401 (2023).
- Catherine M. Mauck, Arthur France-Lanord, Alexander C. Hernandez Oendra, Nabeel S. Dahod, Jeffrey C. Grossman, and William A. Tisdale, The Journal of Physical Chemistry C 123 (45), 27904 (2019).
- Hao Ma, Chen Li, Yunwei Ma, Heng Wang, Zachary W Rouse, Zhuolei Zhang, Carla Slebodnick, Ahmet Alatas, Shefford P. Baker, Jeffrey J. Urban, and Zhiting Tian, Phys. Rev. Lett. **123** (15), 155901 (2019).
- Md Azimul Haque, Seyoung Kee, Diego Rosas Villalva, Wee-Liat Ong, and Derya Baran, Adv. Sci. 7 (10), 1903389 (2020).
- Patrick E. Hopkins and Edward S. Piekos, Appl. Phys. Lett. **94** (18) (2009).
- Nabeel S. Dahod, Arthur France-Lanord, Watcharaphol Paritmongkol, Jeffrey C. Grossman, and William A. Tisdale, The Journal of Chemical Physics **153** (4) (2020).
- Shubhaditya Majumdar, Jonatan A. Sierra-Suarez, Scott N. Schiffres, Wee-Liat Ong, C. Fred Higgs, III, Alan J. H. McGaughey, and Jonathan A. Malen, Nano Letters **15** (5), 2985 (2015).
- Ashutosh Giri, Janne-Petteri Niemelä, Tommi Tynell, John T. Gaskins, Brian F. Donovan, Maarit Karppinen, and Patrick E. Hopkins, Physical Review B **93** (11), 115310 (2016).
- Ashutosh Giri, Janne-Petteri Niemelä, Chester J. Szwejkowski, Maarit Karppinen, and Patrick E. Hopkins, Physical Review B **93** (2), 024201 (2016).
- Ashutosh Giri, Sean W. King, William A. Lanford, Antonio B. Mei, Devin Merrill, Liyi Li, Ron Oviedo, John Richards, David H. Olson, Jeffrey L. Braun, John T. Gaskins, Freddy Deangelis, Asegun Henry, and Patrick E. Hopkins, Advanced Materials **30** (44), 1804097 (2018).
- ³⁰⁸ G. Chen, Physical Review B **57** (23), 14958 (1998).
- Shouwu Yu, Peirong Liu, and Shujuan Xiao, Journal of Materials Science **56** (20), 11656 (2021).

- Aryeh Gold-Parker, Peter M. Gehring, Jonathan M. Skelton, Ian C. Smith, Dan Parshall, Jarvist M. Frost, Hemamala I. Karunadasa, Aron Walsh, and Michael F. Toney, Proceedings of the National Academy of Sciences **115** (47), 11905 (2018).
- Pierre-Adrien Mante, Constantinos C. Stoumpos, Mercouri G. Kanatzidis, and Arkady Yartsev, Nature Communications **8** (1), 14398 (2017).
- D. König, K. Casalenuovo, Y. Takeda, G. Conibeer, J. F. Guillemoles, R. Patterson, L. M. Huang, and M. A. Green, Physica E: Low-dimensional Systems and Nanostructures 42 (10), 2862 (2010).
- Partha Maity, Jun Yin, Bin Cheng, Jr-Hau He, Osman M. Bakr, and Omar F. Mohammed, The Journal of Physical Chemistry Letters **10** (17), 5259 (2019).
- M. V. Simkin and G. D. Mahan, Phys. Rev. Lett. **84** (5), 927 (2000).
- Shin-ichiro Tamura, Yukihiro Tanaka, and Humphrey J. Maris, Physical Review B **60** (4), 2627 (1999).
- Miao-Ling Lin, Balaji Dhanabalan, Giulia Biffi, Yu-Chen Leng, Seda Kutkan, Milena P. Arciniegas, Ping-Heng Tan, and Roman Krahne, Small **18** (15), 2106759 (2022).
- Albrecht Bartels, Thomas Dekorsy, Heinrich Kurz, and Klaus Köhler, Phys. Rev. Lett. **82** (5), 1044 (1999).
- C. Colvard, R. Merlin, M. V. Klein, and A. C. Gossard, Phys. Rev. Lett. **45** (4), 298 (1980).
- ³¹⁹ A. S. Barker, J. L. Merz, and A. C. Gossard, Physical Review B **17** (8), 3181 (1978).
- Hyejin Jang, Joshua D. Wood, Christopher R. Ryder, Mark C. Hersam, and David G. Cahill, Advanced Materials **27** (48), 8017 (2015).
- Puqing Jiang, Xin Qian, Ronggui Yang, and Lucas Lindsay, Physical Review Materials **2** (6), 064005 (2018).
- Jun Liu, Gyung-Min Choi, and David G. Cahill, Journal of Applied Physics **116** (23) (2014).
- Puqing Jiang, Xin Qian, Xiaokun Gu, and Ronggui Yang, Advanced Materials **29** (36), 1701068 (2017).
- Xiaoming Zhao, Tianran Liu, and Yueh-Lin Loo, Advanced Materials **34** (3), 2105849 (2022).
- Abhishek Maiti, Khushboo Agarwal, Sergio Gonzalez-Munoz, and Oleg V. Kolosov, Physical Review Materials 7 (2), 023801 (2023).
- Robert McKinney, Prashun Gorai, Eric S. Toberer, and Vladan Stevanović, Chemistry of Materials **31** (6), 2048 (2019).
- Paribesh Acharyya, Tanmoy Ghosh, Koushik Pal, Kewal Singh Rana, Moinak Dutta, Diptikanta Swain, Martin Etter, Ajay Soni, Umesh V. Waghmare, and Kanishka Biswas, Nature Communications **13** (1), 5053 (2022).
- David G. Billing and Andreas Lemmerer, Acta Crystallographica Section B **63** (5), 735 (2007).
- GS Nolas and HJ Goldsmid, in *Thermal Conductivity: Theory, Properties, and Applications* (Springer, 2004), pp. 105.
- Sandip Tiwari, Compound semiconductor device physics. (Academic press, 2013).
- H. R. Shanks, P. D. Maycock, P. H. Sidles, and G. C. Danielson, Physical Review 130 (5), 1743 (1963).
- Songyang Yuan, Jiahuan Deng, Hui Xiong, Wenwen Wu, Zhipeng Ma, Mengqi Wang, Wenzhe Li, and Jiandong Fan, J. Mater. Chem. A **11** (36), 19685 (2023).

- Jiangwei Li, Qin Yu, Yihui He, Constantinos C. Stoumpos, Guangda Niu, Giancarlo G. Trimarchi, Hang Guo, Guifang Dong, Dong Wang, Liduo Wang, and Mercouri G. Kanatzidis, Journal of the American Chemical Society **140** (35), 11085 (2018).
- JJ Alvarado, O Zelaya Angel, F Sánchez Sinencio, G Torres Delgado, H Vargas, and J González Hernández, Journal of applied physics **76** (11), 7217 (1994).
- Woochul Lee, Huashan Li, Andrew B. Wong, Dandan Zhang, Minliang Lai, Yi Yu, Qiao Kong, Elbert Lin, Jeffrey J. Urban, Jeffrey C. Grossman, and Peidong Yang, Proceedings of the National Academy of Sciences **114** (33), 8693 (2017).
- Otfried Madelung, in *Semiconductors: Data Handbook*, edited by Otfried Madelung (Springer Berlin Heidelberg, Berlin, Heidelberg, 2004), pp. 173.
- Otfried Madelung, in *Semiconductors: Data Handbook*, edited by Otfried Madelung (Springer Berlin Heidelberg, Berlin, Heidelberg, 2004), pp. 71.
- S. Mei and I. Knezevic, Journal of Applied Physics 118 (17) (2015).
- Won-Yong Lee, Jung-Hoon Lee, Jae-Young Ahn, Tae-Hyun Park, No-Won Park, Gil-Sung Kim, Jin-Seong Park, and Sang-Kwon Lee, Nanotechnology **28** (10), 105401 (2017).
- Jingyu Li, Liuming Wei, Zhuoyang Ti, Le Ma, Yuli Yan, Guangbiao Zhang, and Peng-Fei Liu, Physical Review B **108** (22), 224302 (2023).
- Mritunjaya Parashar, Ranbir Singh, Kicheon Yoo, and Jae-Joon Lee, ACS Applied Energy Materials 4 (3), 2751 (2021).
- Yanqiang Hu, Ting Qiu, Fan Bai, Wei Ruan, and Shufang Zhang, Adv. Energy Mater. **8** (19), 1703620 (2018).
- Zheng Zhang, Xiaowei Li, Xiaohong Xia, Zhuo Wang, Zhongbing Huang, Binglong Lei, and Yun Gao, The Journal of Physical Chemistry Letters **8** (17), 4300 (2017).
- Mengqin Kong, Hang Hu, Li Wan, Miaomiao Chen, Yisheng Gan, Jia Wang, Fengxiang Chen, Binghai Dong, Dominik Eder, and Shimin Wang, RSC Adv. 7 (56), 35549 (2017).
- Guangbiao Xiang, Yanwen Wu, Man Zhang, Chen Cheng, Jiancai Leng, and Hong Ma, Nanomaterials **11** (10), 2712 (2021).
- Kyle M. McCall, Constantinos C. Stoumpos, Oleg Y. Kontsevoi, Grant C. B. Alexander, Bruce W. Wessels, and Mercouri G. Kanatzidis, Chemistry of Materials **31** (7), 2644 (2019).
- Anna J. Lehner, Douglas H. Fabini, Hayden A. Evans, Claire-Alice Hébert, Sara R. Smock, Jerry Hu, Hengbin Wang, Josef W. Zwanziger, Michael L. Chabinyc, and Ram Seshadri, Chemistry of Materials **27** (20), 7137 (2015).
- Paribesh Acharyya, Koushik Pal, Abdul Ahad, Debattam Sarkar, Kewal Singh Rana, Moinak Dutta, Ajay Soni, Umesh V. Waghmare, and Kanishka Biswas, Advanced Functional Materials **33** (41), 2304607 (2023).
- Byung-Wook Park, Bertrand Philippe, Xiaoliang Zhang, Håkan Rensmo, Gerrit Boschloo, and Erik M. J. Johansson, Advanced Materials **27** (43), 6806 (2015).
- Md Azimul Haque, Appala Naidu Gandi, Rajeshkumar Mohanraman, Yakui Weng, Bambar Davaasuren, Abdul-Hamid Emwas, Craig Combe, Derya Baran, Alexander Rothenberger, Udo Schwingenschlögl, Husam N. Alshareef, Shuai Dong, and Tom Wu, Advanced Functional Materials **29** (13), 1809166 (2019).
- A. C. Ferreira, A. Letoublon, S. Paofai, S. Raymond, C. Ecolivet, B. Ruffle, S. Cordier, C. Katan, M. I. Saidaminov, A. A. Zhumekenov, O. M. Bakr, J. Even, and P. Bourges, Phys Rev Lett **121** (8), 085502 (2018).

- I. P. Swainson, M. G. Tucker, D. J. Wilson, B. Winkler, and V. Milman, Chemistry of Materials **19** (10), 2401 (2007).
- B. Li, Y. Kawakita, Y. Liu, M. Wang, M. Matsuura, K. Shibata, S. Ohira-Kawamura, T. Yamada, S. Lin, K. Nakajima, and S. F. Liu, Nat Commun **8**, 16086 (2017).
- Li Na Quan, Yoonjae Park, Peijun Guo, Mengyu Gao, Jianbo Jin, Jianmei Huang, Jason K. Copper, Adam Schwartzberg, Richard Schaller, David T. Limmer, and Peidong Yang, Proceedings of the National Academy of Sciences **118** (25), e2104425118 (2021).
- Cong Yang, Saqlain Raza, Xiaobo Li, and Jun Liu, The Journal of Physical Chemistry B **127** (30), 6804 (2023).
- Qing Tu, Doyun Kim, Mohammed Shyikh, and Mercouri G. Kanatzidis, Matter 4 (9), 2765 (2021).
- David G. Cahill, S. K. Watson, and R. O. Pohl, Physical Review B **46** (10), 6131 (1992).
- Ashutosh Giri and Patrick E. Hopkins, Advanced Functional Materials **30** (8), 1903857 (2020).
- Zhiping Xu, Theoretical and Applied Mechanics Letters 6 (3), 113 (2016).
- Eleonora Isotta, Wanyue Peng, Ashiwini Balodhi, and Alexandra Zevalkink, Angewandte Chemie International Edition **62** (12), e202213649 (2023).
- Qing Tu, Ioannis Spanopoulos, Eugenia S. Vasileiadou, Xiaotong Li, Mercouri G. Kanatzidis, Gajendra S. Shekhawat, and Vinayak P. Dravid, ACS Appl. Mater. Interfaces **12** (18), 20440 (2020).
- Hongqiang Gao, Wenjuan Wei, Linsui Li, Yuhui Tan, and Yunzhi Tang, The Journal of Physical Chemistry C **124** (35), 19204 (2020).
- Glen A. Slack and S. Galginaitis, Physical Review 133 (1A), A253 (1964).
- ³⁶⁴ Ching-Hua Su, AIP Advances **5** (5) (2015).
- J. J. Alvarado-Gil, O. Zelaya-Angel, H. Vargas, and J. L. Lucio M, Physical Review B 50 (19), 14627 (1994).
- R. Castro-Rodríguez, M. Zapata-Torres, V. Rejón Moo, P. Bartolo-Pérez, and J. L. Peña, Journal of Physics D: Applied Physics **32** (11), 1194 (1999).
- ³⁶⁷ Gavin Conibeer, Materials Today **10** (11), 42 (2007).
- Sang Hyuk Im, Hi-jung Kim, Sung Woo Kim, Sang-Wook Kim, and Sang Il Seok, Energy & Environmental Science 4 (10), 4181 (2011).
- Ghada I. Koleilat, Larissa Levina, Harnik Shukla, Stefan H. Myrskog, Sean Hinds, Andras G. Pattantyus-Abraham, and Edward H. Sargent, ACS Nano 2 (5), 833 (2008).
- Jin Ho Bang and Prashant V. Kamat, ACS Nano 3 (6), 1467 (2009).
- Junwei Yang and Xinhua Zhong, J. Mater. Chem. A **4** (42), 16553 (2016).
- Kurtis S. Leschkies, Ramachandran Divakar, Joysurya Basu, Emil Enache-Pommer, Janice E. Boercker, C. Barry Carter, Uwe R. Kortshagen, David J. Norris, and Eray S. Aydil, Nano Letters 7 (6), 1793 (2007).
- Fei Huang, Lisha Zhang, Qifeng Zhang, Juan Hou, Hongen Wang, Huanli Wang, Shanglong Peng, Jianshe Liu, and Guozhong Cao, ACS Appl. Mater. Interfaces **8** (50), 34482 (2016).
- Rakesh K. Sonker, Rajkamal Shastri, and Rahul Johari, Energy & Fuels **35** (9), 8430 (2021).
- Muhammad Panachikkool and T. Pandiyarajan, Carbon Letters **34** (1), 445 (2024).

- Miaomiao Li, Wang Ni, Bin Kan, Xiangjian Wan, Long Zhang, Qian Zhang, Guankui Long, Yi Zuo, and Yongsheng Chen, Physical Chemistry Chemical Physics **15** (43), 18973 (2013).
- Mitchell Bacon, Siobhan J. Bradley, and Thomas Nann, Particle & Particle Systems Characterization **31** (4), 415 (2014).
- Andrew Kim, Jatis Kumar Dash, Pawan Kumar, and Rajkumar Patel, ACS Applied Electronic Materials 4 (1), 27 (2022).
- P. Guyot-Sionnest, M. Shim, C. Matranga, and M. Hines, Physical Review B Condensed Matter and Materials Physics **60** (4), R2181 (1999).
- V. Klimov, A. Mikhailovsky, D. McBranch, C. Leatherdale, and M. Bawendi, Physical Review B Condensed Matter and Materials Physics **61** (20), R13349 (2000).
- Dmitri V. Talapin and Jonathan Steckel, MRS Bull. 38 (9), 685 (2013).
- ³⁸² Arden L. Moore and Li Shi, Materials Today **17** (4), 163 (2014).
- Yan Gao, Bo Li, Xiaonan Liu, Huaibin Shen, Yang Song, Jiaojiao Song, Zhijie Yan, Xiaohan Yan, Yihua Chong, Ruyun Yao, Shujie Wang, Lin Song Li, Fengjia Fan, and Zuliang Du, Nature Nanotechnology **18** (10), 1168 (2023).
- Mohamad Insan Nugraha, Indriyati Indriyati, Indah Primadona, Murali Gedda, Gerald Ensang Timuda, Ferry Iskandar, and Thomas D. Anthopoulos, Advanced Materials **35** (38), 2210683 (2023).
- A. Khalid, K. Easawi, S. Abdallah, M. G. El-Shaarawy, S. Negm, and H. Talaat, IOP Conference Series: Materials Science and Engineering **762** (1), 012007 (2020).
- Ali Badawi, N. M. Al-Hosiny, S. Abdallah, Sohair Negm, and M. Hassan Talaat, Journal of Materials Science and Engineering A 2, 1 (2012).
- Najim Al-Hosiny, A Badawi, MAA Moussa, R El-Agmy, and S Abdallah, International Journal of Nanoparticles **5** (3), 258 (2012).
- N. K. Mahanta and A. R. Abramson, presented at the 13th InterSociety Conference on Thermal and Thermomechanical Phenomena in Electronic Systems, 2012 (unpublished).
- Minglu Liu, Yuanyu Ma, and Robert Y. Wang, ACS Nano 9 (12), 12079 (2015).
- Wee-Liat Ong, Sara M. Rupich, Dmitri V. Talapin, Alan J. H. McGaughey, and Jonathan A. Malen, Nat. Mater. **12** (5), 410 (2013).
- Joseph P. Feser, Emory M. Chan, Arun Majumdar, Rachel A. Segalman, and Jeffrey J. Urban, Nano Letters **13** (5), 2122 (2013).
- Benjamin T. Diroll, Peijun Guo, and Richard D. Schaller, Nano Letters **18** (12), 7863 (2018).
- Benjamin T. Diroll and Richard D. Schaller, Nanoscale 11 (17), 8204 (2019).
- Marek Piotrowski, Miguel Franco, Viviana Sousa, José Rodrigues, Francis Leonard Deepak, Yohei Kakefuda, Naoyuki Kawamoto, Tetsuya Baba, Bryan Owens-Baird, Pedro Alpuim, Kirill Kovnir, Takao Mori, and Yury V. Kolen'ko, The Journal of Physical Chemistry C **122** (48), 27127 (2018).
- Kai Gu, Heng Wu, Jiaming Su, Peihan Sun, Ping-Heng Tan, and Haizheng Zhong, Nano Letters **24** (13), 4038 (2024).
- Zhongyong Wang, Alexander D. Christodoulides, Lingyun Dai, Yang Zhou, Rui Dai, Yifei Xu, Qiong Nian, Junlan Wang, Jonathan A. Malen, and Robert Y. Wang, Nano Letters **22** (12), 4669 (2022).

- Yuxing Liang, Benjamin T. Diroll, Kae-Lin Wong, Samantha M. Harvey, Michael Wasielewski, Wee-Liat Ong, Richard D. Schaller, and Jonathan A. Malen, Nano Letters **23** (9), 3687 (2023).
- ³⁹⁸ J. Rupp and R. Birringer, Physical Review B **36** (15), 7888 (1987).
- ³⁹⁹ N. X. Sun and K. Lu, Physical Review B **54** (9), 6058 (1996).
- ⁴⁰⁰ Yadong Yin and A. Paul Alivisatos, Nature **437** (7059), 664 (2005).
- Mehdi B. Zanjani and Jennifer R. Lukes, Journal of Applied Physics 115 (14) (2014).
- Angang Dong, Xingchen Ye, Jun Chen, Yijin Kang, Thomas Gordon, James M. Kikkawa, and Christopher B. Murray, Journal of the American Chemical Society **133** (4), 998 (2011).
- Matthew T. Frederick, Victor A. Amin, Laura C. Cass, and Emily A. Weiss, Nano Letters **11** (12), 5455 (2011).
- Dmitri V. Talapin, Jong-Soo Lee, Maksym V. Kovalenko, and Elena V. Shevchenko, Chemical Reviews **110** (1), 389 (2010).
- Nuri Yazdani, Maximilian Jansen, Deniz Bozyigit, Weyde M. M. Lin, Sebastian Volk, Olesya Yarema, Maksym Yarema, Fanni Juranyi, Sebastian D. Huber, and Vanessa Wood, Nature Communications **10** (1), 4236 (2019).
- Roger H. Terrill, Timothy A. Postlethwaite, Chun-hsien Chen, Chi-Duen Poon, Andreas Terzis, Aidi Chen, James E. Hutchison, Michael R. Clark, and George Wignall, Journal of the American Chemical Society **117** (50), 12537 (1995).
- Michael A. Boles and Dmitri V. Talapin, Journal of the American Chemical Society **136** (16), 5868 (2014).
- Mark C. Weidman, Kevin G. Yager, and William A. Tisdale, Chemistry of Materials **27** (2), 474 (2015).
- Kyle J. Schnitzenbaumer and Gordana Dukovic, Nano Letters **18** (6), 3667 (2018).
- Xin Yan, Xiao Cui, Binsong Li, and Liang-shi Li, Nano Letters 10 (5), 1869 (2010).
- Iuliana Mihalache, Antonio Radoi, Mihai Mihaila, Cornel Munteanu, Alexandru Marin, Mihai Danila, Mihaela Kusko, and Cristian Kusko, Electrochimica Acta 153, 306 (2015).
- Golnoush Zamiri and Samira Bagheri, Journal of Colloid and Interface Science **511**, 318 (2018).
- Vinay Gupta, Neeraj Chaudhary, Ritu Srivastava, Gauri Datt Sharma, Ramil Bhardwaj, and Suresh Chand, Journal of the American Chemical Society **133** (26), 9960 (2011).
- Haoxue Han, Yong Zhang, Nan Wang, Majid Kabiri Samani, Yuxiang Ni, Zainelabideen Y. Mijbil, Michael Edwards, Shiyun Xiong, Kimmo Sääskilahti, Murali Murugesan, Yifeng Fu, Lilei Ye, Hatef Sadeghi, Steven Bailey, Yuriy A. Kosevich, Colin J. Lambert, Johan Liu, and Sebastian Volz, Nature Communications 7 (1), 11281 (2016).
- A. J. Nozik, Physica E: Low-dimensional Systems and Nanostructures **14** (1), 115 (2002).
- M. Potenza, A. Cataldo, G. Bovesecchi, S. Corasaniti, P. Coppa, and S. Bellucci, AIP Advances 7 (7) (2017).
- A. H. Elsheikh, S. W. Sharshir, Mohamed E. Mostafa, F. A. Essa, and Mohamed Kamal Ahmed Ali, Renewable and Sustainable Energy Reviews **82**, 3483 (2018).
- Elaheh K. Goharshadi, Zohreh Niyazi, Masoomeh Shafaee, Monireh B. Moghaddam, Ralf Ludwig, and Majid Namayandeh-Jorabchi, Journal of Molecular Liquids **241**, 831 (2017).

- Ehsanollah Ettefaghi, Barat Ghobadian, Alimorad Rashidi, G. Najafi, Mohammad Hadi Khoshtaghaza, and Sepideh Pourhashem, Energy Conversion and Management **153**, 215 (2017).
- F. Sedaghat and F. Yousefi, Journal of Molecular Liquids **278**, 299 (2019).
- Joel R. Seibert, Ozgur Keles, Jun Wang, and Folarin Erogbogbo, Data in Brief **28**, 105008 (2020).
- Khan M. F. Shahil and Alexander A. Balandin, Nano Letters 12 (2), 861 (2012).
- E. Isotta, U. Syafiq, N. Ataollahi, A. Chiappini, C. Malerba, S. Luong, V. Trifiletti, O. Fenwick, N. M. Pugno, and P. Scardi, Physical Chemistry Chemical Physics **23** (23), 13148 (2021).
- Haoran Yang, Luis A. Jauregui, Genqiang Zhang, Yong P. Chen, and Yue Wu, Nano Letters **12** (2), 540 (2012).
- Min-Ling Liu, Fu-Qiang Huang, Li-Dong Chen, and I-Wei Chen, Appl. Phys. Lett. **94** (20) (2009).
- Jonathan M. Skelton, Adam J. Jackson, Mirjana Dimitrievska, Suzanne K. Wallace, and Aron Walsh, APL Materials **3** (4) (2015).
- Martin Handwerg, Rüdiger Mitdank, Sergiu Levcenco, Susan Schorr, and Saskia F Fischer, Materials Research Express 7 (10), 105908 (2020).
- Eleonora Isotta, Binayak Mukherjee, Carlo Fanciulli, Narges Ataollahi, Ilya Sergueev, Svetoslav Stankov, Raju Edla, Nicola M. Pugno, and Paolo Scardi, Physical Review Applied **14** (6), 064073 (2020).
- W. D. Thompson, Abhishek Nandur, and B. E. White, Jr., Journal of Applied Physics **119** (9) (2016).
- Kevin Ye, Sin Cheng Siah, Peter T. Erslev, Austin Akey, Charles Settens, Md Shafkat Bin Hoque, Jeffrey Braun, Patrick Hopkins, Glenn Teeter, Tonio Buonassisi, and R. Jaramillo, Chemistry of Materials **31** (20), 8402 (2019).
- Sarita Devi Sharma, B. Khasimsaheb, Y. Y. Chen, and S. Neeleshwar, Ceram. Int. **45** (2, Part A), 2060 (2019).
- Katarzyna Kapusta, Mariusz Drygas, Jerzy F. Janik, Piotr Jelen, Miroslaw M. Bucko, and Zbigniew Olejniczak, Journal of Alloys and Compounds **770**, 981 (2019).
- Qihao Zhang, Xin Ai, Lianjun Wang, Yanxia Chang, Wei Luo, Wan Jiang, and Lidong Chen, Advanced Functional Materials **25** (6), 966 (2015).
- Kyu-Hyoung Lee, Hyun-Sik Kim, Sang-Il Kim, Eun-Sung Lee, Sang-Mock Lee, Jong-Soo Rhyee, Jae-Yong Jung, Il-Ho Kim, Yifeng Wang, and Kunihito Koumoto, Journal of Electronic Materials **41** (6), 1165 (2012).
- Biplab Paul, Ajay Kumar V, and P. Banerji, Journal of Applied Physics 108 (6) (2010).
- Machhindra Koirala, Huaizhou Zhao, Mani Pokharel, Shuo Chen, Tulashi Dahal, Cyril Opeil, Gang Chen, and Zhifeng Ren, Applied Physics Letters **102** (21) (2013).
- Shanyu Wang, Han Li, Ruiming Lu, Gang Zheng, and Xinfeng Tang, Nanotechnology **24** (28), 285702 (2013).
- L. Dong, L. Ye, D. Zhao, L. Tong, F. Gao, W. Li, P. Lu, and X. H. Bu, J Phys Chem Lett **11** (14), 5728 (2020).
- Zhurong Liang, Shaohong Zhang, Xueqing Xu, Nan Wang, Junxia Wang, Xin Wang, Zhuoneng Bi, Gang Xu, Ningyi Yuan, and Jianning Ding, RSC Adv. **5** (74), 60562 (2015).

- Namchul Cho, Feng Li, Bekir Turedi, Lutfan Sinatra, Smritakshi P. Sarmah, Manas R. Parida, Makhsud I. Saidaminov, Banavoth Murali, Victor M. Burlakov, Alain Goriely, Omar F. Mohammed, Tom Wu, and Osman M. Bakr, Nature Communications 7 (1), 13407 (2016).
- Linfang Yan, Junjie Ma, Pengwei Li, Shuangquan Zang, Liyuan Han, Yiqiang Zhang, and Yanlin Song, Advanced Materials **34** (7), 2106822 (2022).
- Zhenghong Dai, Srinivas K. Yadavalli, Min Chen, Ali Abbaspourtamijani, Yue Qi, and Nitin P. Padture, Science **372** (6542), 618 (2021).
- Zhenghong Dai and Nitin P. Padture, Nature Energy 8 (12), 1319 (2023).
- In Seok Yang, Zhenghong Dai, Anush Ranka, Du Chen, Kai Zhu, Joseph J. Berry, Peijun Guo, and Nitin P. Padture, Advanced Materials **36** (3), 2308819 (2024).
- F. Hofmann, D. R. Mason, J. K. Eliason, A. A. Maznev, K. A. Nelson, and S. L. Dudarev, Scientific Reports 5 (1), 16042 (2015).
- Moojoong Kim, Kuentae Park, Gwantaek Kim, Jaisuk Yoo, Dong-Kwon Kim, and Hyunjung Kim, Applied Sciences **9** (8), 1522 (2019).
- Diganta Sarkar, Riley Hooper, Abhoy Karmakar, Victor Terskikh, and Vladimir Michaelis, (2021).
- Xavier Mettan, Riccardo Pisoni, Péter Matus, Andrea Pisoni, Jaćim Jaćimović, Bálint Náfrádi, Massimo Spina, Davor Pavuna, László Forró, and Endre Horváth, The Journal of Physical Chemistry C 119 (21), 11506 (2015).